A Review of Degradation Mechanisms and Recent Achievements for Ni-Rich Cathode-Based Li-Ion Batteries

Ming Jiang, Dmitri L. Danilov, Rüdiger-A. Eichel, and Peter H. L. Notten*

The growing demand for sustainable energy storage devices requires rechargeable lithium-ion batteries (LIBs) with higher specific capacity and stricter safety standards. Ni-rich layered transition metal oxides outperform other cathode materials and have attracted much attention in both academia and industry. Lithium-ion batteries composed of Ni-rich layered cathodes and graphite anodes (or Li-metal anodes) are suitable to meet the energy requirements of the next generation of rechargeable batteries. However, the instability of Ni-rich cathodes poses serious challenges to large-scale commercialization. This paper reviews various degradation processes occurring at the cathode, anode, and electrolyte in Ni-rich cathode-based LIBs. It highlights the recent achievements in developing new stabilization strategies for the various battery components in future Ni-rich cathode-based LIBs.

1. Introduction

Motivated by the necessity of reducing CO_2 emission and urgent transition from fossil fuels to sustainable clean energy sources, rechargeable lithium-ion batteries (LIBs) have received much academic and industrial attention since their commercialization by Sony in 1991. Stimulated by the constant technological innovations, government subsidies, and the thriving markets of, for

M. Jiang, D. L. Danilov, P. H. L. Notten
Department of Electrical Engineering
Eindhoven University of Technology
P.O. Box 513, Eindhoven, MB 5600, The Netherlands
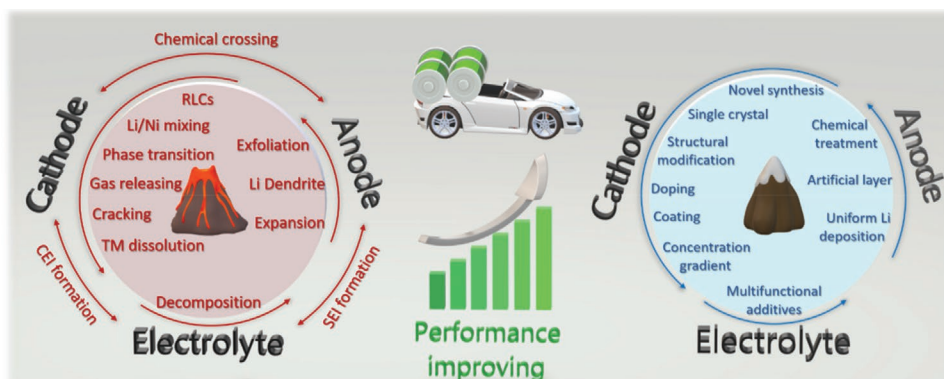E-mail: p.h.l.notten@tue.nl
M. Jiang, D. L. Danilov, R.-A. Eichel, P. H. L. Notten
Institute of Energy and Climate Research
Forschungszentrum Jülich (IEK-9)
D-52425 Jülich, Germany
R.-A. Eichel
Institute of Physical Chemistry
RWTH Aachen University
D-52074 Aachen, Germany
P. H. L. Notten
Centre for Clean Energy Technology
University of Technology Sydney
Broadway, Sydney, NSW 2007, Australia

example, consumer electronics and electric vehicles (EVs), LIBs have made considerable progress. Ni-based layered transition metal (TM) oxides have managed to amass a dominant position in chosen cathode materials during the last decade.[1–3] In 2012, all early EV models used batteries based on $LiNi_{1/3}Co_{1/3}Mn_{1/3}O_2$ (NCM111) cathode materials. However, NCM111-based LIBs cannot fulfill the growing demand for higher specific energy, envisioned to approach 350 Wh kg^{-1} at a cell level by 2025.[4] To increase the energy density, layered transition metal oxides with higher Ni-content have been developed, denoted as Ni-rich cathodes. Two major advantages of Ni-rich cathodes are their high specific energy capacity (200–250 mAh g^{-1}) and the relatively high operating voltage (≈4.3 V vs Li$^+$/Li), which are more promising in many applications compared to the other cathode materials, such as $LiCoO_2$, $LiFePO_4$, Li_2MnO_4, etc.[5]

The superiority of Ni-rich cathodes in storage capacity also brings the tradeoff with electrochemical stability. It was confirmed that the crystal structure of the Ni-rich cathode materials is prone to irreversibly transform during the (de)lithiation process, resulting in rapid performance fading.[6] The degree of degradation depends on the particular elemental composition in the cathode material. However, all Ni-rich cathodes undergo similar electronic and structural changes. Apart from cathode materials, the degradations occurring in the battery anode and electrolyte should also be considered from a full-cell perspective.[7] Graphite is the commercially most successful anode material in the market. It is commonly employed together with Ni-rich cathode in modern batteries.[8] Li-metal is considered an ideal anode material because of its lowest negative electrochemical electrode potential. Coupled with a Ni-rich cathode, it will significantly boost the battery capacity.[9] However, both anode materials suffer from serious problems, such as solid-electrolyte-interphase (SEI) formation, dendrite growth, etc. Such detrimental issues severely hinder the large-scale commercialization of the Ni-rich-based LIBs as next-generation batteries.[10]

This review starts with a general introduction to the fundamental properties of Ni-rich cathode materials, chemically and electrochemically. Then, a comprehensive discussion of the underlying degradation mechanisms of Ni-rich cathodes, anodes, and electrolytes will be addressed. The state-of-the-art mitigation solutions proposed over the past five years will also be summarized (**Figure 1**). Finally, a perspective on future directions of designing Ni-rich cathode-based LIBs with superior performance will be presented.

Figure 1. Current challenges arising in Ni-rich cathode-based LIBs and emerging solutions.

2. Properties of Ni-Rich Cathode Materials

Ni-rich cathode materials are derived from layered $LiNiO_2$, first discovered by Dyer et al. in the 1950s.[11] $LiNiO_2$ was one of the candidates as electrode material with a strong commercialization perspective. However, the structural degradation of $LiNiO_2$ is extreme, hindering its further development. Other elements, such as Co, Mn, Al, Zr, etc., were introduced into the $LiNiO_2$ and partially substituted Ni to overcome this deficiency. Among all the elements, Co, Mn, and Al substitutions are most relevant for improving Ni-rich cathode materials' performance.[12] Co contributes to the rate capacity enhancement and cation-mixing mitigation, while substitution by Mn is beneficial to the structural stability of $LiNiO_2$.

Furthermore, partial substitution of Ni by Al ions is also advantageous and cost-effective due to the low cost and light atomic weight of Al. Consequently, the excellent synergy between Ni, Co, Mn, and Ni, Co, Al ensures Ni-rich NCM ($LiNi_xCo_yMn_{1-x-y}O_2$, $x \geq 0.6$) and NCA ($LiNi_xCo_yAl_{1-x-y}O_2$, $x \geq 0.6$) materials are the most promising materials to improve LIBs further.[4] Up to now, Ni-rich cathodes of various compositions have been proposed and comprehensively investigated, leading to a better understanding of the degradation mechanism and improvement in performance.[13]

2.1. Chemical Properties

The crystallographic structure of layered $LiMO_2$ (M = transition metals, Ni, Co, Mn, Al, etc.) is isostructural with α-$NaFeO_2$, where the rhombohedral crystal with O3-type layered oxide structure, formed by a cubic close-packed (ccp) lattice, is surrounded by oxygen atoms (**Figure 2**a).[14] Considering that the octahedral
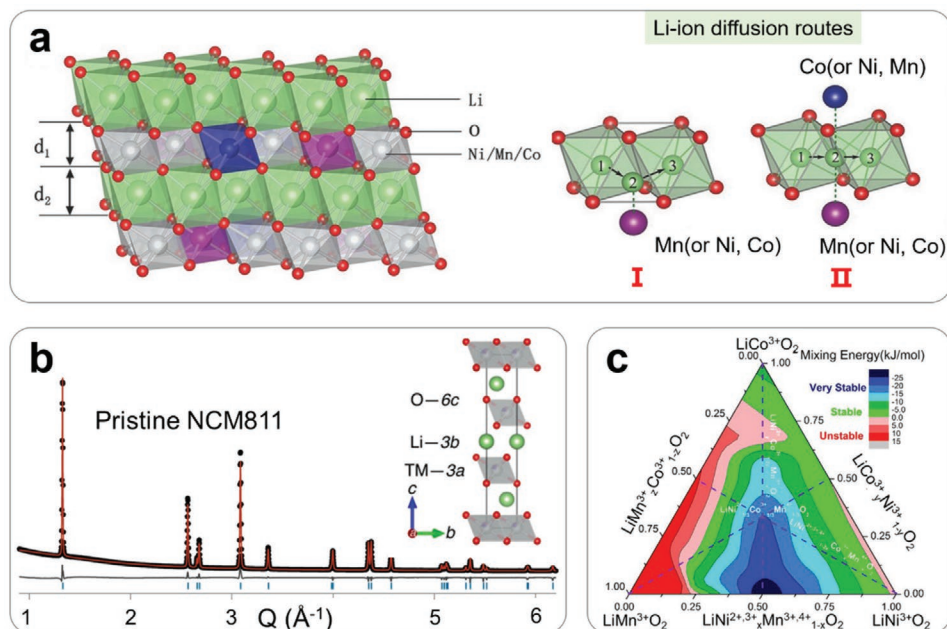
Figure 2. a) Lattice of the NMC layered structure, tetrahedral site pathway (route I), and oxygen dumbbell pathway (route II) for Li-ion diffusion. b) XRD pattern of pristine polycrystalline NMC811. c) Mixing energy predicted from the present bonding model for the solid solution $LiMO_2$ (M = Ni, Co, Mn) phase triangle. a) Reproduced with permission.[14] Copyright 2016, Wiley-VCH. b) Reproduced with permission.[15] Copyright 2021, Nature. c) Reproduced with permission.[17] Copyright 2016, American Chemical Society.

**ADVANCED
SCIENCE NEWS**

www.advancedsciencenews.com

**ADVANCED
ENERGY
MATERIALS**

www.advenergymat.de

sites in $LiMO_2$ crystal are occupied by lithium or TMs, the layer structure in $LiMO_2$ can be divided into Li slabs and transition metal oxide slabs. The thickness of the Li and transition metal oxide slabs are represented by d_1 and d_2, respectively. Such slabs alternate each other in the crystal. The relationship between d_1 and d_2 is usually represented by $d_{001} = d_1 + d_2$.

It is well known that the layered structure has 2D channels for Li-ion diffusion. Apart from that, two kinds of Li-ion diffusion routes have been proposed by Pan and co-workers.[14] Li+ ions will either move from one octahedral site to the next site through the intermediate tetrahedral sites (route I) or hop via the oxygen dumbbells (route II). At the early stage of delithiation, the oxygen dumbbell diffusion is most dominant. When about 1/3 of lithium is extracted, the tetrahedral site pathway becomes prevailing. Typical X-ray diffraction (XRD) patterns corresponding to reflections of (104) and (003) planes are illustrated in Figure 2b.[15] Some Li–TM cations disorder can easily occur in layered $LiMO_2$, especially at high state-of-charge (SOC) or high temperatures, weakening the electrochemical performance.[16] The relationship between the intensity of the (104) and (003) reflections plays an essential role in cation disorder studies. It will be discussed in detail in the following sections.

With various cation dopant ratios in $LiMO_2$, the TM–TM bonds show different bond strengths, closely related to the phase stability of $LiMO_2$. Cho and co-workers quantitatively investigated the relative stability of NCM materials with a variation of the Ni, Co, Mn composition (Figure 2c).[17] Based on the bond model given in this work, the strong bonds of $Mn^{4+}-Mn^{4+}$ (-22.09 kJ mol^{-1}) and $Ni^{2+}-Mn^{4+}$ (-15.28 kJ mol^{-1}) lead to the most stable materials composition in the phase diagram: $LiNi_{0.5}Mn_{0.5}O_2$. With increasing Co content in $LiNi_yCo_{1-2y}Mn_yO_2$, the mixing energy remains relatively low until the $LiNi_{1/3}Co_{1/3}Mn_{1/3}O_2$ (NCM111) composition has been reached. From NCM111 to $LiNiO_2$, the ternary composition is showing reduced phase stability. In contrast, a higher content of Mn ion leads to higher mixing energies and compromised material stability, which can be seen in Figure 2c near the $LiMnO_2$ vertex, where the number of weak Mn^{3+}–TM bonds is large.

2.2. Electrochemical Properties

The Ni-content in NCM materials mainly determines the electrochemical properties and structural stability. Nowadays, many studies confirmed a concomitant increase in storage capacity and decreased electrode stability with increasing Ni-content.[18,19] Particularly, an increasing Ni ratio results in a simultaneous increase in high-valence Ni ions (Ni^{3+}, Ni^{4+}), which contributes to the higher capacity. However, these ions tend to easily react with the battery electrolyte, resulting in detrimental cycling instabilities.

Major and co-workers studied NCM materials with different Ni-content by employing the density functional theory (DFT) method and elaborated on the crucial effect of the Ni-content.[20] The amounts of high-valence Ni ions (Ni^{4+}) in NCMs are presented in **Figure 3**a. It can be seen that the amount of Ni^{4+} increases from low-Ni NCMs (NCM424: $LiNi_{0.4}Co_{0.2}Mn_{0.4}O_2$, NCM523: $LiNi_{0.5}Co_{0.2}Mn_{0.3}O_2$) to Ni-rich NCMs (NCM622: $LiNi_{0.6}Co_{0.2}Mn_{0.2}O_2$, NCM811: $LiNi_{0.8}Co_{0.1}Mn_{0.1}O_2$). The Ni ions in NCM consist of Ni^{2+}, Ni^{3+}, and Ni^{4+}, the increase of Ni-content

in NCMs brings a higher amount of Ni^{4+} in the supercell. Note that the concentration of Ni^{4+} decreases rapidly with the increase of SOC. That means Ni^{4+} can easily react with oxygen or electrolyte species during charging due to the low-lying lowest unoccupied molecular orbital (LUMO), resulting in fast degradation.

Recent studies have further confirmed that NCMs with higher Ni fractions reveal lower capacity retention upon cycling. The experimental result of NCMs with various Ni-content is given by Sun and co-workers, as shown in Figure 3b.[18] Ni-rich cathodes suffer from severe capacity decay. When the composition reaches $LiNiO_2$, the capacity retention drops to ≈75% after 100 cycles, making it unsuitable for practical applications. Apart from the Ni-content in the compounds, the higher Li utilization (higher SOC) is also a leading cause of accelerating mechanical fracture. Manthiram and co-workers similarly detected the abrupt lattice collapse of NCMs with various Ni-content (90, 70, 50, and 33 mol%). When Li-utilization reaches 80% at high cut-off given voltage, structural deterioration consistently occurs in various NCMs.[21]

Figure 3 further summarizes the fundamental electrochemical characteristics of Ni-rich NCM-based electrodes.[18] The charge–discharge voltage curves (Figure 3c) indicate that for Ni-rich NCMs ($x > 90\%$), the specific capacity is improved despite its reduced stability shown in Figure 3b. The authors experimentally confirmed that the discharge capacity of Ni-rich NCMs displays a linear relationship with the Ni-content in the compounds. At the same time, the theoretical capacity of NCM of 275 mAh g^{-1} indicates considerable potential for further growth. An increasing Ni content is therefore essential for further developments. That becomes one of the most crucial research directions. Furthermore, a higher Ni-content also leads to an enhanced rate capability, as shown in Figure 3d, where the rate capabilities of NCM622 and $LiNi_{0.90}Co_{0.05}Mn_{0.05}O_2$ (NCM900505) are compared.[22]

A comprehensive understanding of NCM phase transformations during the charge and discharge processes is critical for mechanistic studies. Prior to the work of Dahn and co-workers in 1993, the structural evolution of layered $LiNiO_2$ as a function of voltage was only investigated in two-phase regions.[16] Using in situ XRD measurements, they, for the first time, proposed four-phase regions for the operation of $LiNiO_2$ electrodes. Such a phase diagram has been widely accepted in other NCM studies since then. The four phase regions have been described as follows. During the delithiation process $Li_{1-x}NiO_2$ (x changes from 0.0 to 0.82) undergoes various phase transitions, starting from hexagonal-1 (denoted as H1) to monoclinic (denoted as M), then from M to hexagonal-2 (denoted as H2), and finally from H2 to hexagonal-3 (H3). **Table 1** summarizes the evolution of phase region in $LiNi_{1-x}O_2$ with the increase of voltage. The definitions of three hexagonal phases are determined by the evolution of lattice parameters in $Li_{1-x}NiO_2$. They can be traced in the differential capacity (dQ/dV) curves.[23] Such plots provide a suitable way to identify the phase transformations of corresponding layered Ni-rich materials electrochemically. Based on the analysis of $LiNiO_2$, the phase evolution of NCMs with various Ni-content is illustrated in Figure 3e.[18] In the case of the NCMs with a Ni ratio higher than 80% ($LiNi_{0.95}Co_{0.025}Mn_{0.025}O_2$, $LiNi_{0.9}Co_{0.05}Mn_{0.05}O_2$, and $LiNi_{0.8}Co_{0.1}Mn_{0.1}O_2$), the phase transformations are similar to those in $LiNiO_2$, showing the original H1 phase transformed into M, H2, and H3 phases. Three
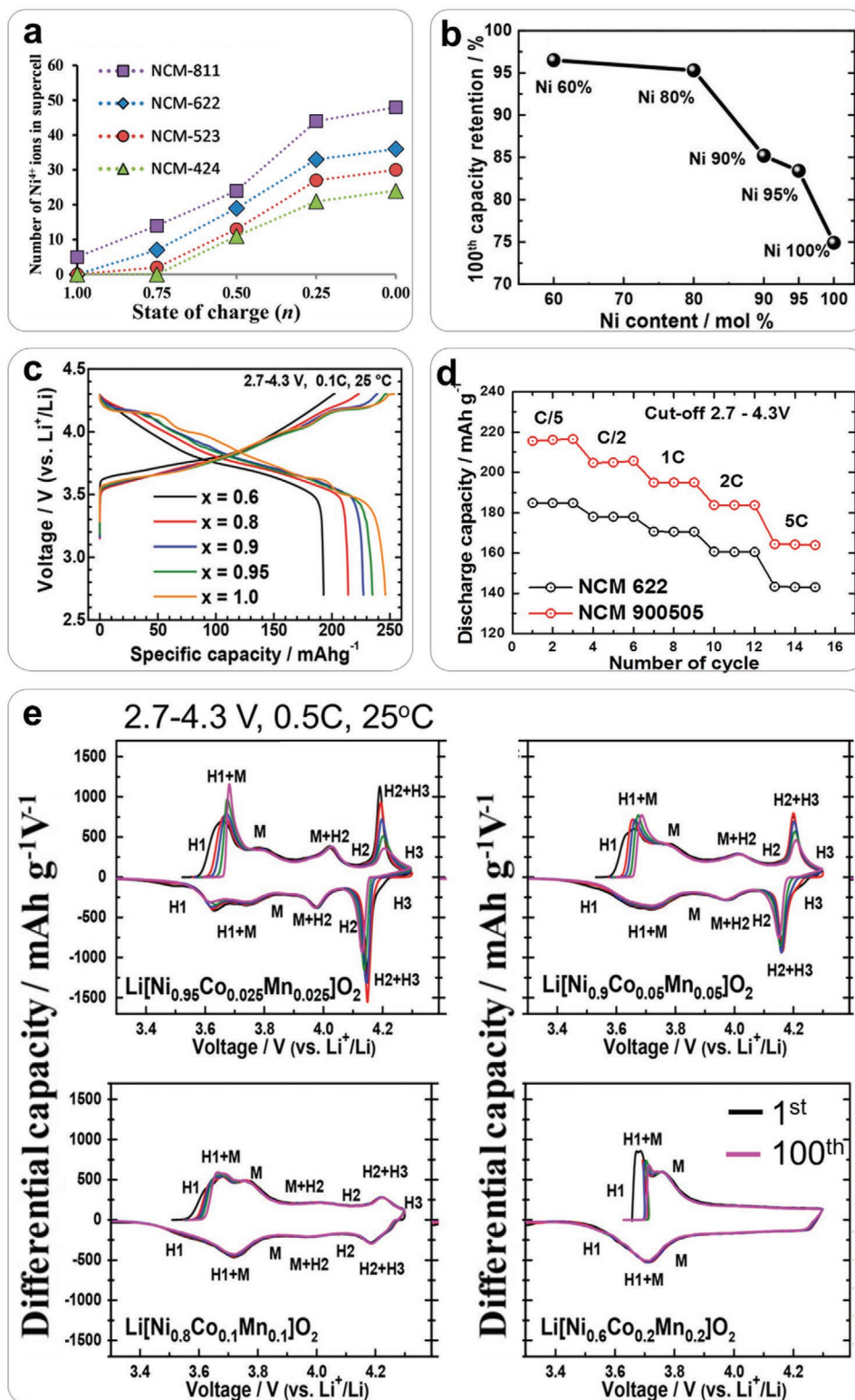
Figure 3. a) The amount of Ni^{4+} ions as a function of SOC in the supercell of various NCMs via the calculation of DFT. b) Capacity retention at 0.5C after 100 cycles plotted as a function of the Ni content. c) Initial charge and discharge voltage curves for $LiNi_xCoMn_{1-x-y}O_2$ ($x = 0.6, 0.8, 0.9, 0.95$, and 1), and comparison of the 0.5C discharge capacities as a function of Ni content (x). d) Rate capabilities of NCM622 and NCM900505 cathodes at various C rates in the voltage range of 2.7–4.3 V. e) Differential capacity profiles (dQ/dV) of various NCM materials. a) Reproduced with permission.[20] Copyright 2017, American Chemical Society. b,c) Reproduced with permission.[18] Copyright 2018, American Chemical Society. d) Reproduced with permission.[22] Copyright 2017, American Chemical Society. e) Reproduced with permission.[18] Copyright 2018, American Chemical Society.

**ADVANCED
SCIENCE NEWS**

www.advancedsciencenews.com

**ADVANCED
ENERGY
MATERIALS**

www.advenergymat.de

Table 1. Summary of phase regions of LiNi$_{1-x}$O$_2$ in the indicated voltage range.[16]

Phase region	H1	H1+M	M	M+H2	H2	H2+H3	H3
x in LiNi$_{1-x}$O$_2$	<0.15	0.15–0.25	0.25–0.50	0.50–0.57	0.57–0.68	0.68–0.82	>0.82
Voltage range [V]	<3.7	3.7	3.7–4.0	4.0	4.0–4.2	4.2	>4.2

phase-coexistence regions are located at around 3.7 (H1+M), 4.0 (M+H2), and 4.2 V (H2+H3). The transition from H2 to H3 under a high voltage regime is mainly attributed to the abrupt shrinkage on the *c*-axis in the unit cell, resulting in detrimental anisotropic lattice volume changes. In the case of NCM622, the peak of the H2-to-H3 transformation is absent in the phase diagram. Apparently, the existence of the H2–H3 peak is becoming distinct with the increasing of Ni-content, suggesting that the H2–H3 transformation plays a significant role in the structural stability. Thus, it is of importance to thoroughly investigate the lattice collapse at high SOC in Ni-rich NCMs.

Figure 4a shows a typical plot differential capacity plot as a function of electrode voltage.[24] Depending on the cut-off voltage, the full profile can be split into stable (green) and unstable (red) regions. When the voltage is above 4.11 V, the electrode undergoes the H2–H3 transition, accompanied by lattice oxygen reduction. This transition induces the lattice collapse and is considered harmful for maintaining the reversible storage capacity. Based on theoretical and experimental studies, the lattice collapse of Ni-rich NCMs is linked with *c*-axis lattice shrinkage during the H2-to-H3 phase transition. The *c*-axis parameter is related to the distance between the Li layers in the
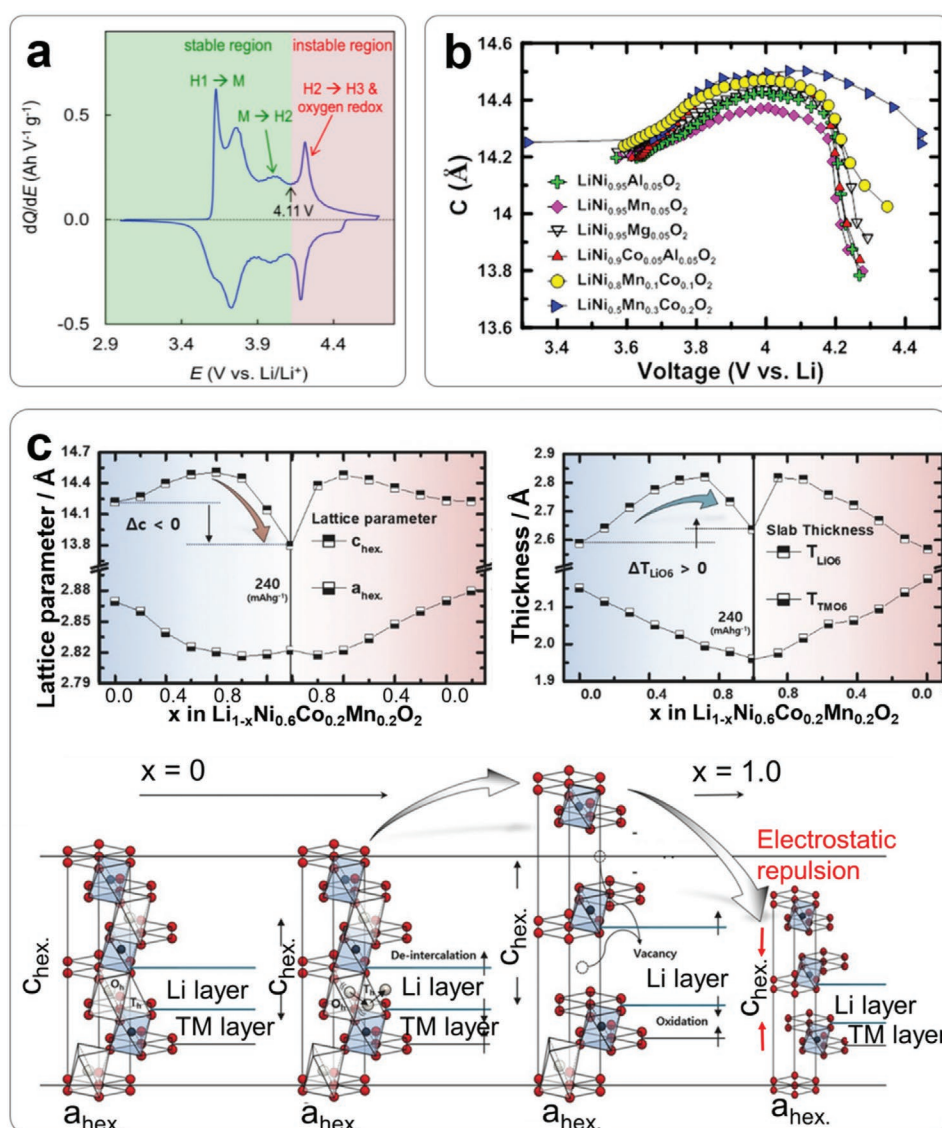
Figure 4. a) Typical dQ/dV curves for Ni-rich NCM/Li cells. b) *c*-axis lattice parameter as a function of *x* in Li$_x$MO$_2$. c) Lattice parameter evolution of Li$_{1-x}$Ni$_{0.6}$Co$_{0.2}$Mn$_{0.2}$O$_2$ during charge and discharge, and the structural evolution of the NCM622 cathode material during the first deintercalation process from *x* = 0 to *x* = 1.0. a) Reproduced with permission.[24] Copyright 2020, Elsevier. b) Reproduced with permission.[25] Copyright 2019, American Chemical Society. c) Reproduced with permission.[26] Copyright 2018, Wiley-VCH.

**ADVANCED
SCIENCE NEWS**
www.advancedsciencenews.com

**ADVANCED
ENERGY
MATERIALS**
www.advenergymat.de

electrode material. It shows a similar evolutionary trend with the unit cell volume, regardless of the various compositions and Ni-content (from 50% to 95%). The evolution of the *c*-axis lattice parameter as the function of voltage and Li content during delithiation has been collected and calculated by in situ XRD experiments, as shown in Figure 4b.[25] Apparently, the length of the *c*-axis lattice experiences a sudden decrease when the voltage reaches 4.1 V when the cathode is at higher SOC. Comparable results have been obtained and verified by many other studies. That indicates the highly unstable H2-to-H3 phase transition in Ni-rich layered materials is strongly related to the anisotropic lattice parameters change during deep delithiation.

Although the above conclusion has been widely accepted nowadays, Yoon and co-workers brought a new understanding regarding the lattice parameters evolution of $LiNi_{0.5+x}Co_{0.2}Mn_{0.3-x}O_2$ (x = 0, 0.1, 0.2) materials during (dis) charging.[26] In previous studies, the Co and Mn content in Ni-rich NCMs are changed independently.[27] Since the role of Mn does not associate with the charge composition mechanism, the authors fixed the Co content in various Ni-rich NCMs for a more detailed investigation of the effect of Ni. For the layered material, the *c*-axis parameter can be calculated by combining the thickness of the TMO_6 slab and the LiO_6 interslab, as illustrated in Figure 4c. Based on high-resolution powder diffraction (HRPD) experiments, it is found that movement of Li^+ ions has a close relationship with the thickness of the LiO_6 interslab, while it seems not related to the thickness of the TMO_6 slab. The sharp decrease of the *c*-axis parameter at high SOC is mainly attributed to the decreasing TMO_6 slab thickness rather than LiO_6. The thickness of the LiO_6-interslab in the fully delithiated state even shows a slight increase compared with the original state due to electrostatic repulsion. In addition, shrinkage of the *c*-axis parameter with increasing Ni-content is also due to the shrinkage of the TMO_6 slab thickness. In contrast, the distance of LiO_6-interslab remains almost the same. This work offers a unique insight into the lattice change of Ni-rich cathodes during the electrochemical process and sheds more light on the charge evolution mechanism. Since the development of Ni-rich cathodes aims to a much higher Ni-content, a profound understanding of the phase transition behavior is essential for the degradation examination and the redemption of strategies exploration.

3. Degradation Mechanisms

Despite the growing expectations toward Ni-rich cathode-based LIBs, their practical application is still restricted due to the rapid performance degradation and safety hazard issues. Generally, for a Ni-rich cathode-based LIB, the degradation problem can originate from different parts in the battery system: cathode, electrolyte, and anode. The current problems and challenges that Ni-rich cathodes are still facing can be summarized as follows: 1) Residual lithium compounds (RLCs) that are inevitably formed during the material preparation process; 2) cation disorder (or Li/TM lattice mixing) triggered by the material synthesis and battery cycling; 3) structural reconstruction occurring at the electrode surface during electrochemical operation, induced by the layered-spinel-rock-salt phase transition combined with the formation of lattice oxygen vacancies; 4) O_2 and CO_2 gas release
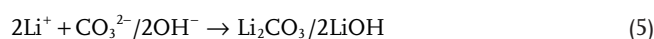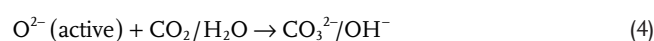
at the electrode material surface, which is closely related to surface reconstruction and side-reactions with the electrolyte; 5) transition metal dissolution as the consequence of HF attack; 6) intragranular and intergranular cracks formed at high SOC and intensive cycling; and 7) The fragile thermal stability, which may lead to thermal runaway, leading to serious safety concerns.
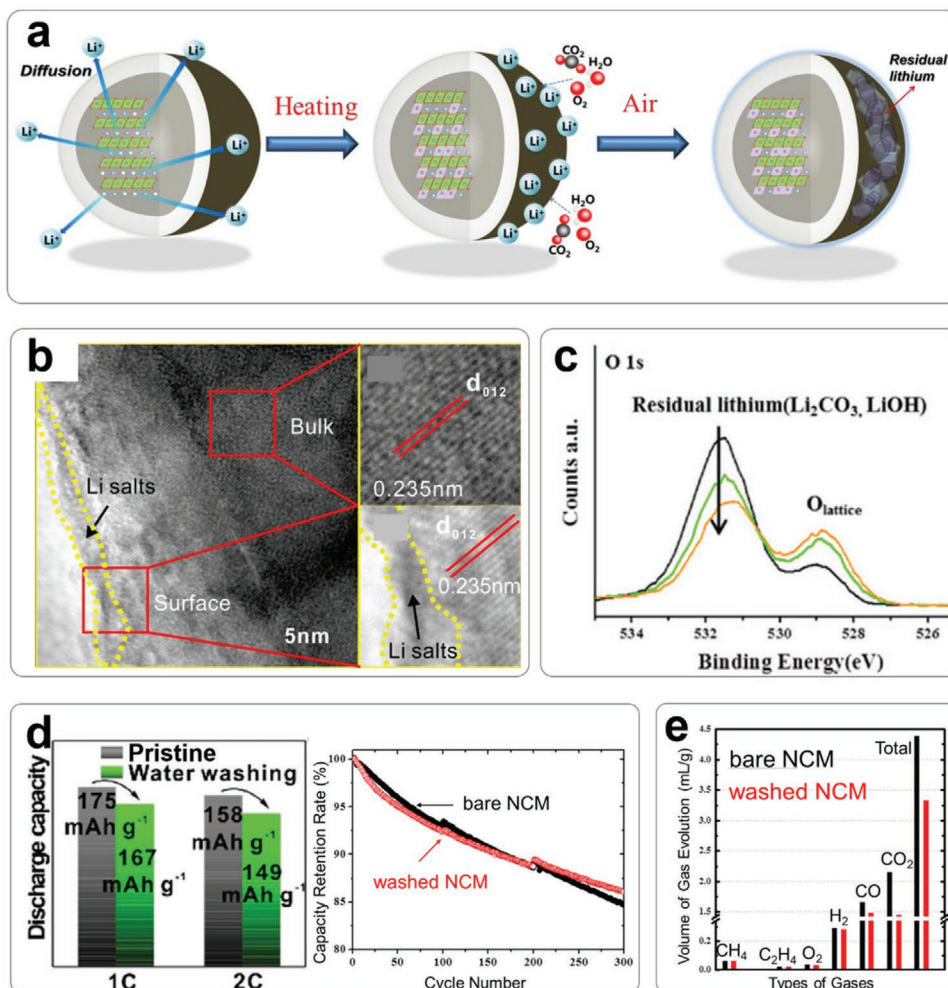
Apart from the various degradation mechanisms at the cathode side, detrimental reactions in the anode and the electrolyte could also cause further battery performance decay. On the one hand, the graphite anode suffers from severe volume expansion and graphite layer collapse. In contrast, the Li-metal anode suffers from dendrite growth and the formation of "death lithium" spots. On the other hand, electrolyte decomposition will spontaneously engage in the solid-electrolyte-interphase formation at both the cathode and anode, forming passivating layers at both electrodes. All the above challenges are generally interlinked in the battery operation. Therefore, a comprehensive and in-depth study of these problems is essential for developing LIBs with a prolonged life span and improved stability. The degradation mechanisms associated with Ni-rich cathodes, anodes, and electrolytes will be presented in subsequent sections.

3.1. Cathode

3.1.1. Residual Lithium Compounds

RLCs are inevitably formed in Ni-rich cathodes and mainly consist of $LiOH$, Li_2CO_3, Li_2O, Li_2O_2, and $LiHCO_3$.[28] Most of these compounds will eventually convert into $LiOH$ and Li_2CO_3 during storage. The formation of RLCs stems from two processes. During the synthesis process, an excess amount of lithium salts (typically 5 mol% higher) is added as transition metal precursor(s) to compensate for the lithium loss during calcination because of the volatilization of lithium at high temperatures. On the one hand, a higher amount of lithium salt can inhibit Li/TM mixing. On the other hand, the excessive lithium content will remain at the particle surface and simultaneously react with H_2O, O_2, and CO_2 in the air.[29] With an increasing Ni-content in Ni-rich cathodes, a lower calcination temperature and higher oxygen purity will be needed during preparation. That will likely lead to the formation of undesirable RLCs layers.[30] The highly active Ni^{3+} ions in the cathode material can contribute to the RLCs formation as well. The spontaneous reduction of Ni^{3+} to Ni^{2+} at the surface will give rise to lattice oxygen O^{2-} oxidation and the consequent reaction with Li^+. It can be described by the following equations[31]

$$Ni^{3+} + O^{2-} (lattice) \rightarrow Ni^{2+} + O^- \tag{1}$$

$$O^- + O^- \rightarrow O^{2-} (active) + O \tag{2}$$

$$O^- + O \rightarrow O_2^-; O + O \rightarrow O_2 \tag{3}$$

$$O^{2-} (active) + CO_2/H_2O \rightarrow CO_3^{2-}/OH^- \tag{4}$$

$$2Li^+ + CO_3^{2-}/2OH^- \rightarrow Li_2CO_3/2LiOH \tag{5}$$

Figure 5. a) Schematic representation of the formation process of LiOH and Li_2CO_3 at an $LiNi_{0.7}Mn_{0.3}O_2$ cathode surface. b) TEM images of a pristine NCM811 cathode surface. c) XPS depth spectra of O 1s at the surface of bare $LiNi_{0.80}Co_{0.15}Mn_{0.05}O_2$. d) The discharge capacity of an NCM811/Li cell before and after washing with water and discharge stability of a $LiNi_{0.80}Co_{0.15}Mn_{0.05}O_2$/graphite cell. e) Gas evolution after cycling 300 times for a bare $LiNi_{0.80}Co_{0.15}Mn_{0.05}O_2$ cathode and a washed one. a) Reproduced with permission.[32] Copyright 2016, Elsevier. b,d) Reproduced with permission.[33] Copyright 2018, Elsevier. c–e) Reproduced with permission.[34] Copyright 2018, Wiley-VCH.
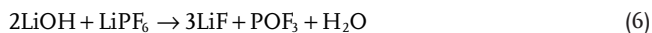
Figure 5a shows a schematic representation of RLCs growth at a Ni-rich cathode surface.[32] The actual composition and amount of surface impurities vary with the synthesis parameters and storage conditions, such as temperature and air humidity. This Li-salt layer can be detected by transmission electron microscopy (TEM), as shown in Figure 5b. The lattice spacing of 2.35 Å is assigned to the (012) plane of the layered NCM811 material. An inhomogeneous Li-salt layer can be observed at the surface with a thickness around 3 nm. X-ray photoelectron spectroscopy (XPS) depth profile was also employed on a pristine $LiNi_{0.80}Co_{0.15}Mn_{0.05}O_2$ material (Figure 5c). In the O 1s spectra, the peak located at 531 eV is attributed to Li_2CO_3 (or LiOH), and the peak at 528.8 eV is the binding energy of TM–O in NCM. The peak intensities expose the amount and distribution of RLCs with sputtering depth, revealing the enrichment of the impurities at the NCM surface.

Many studies have confirmed that the generation of RLCs surface layers is detrimental to the performance of Ni-rich cathodes. The most efficient and feasible way to remove RLCs from the surface is by the water washing method. However, the washing will lead to capacity losses (Figure 5d), as water tends to react with the active electrode material at the subsurface and partially destroy the material's crystalline structure, which is a kind of tradeoff.[33] Moreover, the water washing process also increases the sensitivity of Ni-rich cathodes to air, so careful control of washing parameters is required. Though the washing treatment leads to a reduced storage capacity, it offers enhanced electrode stability and moderate gas evolution compared in comparison to untreated electrode materials.

The study of Park et al. demonstrates that the total amount of gas evolution was reduced by 25% for treated samples after 300 cycles in a $LiNi_{0.80}Co_{0.15}Mn_{0.05}O_2$/graphite cell (Figure 5e).[34] The accumulation of gas in a battery places a considerable safety hazard. The gas generation in the battery predominantly arises from the reaction between RLCs and the electrolyte as well as phase transitions inside the electrode material. The latter factor will be illustrated in details in the following section,

ADVANCED
SCIENCE NEWS
www.advancedsciencenews.com

ADVANCED
ENERGY
MATERIALS
www.advenergymat.de

while the mechanism of RLCs reacting with electrolyte during cycling has been described reaction sequence[34]

$$2LiOH + LiPF_6 \rightarrow 3LiF + POF_3 + H_2O \qquad (6)$$

$$LiPF_6 + H_2O \rightarrow LiF + OPF_3 + 2HF \qquad (7)$$

$$Li_2CO_3 + 2HF \rightarrow 2LiF + H_2O + CO_2 \qquad (8)$$

3.1.2. Cation Disorder

Cation disorder is a phenomenon also known as Li/TM ions mixing in Ni-rich layered cathodes. Among the basic cations in Ni-rich cathodes, such as Ni^{2+}, Co^{3+}, Mn^{3+}, Al^{3+}, etc., Ni^{2+} ions show a high propensity to mix with Li^+ ions due to the similar ionic radii of Ni^{2+} (0.69 Å) and Li^+ (0.76 Å) cations. Such mixing leads to crystal structure transformation from a pristine layer via a spinel phase to the final rock-salt phase. The Li-ion mobility will be hindered due to this cation disordering, thus reducing the rate capability of Ni-rich cathodes. It is worth noticing that cation disorder is observed during the synthesis process and exits throughout the whole battery life. This Li/Ni mixing tendency becomes much more frequent with increasing Ni-ratio, operation temperature, cut-off voltage, and SOC.

Finding a suitable reactant ratio between the TM-precursor and lithium salt is the starting point for restraining TM migration during calcination. Chu and co-workers recently investigated the influence of the Li-excess during calcination on the Li/TM mixing.[35] The schematic diagram shown in **Figure 6**a shows that the samples prepared with Li/TM ratios of 1.00, 1.06, and 1.12 are denoted by E00, E06, and E12, respectively. It is found that the Li slab in the lattice will experience shrinkage under both Li-loss (E00) and Li-excess (E12) conditions. For the E00 Li-loss sample, lithium volatilization during calcination will cause unoccupied defects in the sample. A large number of defects in lattice lead to contraction of the Li slab and eventually create severe Li/TM disorder. For the E12 Li-excess sample, the extra Li will partially occupy TM (3b) sites. The introduction of slightly larger Li^+ ions leads to larger TMO_6 octahedrons, expanding the distance between TM slabs and contracting the Li slab resulting in Li/TM disorder. Only the sample with the most optimal Li/TM ratio (E06) shows a broader Li slab. The expansion of the Li slab and shrinkage of TMO_6 will guarantee better Li-ion diffusion.

In situ XRD is a proper method to diagnose cation disorder and can even provide quantitative analyses.[36] The relative intensity ratio between the (003) and (104) plane reflection ($R = I_{(003)}/I_{(104)}$) reveals the degree of cation disorder in the bulk of the material. Figure 6b illustrates the positions of the (003) and (104) planes in the lattice, where TM ions, Li^+ ions, and O ions are evenly distributed in the (104) planes, making the reflection of (104) independent of the ordering. In contrast, the reflection of the (003) plane is highly sensitive to cationic ordering. When Li/Ni mixing occurs in the crystal, the X-ray reflection intensity of the (003) plane will reduce, leading to a decrease of the R-value. 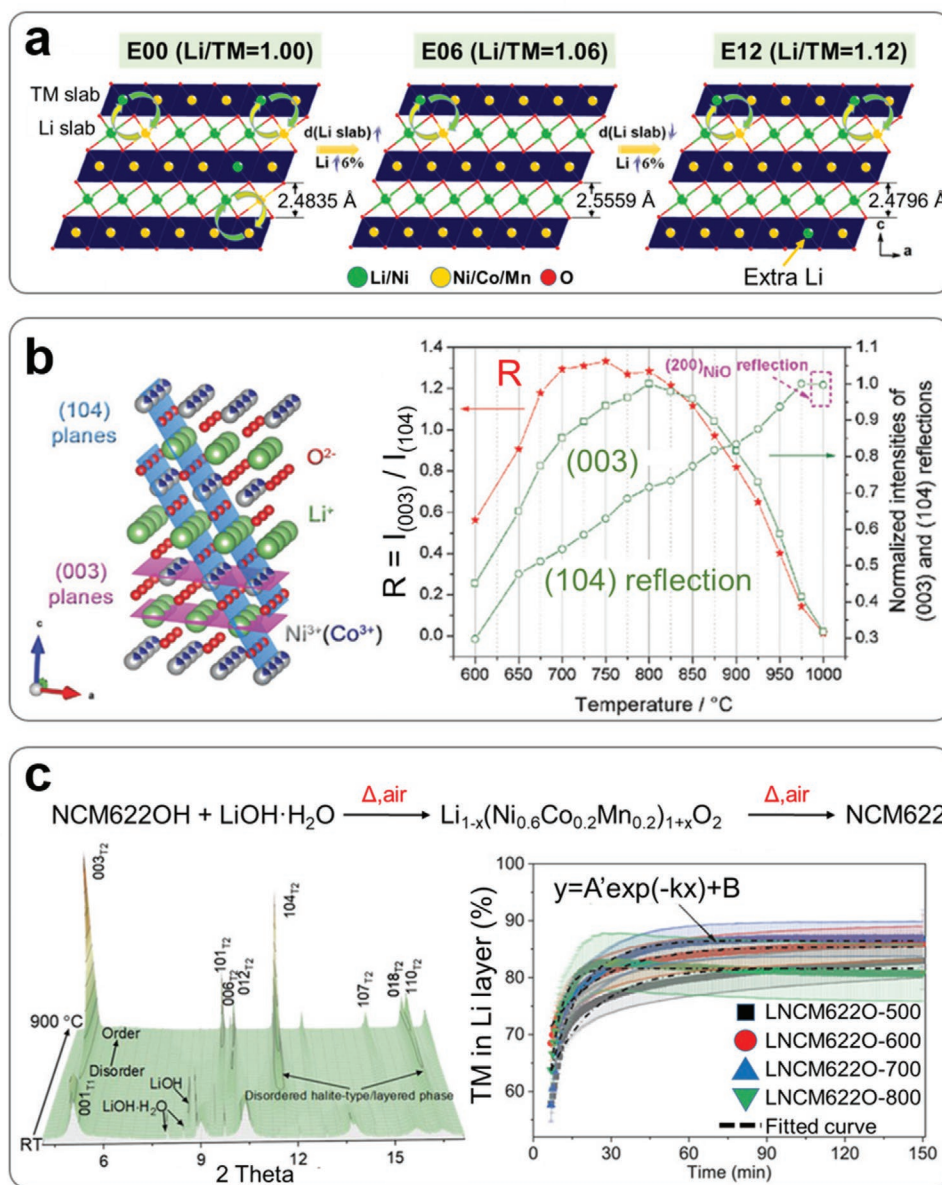Thus, a preliminary determination on the degree of cation disorder can be obtained from the XRD result through the peak intensity ratio between the (003) and (104) plane. Wang and co-workers applied in situ XRD to study the structural ordering evolution of $LiNiO_2$ and $LiNi_{0.8}Co_{0.2}O_2$ during calcination.[36] Their results highlight Co substitution's significance in facilitating the initial nucleation of Li-deficient layered structure at low temperatures and restraining the cation disorder at high temperatures.

The cation disorder is also detectable during the high-temperature lithiation reaction of the calcination process. Liu and co-workers employed in situ high-temperature synchrotron radiation diffraction (HTSRD) to systematically investigate the nonequilibrium formation of layered NCM622 (Figure 6c).[37] The starting reactants are the TM-hydroxide $Ni_{0.6}Co_{0.2}Mn_{0.2}(OH)_2$ (NCM622OH) precursor with trigonal layered structure ($P\overline{3}m1$, T1 phase), and lithium source $LiOH \cdot H_2O$. The in situ HTSRD pattern shows that the characterized reflections of NCM622OH gradually disappear when the temperature increases to 300 °C. Furthermore, a metastable layered $Li_{1-x}(Ni_{0.6}Co_{0.2}Mn_{0.2})_{1+x}O_2$ with a higher degree of Li/TM exchange of about 30% is detected at around 500 °C. The Li/TM exchange ratio can be obtained from the c/a ratio calculation, as presented in the previous paragraph. With further increasing the temperature up to 900 °C, a well-defined trigonal layered phase NCM622 can be indexed. Based on this investigation, it has been identified that complex reactions occur between the TM-precursor and lithium sources during the thermal treatment in the air. Three dominant components (NCM622OH, $Li_{1-x}(Ni_{0.6}Co_{0.2}Mn_{0.2})_{1+x}O_2$, and NCM622) have been identified throughout the process. Additionally, it is shown that a longer thermal treatment time should be considered at lower heating temperatures to stabilize the final structure. Therefore, it is important to carefully control the heating temperature and duration time to mitigate the cation disorder degree of Ni-rich cathodes. Noteworthily, the synthesis of different Ni-rich cathodes may require a different set of heating parameters.

The visualization of Li/TM migration at an atomic scale has been realized by applying scanning transmission electron microscopy (STEM). Based on the STEM measurements, Zhang and co-workers proposed two possible TM ions migration pathways, as illustrated in **Figure 7**a.[38] The first process is "single TM migration," where one single TM ion migrates to the nearest surface vacancy of the Li site (V_{Li}). The second process is "TM–O comigration," when a single TM ion migrates to the nearest surface V_{Li}, and the nearest O ion migrates to the outermost layer simultaneously. Among all TM–O comigrations, the Ni2–O migration was accompanied by the lowest formation energy, implying the higher tendency for Ni ions to migrate with O ions. In addition, Zhang and co-workers further divided the second process into three different trajectories: 1) single Ni-migration, 2) Ni–O comigration, and 3) O migration followed by Ni migration. Another enlightened work of the same group is the in operando observation of cation disorder, elaborating its impact on battery voltage decay.[39]

The high-angle annular dark-field STEM (HAADF-STEM) images of Figure 7b show the atomic arrangement as a function of measurement time, revealing the gradually increasing number of Ni_{Li} (migrated Ni ion) in Li sites during cation migration. Moreover, the authors observed that the TM

**ADVANCED
SCIENCE NEWS**

www.advancedsciencenews.com

**ADVANCED
ENERGY
MATERIALS**

www.advenergymat.de

Figure 6. a) Schematic diagram of NCM materials with different Li/TM ratios of 1.00 (E00), 1.06 (E06), and 1.12 (E12) in LiMO$_2$. b) Illustration of the atomic configuration and evolution of the intensity of the (003) and (104) reflections during synthesis of LiNi$_{0.8}$Co$_{0.2}$O$_2$. c) In situ HTSRD pattern evolution during NCM622 synthesis and the evolution of cation disordering as a function of reaction time. a) Reproduced with permission.[35] Copyright 2020, American Chemical Society. b) Reproduced with permission.[36] Copyright 2017, Wiley-VCH. c) Reproduced with permission.[37] Copyright 2021, Wiley-VCH.

migration gives rise to some fluctuation of Ni—O bond length (Figure 7c). The length of Ni—O changes in the range of 1.804–2.184 Å, corresponding to the rate of −10.2% to 8.6% in comparison to the pristine Ni—O length (2.010 Å). They further performed calculations of the energy bands of LiNiO$_2$ with the pristine Ni—O bond length, increased Ni—O bond length (+8%), and decreased Ni—O bond length (−8%). The 0% pristine length is defined by the primitive LiNiO$_2$ cell, taken from the DFT simulation package. The calculation results reveal that the changes of Ni—O bond length (+8% and −8%) will both ultimately lift the energy density of e$_g$* antibonding orbits

($3d_z^2$–2p)* in the NiO$_6$ octahedrons. Given the fact that the thermodynamic equilibrium voltage of a full-cell is determined by the energy gap between Li 2s and the highest occupied molecular orbital (HOMO) energy level (($3d_z^2$–2p)* in NiO$_6$), lifting the HOMO level will ultimately result in a cell voltage decline.

3.1.3. Surface Reconstruction

Surface reconstruction in Ni-rich cathodes is related to a phase transition process, mostly at the material's surface. During this
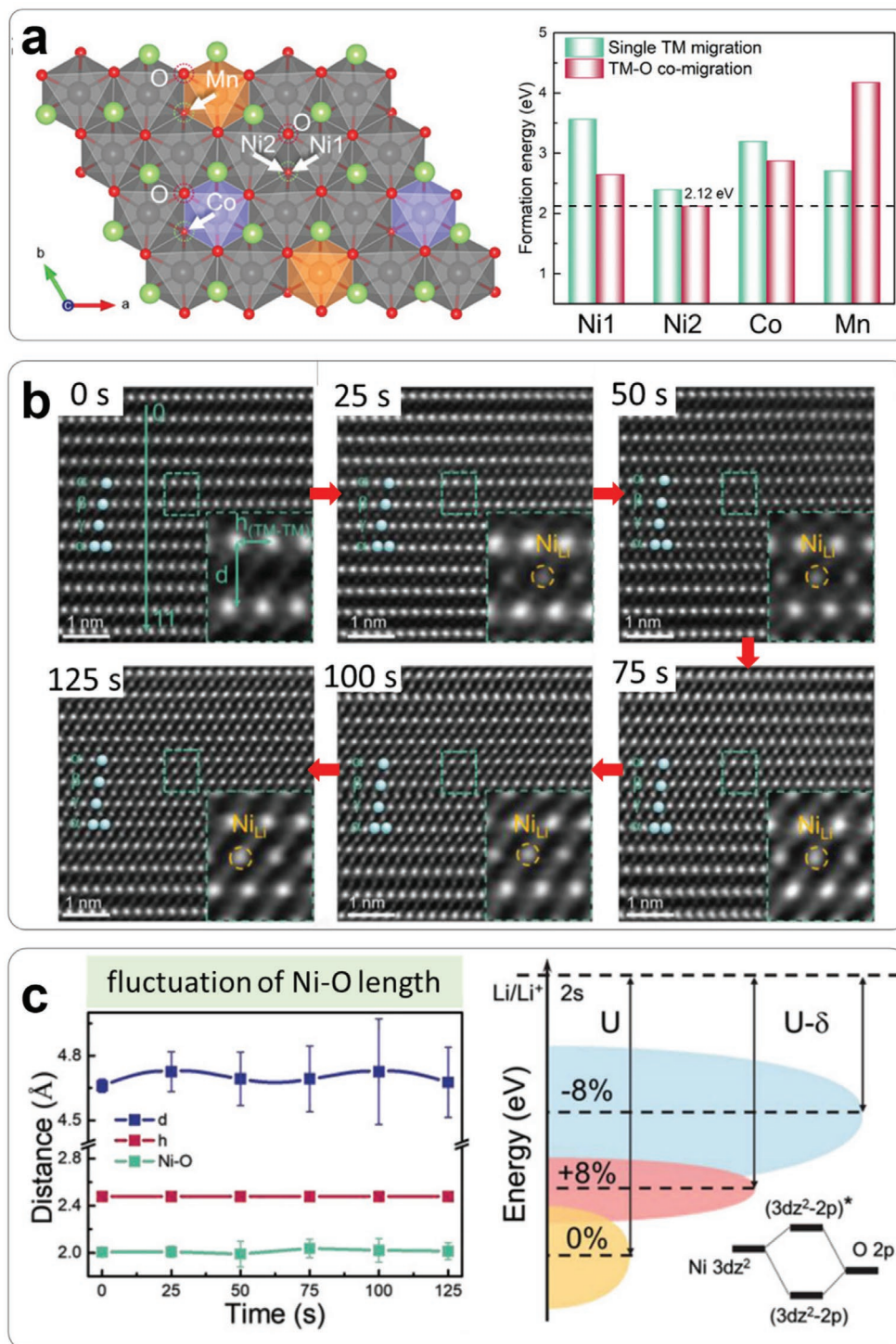
Figure 7. a) Schematic representation of the outward migration paths of TM and O ions along the out-of-plane direction and the formation energy of "single TM migration" and "TM–O comigration." b) Evolution of atomic arrangements during TM migration viewed along the [110] orientation. c) Evolution of the average interlayer distance between TM slabs (d), spacing distance between two TM ions (h), and Ni–O length during TM migration. Schematic diagram of e_g^* antibonding orbits hybridized by Ni $3d_z^2$ and O 2p orbits in NiO_6 octahedron with different Ni—O bonds. a) Reproduced with permission.[38] Copyright 2021, Wiley-VCH. b,c) Reproduced with permission.[39] Copyright 2020, Wiley-VCH.
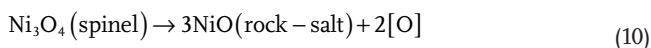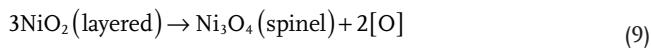
phase transition, the original crystal structure changes from layered-structured to spinel and eventfully to rock-salt. Typical differential capacity profiles can be observed at the highly

delithiated state, as previously shown in Figure 4a, suggesting that the H2-to-H3 transition is responsible for this process.[40] This transformation is the combined impact of cation disorder and
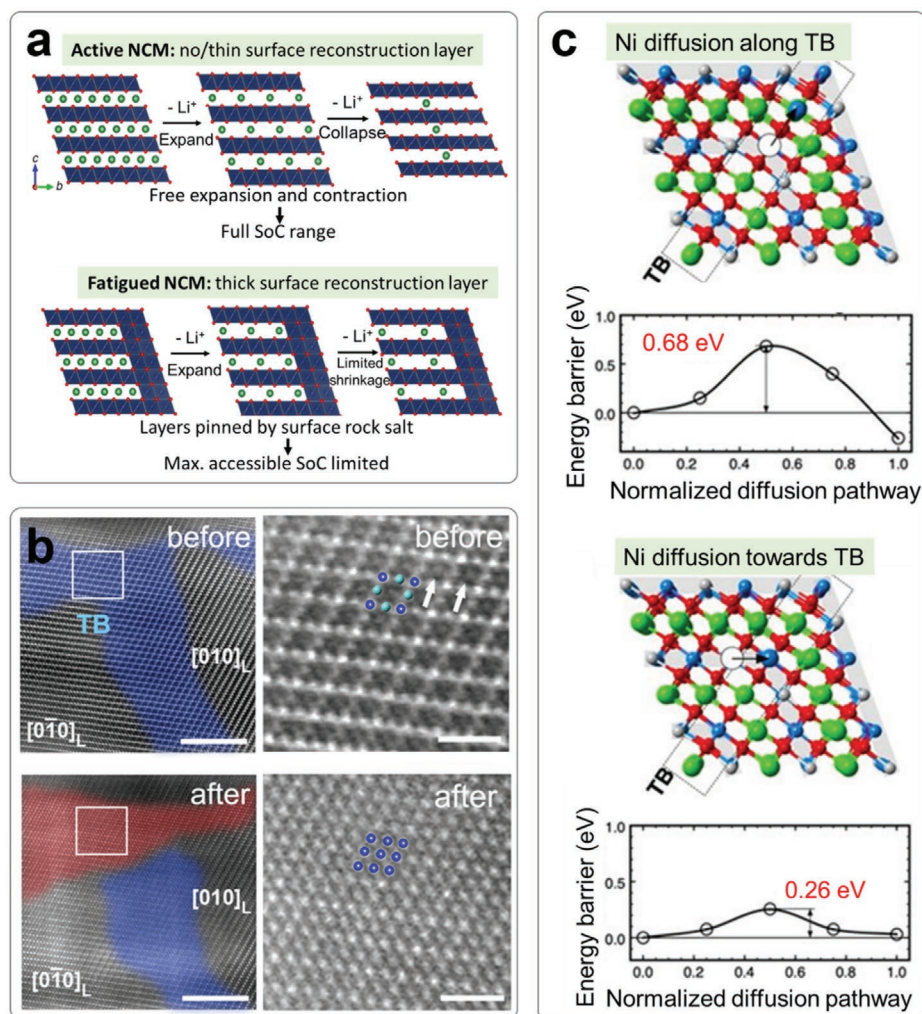
Figure 8. a) Illustrations of the NCM811 structural evolution of the active and fatigued phase during delithiation. b) HAADF-STEM images before and after delithiation of NCM76 surface. c) The kinetics of a series of reaction steps required by the layered → rock-salt phase transformation. a) Reproduced with permission.[15] Copyright 2021, Nature. b,c) Reproduced with permission.[42] Copyright 2020, Wiley-VCH.

lattice oxygen loss and is accelerated at high Ni-content, high SOC, and high temperatures. The following equations describe this transition[41]

$$3NiO_2 (layered) \rightarrow Ni_3O_4 (spinel) + 2[O] \qquad (9)$$

$$Ni_3O_4 (spinel) \rightarrow 3NiO(rock-salt) + 2[O] \qquad (10)$$

The formed rock-salt phase has poor Li transportation kinetics, resulting in blocking Li-ion diffusion paths and reducing ionic conductivity. The NiO-like rock-salt phase in the surface reconstruction layer grows epitaxially on the edge of aged Ni-rich cathodes. Grey and co-workers proposed a surface reconstruction-driven degradation mechanism for NCM811 by applying in situ synchrotron-radiation powder X-ray diffraction (SR-PXRD).[15] During the long-duration electrochemical cycling experiments, the phase fraction obtained for the aged NCM811 cathode reveals a growing proportion of fatigued phase. In contrast, the amount of electrochemically active phase is decreasing. In the fatigued phase, the layered structure in the bulk material will be pinned by the thick rock-salt surface layer due to the high interfacial lattice strain, as illustrated in **Figure 8**a. Thus, the Li slab is prevented from contracting further, making the active Li+ trapped in the lattice, which is no longer available to participate in the delithiation process at the higher SOC. Their analysis indicates the lattice mismatch between the layered and rock-salt phases developing after intensive cycling of Ni-rich cathodes, restricting the reversible SOC range to 75%. Attempts to reach higher SOC values by applying higher cut-off voltage lead to even larger lattice mismatches and even more rapid electrode degradation.

Some studies also demonstrate that phase transitions can already be detected before lithiation occurs at the material surface. Su and co-workers investigated the structural evolution close to the surface region at the atomic scale by in situ TEM.[42] They confirmed that crystallographic defects in pristine materials could trigger the formation of additional phases and distinct boundaries between three phases (layered, spinel, rock-salt). These intrinsic defects enable the appearance of a broad

**ADVANCED
SCIENCE NEWS**

www.advancedsciencenews.com

**ADVANCED
ENERGY
MATERIALS**

www.advenergymat.de

area with a spinel phase even before lithiation. Subsequently, the rock-salt phase starts growing and keeps propagating after lithiation (Figure 8b). According to these observations, the structural changes tend to evolve along with planar defects. DFT calculations suggest that the existence of a coherent twin boundary (TB) in the crystal reduces the energy barrier of cation migration and provides a more feasible pathway for Li/TM diffusion (Figure 8c). This work reveals that intrinsic crystallographic defects in Ni-rich cathodes significantly influence the layer-spinel-rock-salt phase transformation. Additionally, Wang and co-workers observed that evolution of the rock-salt phase upon electrochemical cycling can also develop along the grain boundaries in $LiNi_{0.76}Mn_{0.14}Co_{0.10}O_2$ (NMC76) (**Figure 9**a).[43] Apart from the crystallographic defects in the primary particles, structural reconstruction is also escalated by the direct contact with the liquid electrolyte and oxygen depletion in the crystal lattice.

Surface reconstruction is generally considered as an unfavorable consequence of electrochemical cycling in Ni-rich cathodes. Studies have shown that this layer is already formed during the synthesis process and found in freshly prepared samples. Interestingly, the formation of this surface reconstruction layer (SRL) is facet-dependent. Chen and co-workers reported that the surface layer was selectively constructed on the non-(001) surface at the pristine NCM622 particles. In contrast, no such layer is observed at the (001) surface.[44] As shown in Figure 9b, Li loss occurs during the heating treatment at the non-(001) surface, leaving behind Li-vacancies in the lattice. The Li loss is accompanied by O losses. These vacant sites then become available for the development of defects for Li/Ni mixing. At the same time, at the (001) surface, the TM–O–Li layers significantly hinder such evolution, resulting in a negligible formation of surface reconstruction layers (Figure 9c).

3.1.4. Gas Release

The gas releasing problem is the most hazardous safety issue in LIBs. The reactions involved in the gas release are typically exothermic, triggering a series of chain reactions and eventually leading to a severe risk of catastrophic self-combustion of the battery.[45] The gaseous decomposition products are generally CO_2 and O_2. In Ni-rich cathodes, the origins of gas generation arise from three aspects, as schematically shown in **Figure 10**a: 1) Electrolyte/surface mixed reactivity, including lattice oxygen loss induced by the structural defects (cation disorder and surface reconstruction as discussed above), lithium hydroxides, and unreacted precursors at the surface; 2) decomposition of Li_2CO_3 and reaction with the electrolyte; 3) direct electrolyte oxidation.[46]

High SOC will accelerate gas generation due to the presence of surface defects. A high delithiation state also stimulates electrolyte decomposition reactions. Washing has been frequently used to alleviate such side effects as the gaseous products that stem from surface contaminations. Studies have confirmed that different solvents and procedures used in the washing process will result in various surface contaminations compounds, leading to diverse gas evolution behavior. Renfrew and McCloskey employed various washing treatments to study the impact of surface contamination on the gas evolution in delithiated

NCM622 (Figure 10b).[47] They prepared NCM622 samples with different treatments (^{18}O-NCM622, ^{18}O-MeOH, ^{18}O-H_2O, ^{18}O-soak, Li_2CO_3-^{18}O, and H_2O-^{18}O) and kept the cathodes at 4.8 V for a long time while monitoring the gas evolution. It turns out that the sample with H_2O soaking treatment (^{18}O-soak) shows the smallest gas evolution and capacity loss. Their results indicated rather complex gas generation mechanisms depending on surface contaminants and defects. Thus, a proper surface pretreatment is necessary for reducing overall gas formation.

O_2 and CO_2 gas evolution in the battery system are significantly accelerated under high voltage operation. As shown in Figure 10c, the gas formation at the NCM622 electrode was investigated by applying differential electrochemical mass spectrometry (DEMS) under potentiostatic control at 4.8 V.[47] Interestingly, the CO_2 and O_2 evolution exhibit diverging behaviors. The O_2 evolution rate reached a maximum at the end of galvanostatic charging at 4.8 V and dropped during the potentiostatic period as the current fell. In contrast, the CO_2 evolution rate continues to rise at the beginning of the potentiostatic period. It starts to drop only after ≈1 h. This trend suggests that the amount of O_2 evolution is closely related to the lattice defection at the outermost surface, influenced by the delithiation depth. The CO_2 evolution mostly depends on the decomposition of Li_2CO_3 (and electrolyte) at the cathode surface. This conclusion has been further confirmed by growing a surface carbonate layer and studying these materials as a function of various cut-off voltages. The surface carbonate layer has already been detected at 3.9 V, while the onset voltage of O_2 lattice loss was found at around 4.45 V. Most of the electrolyte degradation products will stem from the surface after discharge. On the contrary, the formation of the surface disorder layer is irreversible and can persist at the electrode surface.

It has been widely accepted that the complex interaction between surface reconstruction and interface reactivity results in gaseous decomposition products. Apart from the decomposition of surface impurity products, CO_2 generation could also originate from phase transformation at the electrode surface. **Figure 11**a schematically shows these reactions at the electrode surface, as found by Berg and co-workers.[48] On the one hand, partly oxidized surface oxygen reacts with organic carbonate electrolytes, such as ethylene carbonate (EC), dimethyl carbonate (DMC), diethyl carbonate (DEC), etc., which results in CO_2 generation. On the other hand, lattice oxygen losses induced by structural transformations ($LiMO_2 \rightarrow MO$ or M_3O_4) lead to O_2 evolution. Additionally, the evolving CO_2, O_2, and R–O intermediates generated from electrolyte decomposition are known to be strongly reactive toward electrolyte solvents, contributing to the formation of the surface inactive layer. Analysis based on the electrochemical mass spectroscopy (EMS) shows that the onset point of gas formation falls within a narrow range of Ni-oxidation state (85–100%). Higher Ni-content facilitates gas formation (Figure 11b). The authors also presented electronic density of state (DOS) calculations for NCM111 and NCM811 at three different states, as illustrated in Figure 11c. They concluded that the rate of gas formation (CO_2 and O_2) is mainly determined by the rate of electron depletion from Ni–O_2* surface state. To a smaller extent, it is affected by the competitive Co t_{2g} bulk oxidation and Co–O_2* surface states.
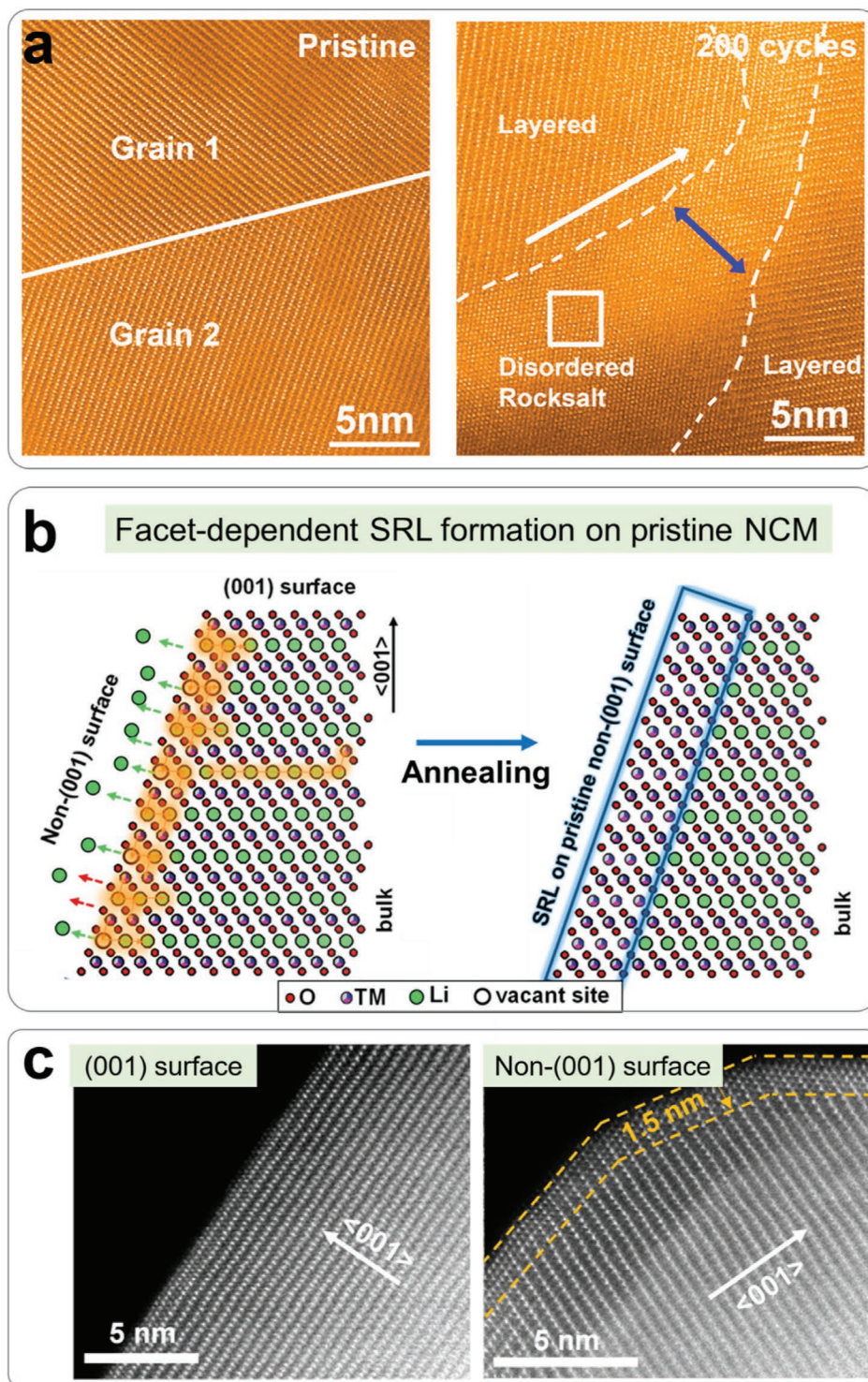
Figure 9. a) HAADF-STEM images of a twin boundary in pristine and cycled NMC76. b) Schematic representation of the annealing process that leads to surface reconstruction layer (SRL) growth at the pristine NMC surface. c) HRTEM images at the (001) surface and non-(001) surface. a) Reproduced with permission.[43] Copyright 2020, American Chemical Society. b,c) Reproduced with permission.[44] Copyright 2020, American Chemical Society.

3.1.5. Transition Metal Dissolution

The dissolution of transition metal ions from the cathode into electrolyte is an inevitable process, resulting in capacity degradation because of the loss of Li-ion insertion sites in the host structure. It is mainly triggered by corrosion of electrolyte decomposition byproducts, such as HF and HClO₄. It accelerates at elevated temperatures and high operating voltages. It is

ADVANCED
SCIENCE NEWS

www.advancedsciencenews.com

ADVANCED
ENERGY
MATERIALS

www.advenergymat.de
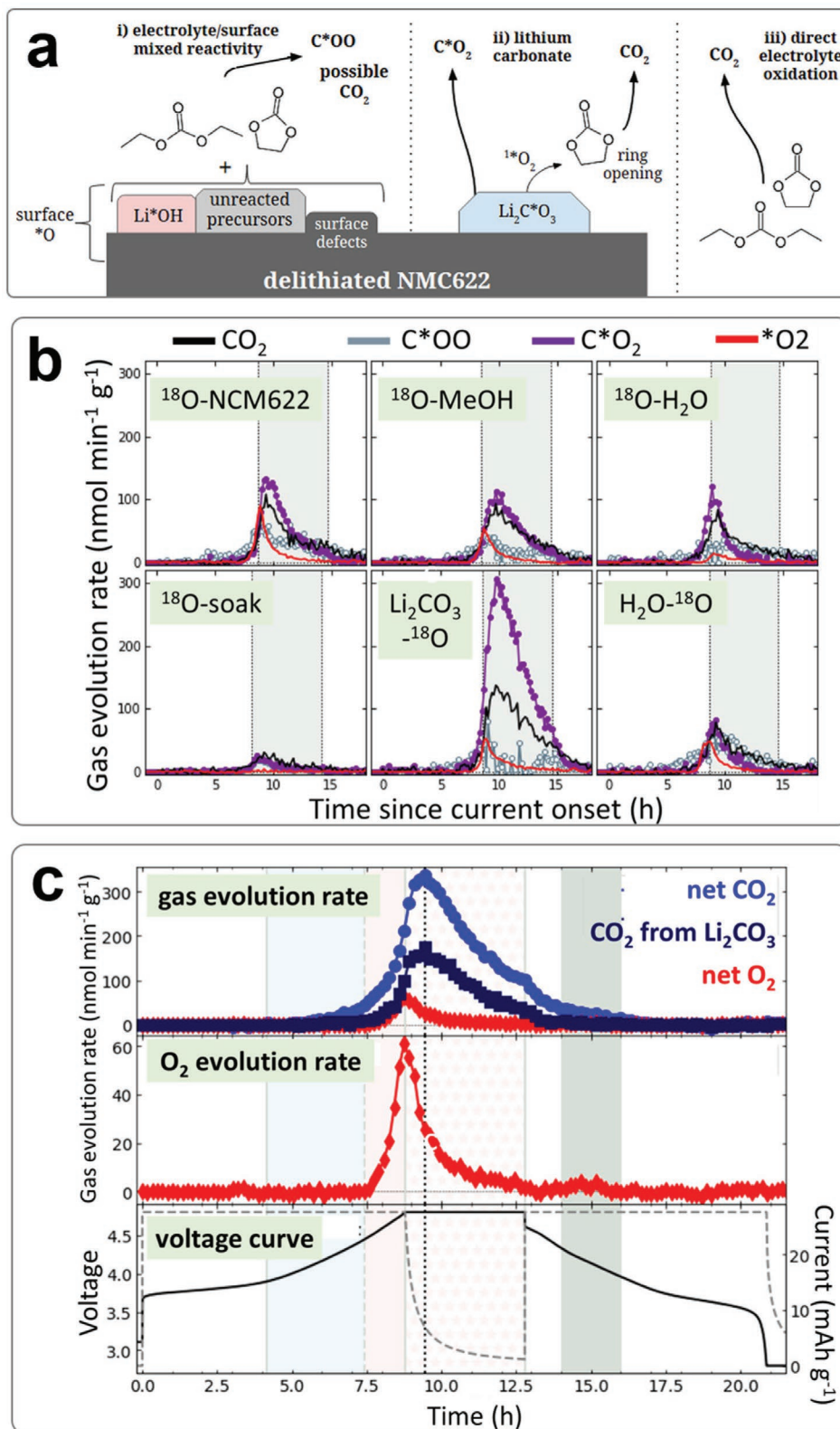
Figure 10. a) Possible reaction routes for gas formation at the surface. b) Rate of $*O_2$ and carbon dioxide evolution for NMC622s under various treatments (^{18}O-NCM622: the baseline sample synthesized via conventional procedure; ^{18}O-MeOH: sample treated by methanol rinsing; ^{18}O-H_2O: sample treated by H_2O rinsing; ^{18}O-soak: sample treated by H_2O soaking; Li_2CO_3-^{18}O: sample treated by Li_2CO_3 enriching; H_2O-^{18}O: sample treated by H_2O washing and ^{18}O enriching). c) Gas evolution and corresponding voltage profiles for NMC622. a,b) Reproduced with permission.[46] Copyright 2019, American Chemical Society. c) Reproduced with permission.[47] Copyright 2019, American Chemical Society.
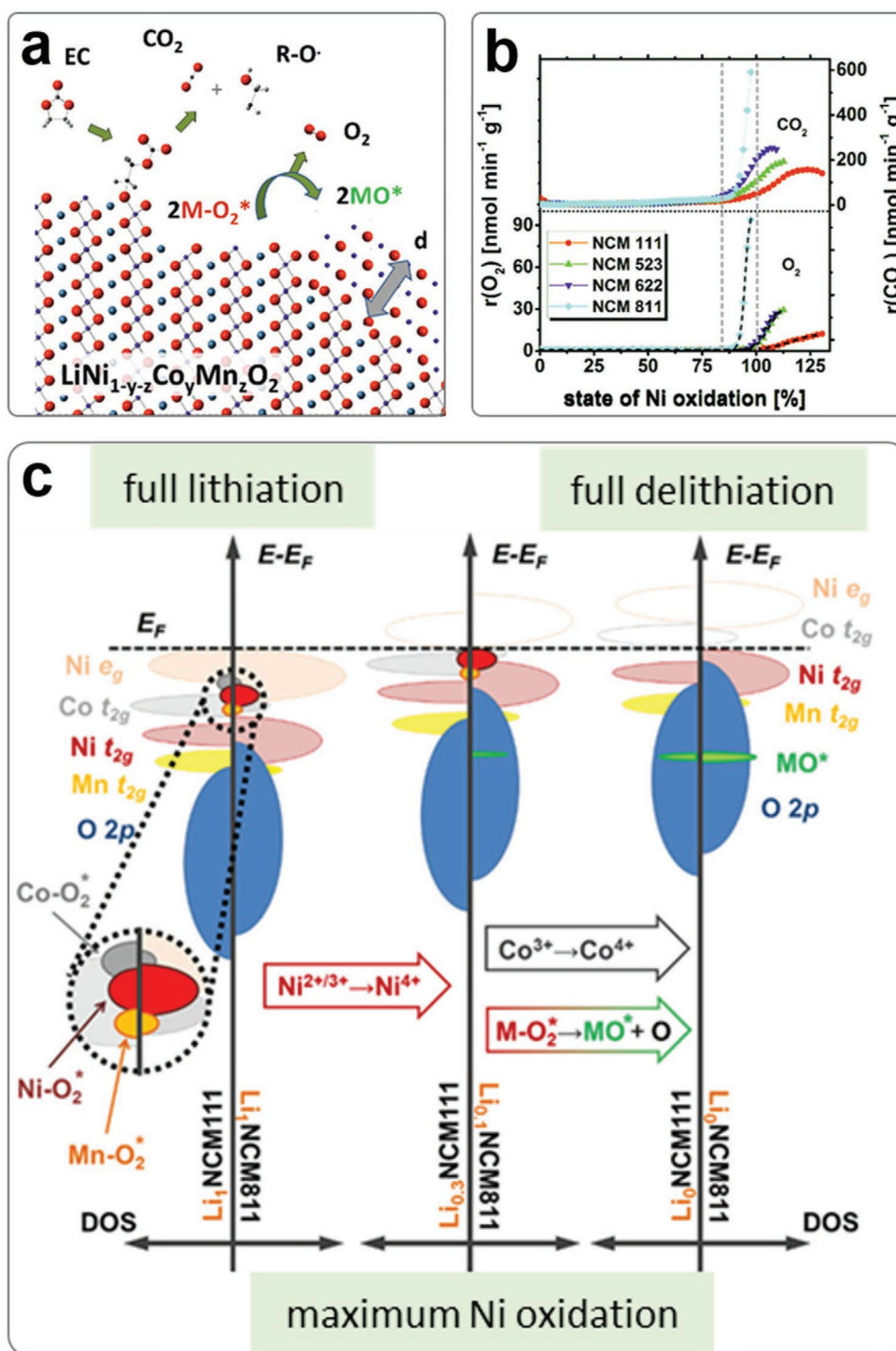
Figure 11. a) Schematic representation of selected reactions resulting in gas formation. b) The dependence of gas evolution on the state of Ni oxidation. c) Qualitative DOS diagrams for NCM111 and NCM811 at full lithiation, maximum nickel oxidation, and complete delithiation. a–c) Reproduced with permission.[48] Copyright 2017, American Chemical Society.

widely acknowledged that the electrolyte solvents might contain traces of water during manufacturing, which react with lithium salts ($LiPF_6$ or $LiClO_4$), yielding acidic species. The related reactions can be described as follows[49]

$$LiPF_6 + H_2O \rightarrow LiF + HF + POF_3 \tag{11}$$

$$LiClO_4 + H_2O \rightarrow LiCl + HClO_4 \tag{12}$$
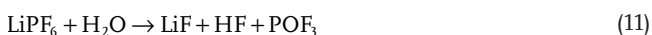
Alternatively, the generation of HF and $HClO_4$ can arise from reactions between organic solvents and PF_6^- or ClO_4^-, such as the one-electron oxidation of $EC\text{-}PF_6^-$. Transition metal dissolution might also occur due to the formation of low valence ions

**ADVANCED
SCIENCE NEWS**

www.advancedsciencenews.com

**ADVANCED
ENERGY
MATERIALS**

www.advenergymat.de
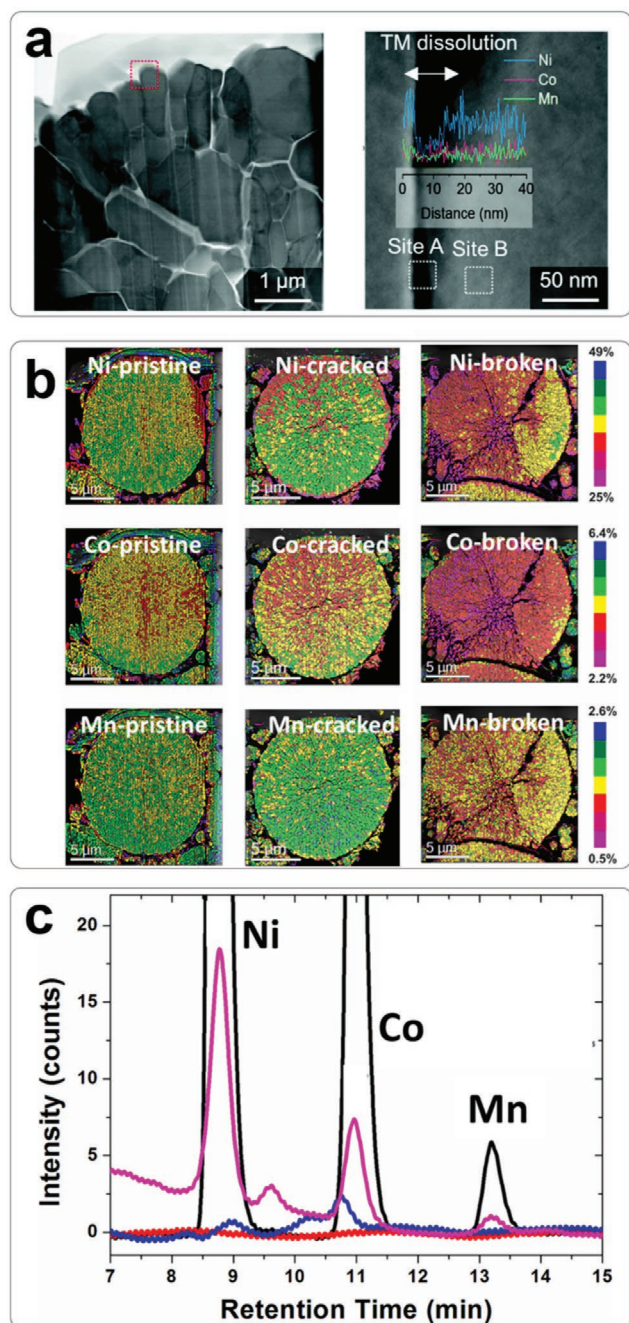
Figure 12. a) HAADF-STEM image and line EDX of cycled NCM811. b) Elemental mapping of Ni, Co, and Mn in $LiNi_{0.87}Co_{0.09}Mn_{0.04}O_2$ particles at pristine, cracked, and broken states. c) Ion chromatograms of the standard uncycled $LiNi_{0.87}Co_{0.09}Mn_{0.04}O_2$ cathode (black line) and the ion chromatograms of electrolytes obtained from the cells after zero (red line), two (blue line), and 500 (purple line) cycles. a) Reproduced with permission.[50] Copyright 2018, Royal Society of Chemistry. b,c) Reproduced with permission.[51] Copyright 2019, Elsevier.

caused by lattice oxygen loss during cycling. Metal ions with lower valence states are more soluble in the electrolyte than those with higher valence states.

Figure 12a presents evidence of transition metal dissolution in secondary particles after battery cycling.[50] The line energy
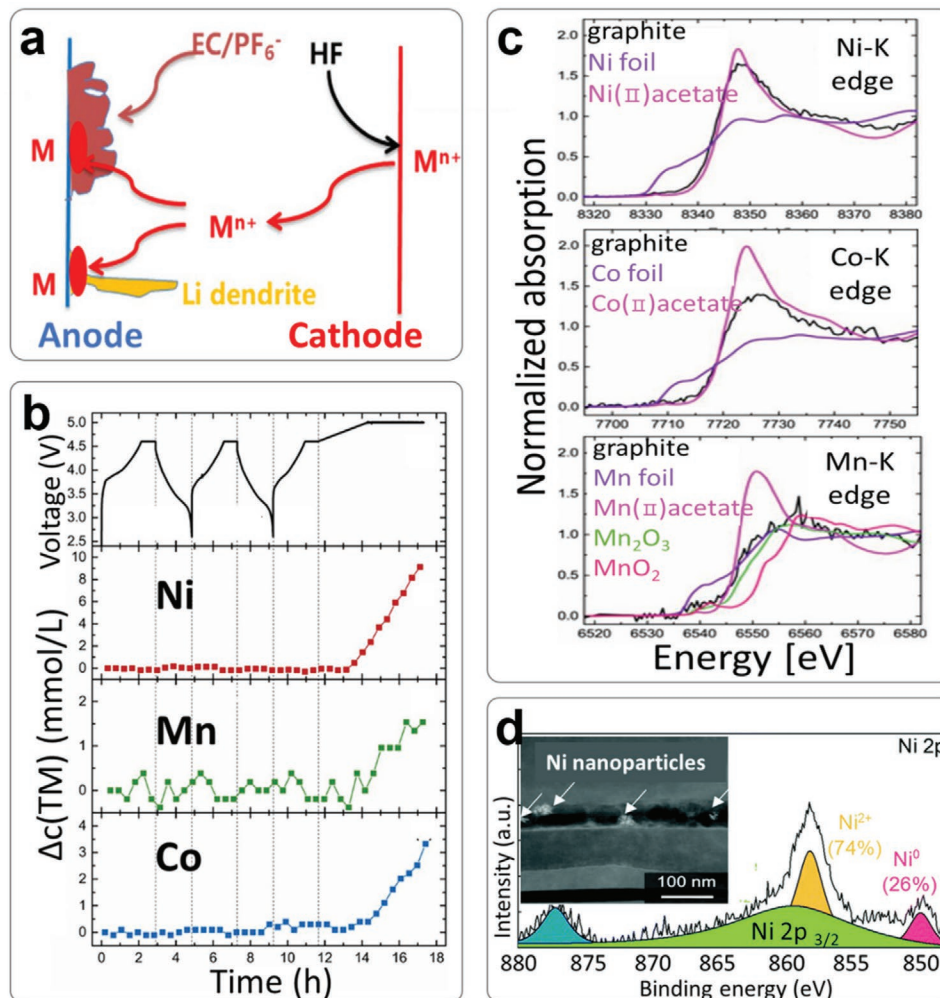
dispersive X-ray spectroscopy (EDX) results demonstrate severe deficiency of the metal ions at the particle surface, especially Ni ions. A similar trend can also be found by the corresponding sectionalized chemical composition maps of a single Ni-rich NCM particle in Figure 12b.[51] Compared with the pristine state, the particles in cracked and especially in the broken states demonstrate increasing transition metal deficiencies. Notably, the metal content decreases dramatically in the cracked and pulverized particles, suggesting that transition metal ions prefer to be released from the broken sites. The fractured particles reveal a larger specific surface area than the intact particles, which allowed a severe acid attack and more drastic dissolution of transition metals. Ion chromatograms of the electrolytes after zero (red), two (blue), and 500 cycles (purple) in Figure 12c imply that metal dissolution can be detected even at the beginning of battery cycling. Note that the black line is the standard chromatogram of the uncycled NCM powder.[51] The concentration of Ni ions in the electrolyte is much higher than Co and Mn, which further confirms the extreme instability of Ni at the surface.

The negative impact of transition metal dissolution is embodied both in the cathode and the anode side. As illustrated in **Figure 13**a, the dissolved metal ions can cross through the separator and deposit at the anode surface after a reduction during battery operation.[49] Up to now, several studies have demonstrated that the deposited metal nanoparticles might participate in the SEI formation and serve as catalysts for electrolyte reduction and lithium dendrite growth. Such side reactions will negatively influence the battery performance. Gasteiger and co-workers applied in situ X-ray absorption spectroscopy (XAS) measurements at NCM622-graphite cells to monitor the transition metal deposition at the anode.[52] The metal concentration evolutions at the graphite surface were recorded along with the charging and discharging process (Figure 13b). During the first two cycles up to 4.6 V, no significant increase of metal concentration can be detected at the graphite surface. That might be due to the detection limit of XAS measurements, considering that only a small amount of transition metal ions will be made available in the electrolyte at the beginning of cycling. With the voltage ramping up to 4.8 V, the concentration of deposited metal on graphite elevates intensively. Subsequently, the K-edge spectra of Ni, Co, and Mn at the graphite surface reveal TM ions' elemental valence state (oxidation state) at the graphite surface, as shown in Figure 13c. Based on the analysis of the XAS spectra, Ni and Co K-edges match the edge position of the +2 oxidation state. In contrast, the edge position of Mn is located between +2 and +3 and is challenging to distinguish. Cho and co-workers employed XPS and TEM measurements on the cycled graphite surface to investigate Ni deposition at the anode side.[50] The results reveal that Ni exists at graphite in the divalent and metallic states (Figure 13d). Interestingly, the metallic Ni nanoparticles can be observed to become part of the SEI film on the anode surface.

3.1.6. Intragranular and Intergranular Cracks

Mechanical failure of Ni-rich cathode particles, caused by the generation and development of cracks, has been widely considered a significant factor influencing battery degradation. The

**ADVANCED
SCIENCE NEWS**

www.advancedsciencenews.com
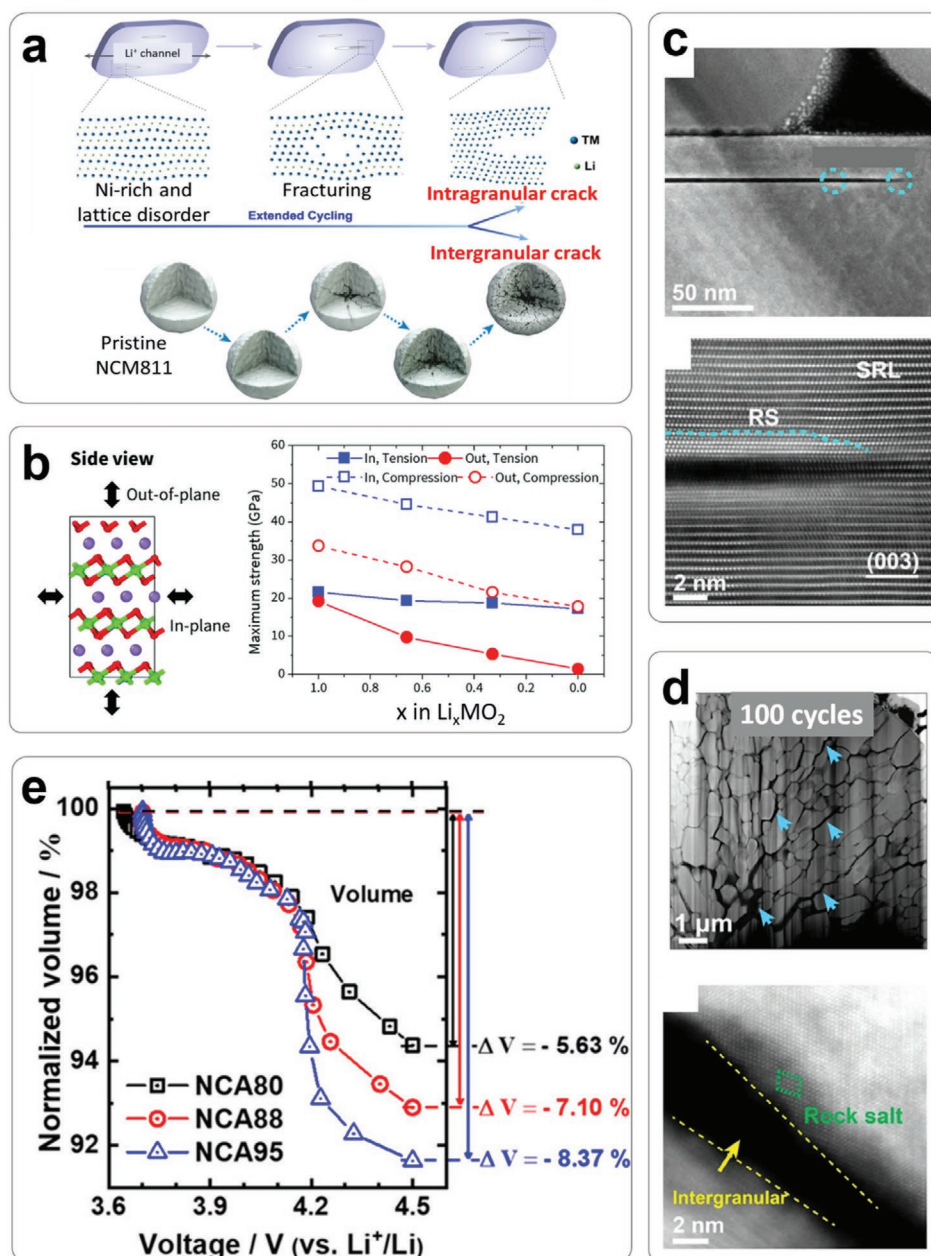
**ADVANCED
ENERGY
MATERIALS**

www.advenergymat.de

Figure 13. a) Schematic of the dissolution and deposition of TM ions from the cathode. b) Concentration changes of Ni, Mn, and Co on the graphite anode with the cycling of NCM622/graphite cell. c) XAS K-edge spectra of Ni, Co, and Mn on the lithiated graphite anode. d) XPS spectra and cross-section TEM image of graphite anode in cycled NCM811/graphite cell. a) Reproduced with permission.[49] Copyright 2020, The Electrochemical Society. b,c) Reproduced with permission.[52] Copyright 2019, The Electrochemical Society. d) Reproduced with permission.[50] Copyright 2018, Royal Society of Chemistry.

presence of particle cracks can be related to many reasons, such as lattice collapse, phase transformation, cation disorder, lattice oxygen loss, surface reconstruction, and heterogeneous lithiation/delithiation.[53] According to their positions, the cracks can be classified as intragranular or intergranular cracks, as illustrated in **Figure 14**a.[54] Intragranular cracks are commonly induced by Ni–Li antisite defects and lattice disorder, as well as Columbic repulsion between ions. The lattice deficiencies in the pristine particles keep growing during extended cycling and eventually develop into nanoscale cracks. In contrast, mechanical failure in intergranular cracks is initiated from the inner central particle area and spreads toward the surface. The generation of such cracks is mostly caused by the random crystal orientation of particles, which leads to anisotropic volume changes during cycling.

Min and Cho performed first-principles calculations on NCM811 cathode material in the case of the formation of intragranular cracks and found an interesting mechanic anisotropy.[55] Tensile and compressive stress calculations were performed to simulate the delithiation process in the layered structure. In-plane and out-of-plane mechanical deformations are initiated from two directions. Their results indicate that the maximum strength change in the material is not homogeneous. The out-of-plane stress is always weaker than those from the in-plane (Figure 14b). The subsequent accumulation of this strain unbalance during repeated lithiation and delithiation of the electrodes will lead to mechanical fatigue, finally resulting in intragranular cracks.

More detailed structural information about intragranular cracks can be obtained by atomic resolution techniques, such as shown in the HAADF-STEM images in Figure 14c.[54] In the fracture region, a rock-salt phase has been found in the surface reconstruction layer located at the crack's edge. Such observation suggests that the cracks initiate and grow inside the rock-salt phase. Notably, with the increasing cycles, the length of the intragranular crack along the (003) plane can reach around 440 nm. Compared

**ADVANCED
SCIENCE NEWS**

www.advancedsciencenews.com

**ADVANCED
ENERGY
MATERIALS**

www.advenergymat.de

Figure 14. a) Schematic representation of microstructural features of intragranular and intergranular cracks. b) Illustration of the directions of tensile and compressive deformation and strength changes for NCM811 under the delithiation process. c) HAADF-STEM images of an intragranular crack in cycled NMC811 (RS: rock-salt; SRL: structural reconstruction layer). d) HAADF-STEM images of intergranular cracks in cycled NMC811. e) Lattice parameter evolution of Ni-rich NCA electrodes during the first charging cycle. a,c,d) Reproduced with permission.[54] Copyright 2020, Elsevier. b) Reproduced with permission.[55] Copyright 2018, Royal Society of Chemistry. e) Reproduced with permission.[56] Copyright 2019, American Chemical Society.

with intragranular cracks, intergranular cracks are more observable, especially for the intensively cycled particles. Figure 14d displays cross-section images of the particles obtained under various cycling conditions. After 200 cycles, large amounts of the anisotropic cracks are observed, demonstrating severe pulverization and mechanical failure of material particles. Besides, the structural reconstruction layer with the inactive rock-salt phase formed at the surface can also be detected at the edge of the intergranular crack. Such a reconstruction layer on the primary particle in the cracking area has an estimated thickness of around 30 nm.

The cracking phenomenon has been frequently discussed in the literature and represents a combined effect of intra- and intergranular cracking.[57] The degree of cracking becomes considerable with higher Ni-content, increasing cycling number, and higher SOC. Sun and co-workers studied the cracking evolution of Ni-rich NCMs with various Ni-content.[18] They identified significant anisotropic shrinkage that occurs during the delithiation process in the compounds with a Ni-ratio above 0.8. Thus, high Ni content facilitates cracking in the particles and leads to the formation of many pores for electrolyte penetration.

Consequently, all Ni-rich NCMs show increasing resistances as the function of cycling number in impedance measurements. The surface of exposed cracks is inactive rock-salt phase (Figure 14d), thus resulting in the slack kinetics. Compounds with higher Ni-content demonstrate higher overall resistances and higher rate of charge transfer resistance increase during cycling.

The formation of intergranular cracks is also more prone to occur under inhomogeneous delithiation. Several studies have recently shown that lithium concentration in the primary particle is spatially inhomogeneous during cycling, especially at high C-rate conditions.[58–60] The lithium-content inhomogeneity inside the particle leads to the coexistence of H2 and H3 phases, causing nonuniform stress and inducing lattice parameter changes and structural defects. In addition, a higher degree of delithiation can also give rise to accelerated cracks formation. When the material is highly delithiated, the H2–H3 phase transition occurs accompanied by severe lattice collapse along the c-direction, ultimately leading to unit volume shrinkage, as shown in Figure 14e.[56] Consequently, cracks gradually propagate within the secondary particles, resulting in mechanical failure, local resistance increases, and capacity fading.

3.1.7. Thermal Stability

Thermal stability is an important factor for the commercialization of Ni-rich cathode-based batteries. During battery operation, considerable heat will be generated in the system, initiating the risk of thermal runaway or even explosion under extreme circumstances.[61] Numerous studies have proven that thermodynamic instability can develop at higher temperatures, also under storage conditions without cycling.[62] As shown in **Figure 15**a, a capacity decay upon storage is strongly temperature-dependent. In postmortem analysis, it is noted that storage at high temperatures leads to a loss of electric contact between the electrodes and current collectors. It is concluded that high-temperature storage could give rise to more considerable capacity losses, escalated resistance, and even adhesive problems in pristine uncycled batteries.

The thermal instability of the Ni-rich cathode has also been attributed to the lower strength of M—O bonds in the delithiated state. Figure 15b shows the oxygen binding energy as a function of Li-content in various NCMs, indicating the strength of M—O bonds.[20] It can be seen that the oxygen binding energy decreases with increasing Ni-content in NCMs and Li-deintercalation. Thus, oxygen is released under a highly delithiation state, leading to an exothermic reaction of Ni ions, reduced from a higher valence state. Recently, Yoon and co-workers proposed that the thermal expansion and oxygen vacancies are two new factors affecting the thermal stability of Ni-rich cathodes.[65] X-ray absorption near edge structure (XANES) analysis of charged Ni-rich NCMs reveals that the most dramatic reduction of Ni^{4+} occurs in the materials at high temperatures. The reduction of Ni ions is accompanied by the formation of oxygen vacancies. Additionally, charged Ni-rich cathodes undergo a sizeable thermal expansion due to the lattice change. Both factors provide energetically favorable pathways for cation migration, accelerate thermal decomposition reactions, and finally lead to the thermal instability of Ni-rich cathodes.
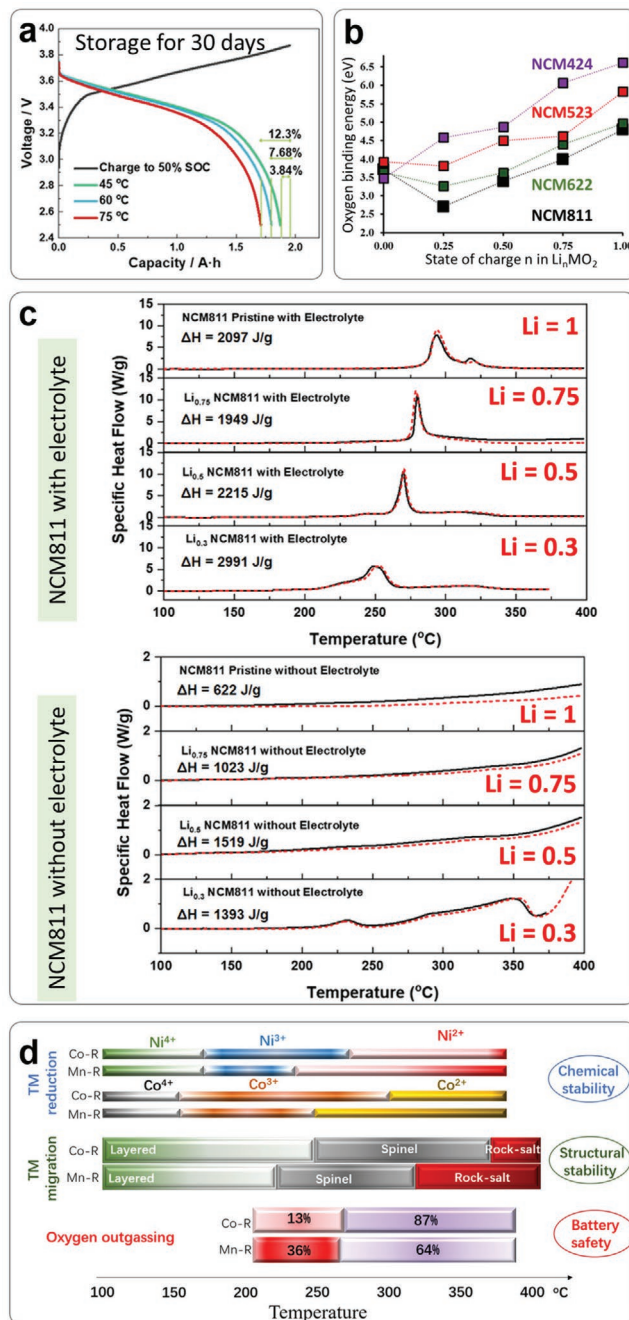
Figure 15. a) Charge (before storage) and discharge (after storage for 30 days) voltage curves of 21700-type batteries at different temperatures. b) Molecular oxygen binding energies for different NCMs as a function of SOC. c) Specific heat flow of an NMC811 electrode with and without the presence of an electrolyte. d) Illustration of chemical and structural stability during thermal degradation of a deep delithiated Ni-rich cathode. a) Reproduced with permission.[62] Copyright 2021, American Chemical Society. b) Reproduced with permission.[20] Copyright 2017, American Chemical Society. c) Reproduced with permission.[63] Copyright 2020, American Chemical Society. d) Reproduced with permission.[64] Copyright 2020, American Chemical Society.

The reactions between the active electrode material and electrolyte have also been investigated. The degree of

**ADVANCED
SCIENCE NEWS**
www.advancedsciencenews.com

**ADVANCED
ENERGY
MATERIALS**
www.advenergymat.de

heat-releasing of the electrode depends on the enthalpy of formation (ΔH). Figure 15c shows the heat generation of NCM811 cathodes filled with and without electrolytes at various delithiation states.[63] Strong delithiation at low Li-content results in a shift of the onset exothermic peak toward lower temperatures. In comparison, the samples without electrolyte contact show only minor heat evolution in all cases. Additionally, the gas releasing process is also facilitated by the higher delithiation states of the NCM811 cathode in the electrolyte. This observation indicates that a high SOC in the presence of the electrolyte makes Ni-rich materials more susceptible to thermal shock and produce more heat and gas during battery operation. This fact represents a serious safety hazard to LIBs.

Mn has been widely considered as a stabilizer for the NMC structure.[12] However, Amine and co-workers recently demonstrated that the thermal stability of deeply delithiated Ni-rich NCMs might be dominated by Co.[64] Based on their results, the presence of unstable Ni^{2+} and the onset point of phase transition in Mn-rich cathode occurs at a lower temperature compared with those of Co-rich cathode materials. Moreover, as illustrated in Figure 15d, Co-rich (Co-R) and Mn-rich (Mn-R) NCMs possess similar onset temperatures of two oxygen outgassing periods (red bar: first period; purple bar: second period), while Mn-R cathode outgasses 36% of its total oxygen in the first period, compared to the lower proportion for the Co-R cathode (13%). The earlier gas release brings a greater risk of thermal runaway, as the formed oxygen is highly reactive with electrolyte and lithiated anode. Thus, the Co/Mn concentration in Ni-rich cathodes has a considerable impact on battery safety. Extensive investigation of Ni-rich batteries with enhanced thermal stability is therefore of the highest priority.

3.2. Anode

3.2.1. Graphite Anode

Graphite is an intercalation anode material widely applied in almost all commercial LIBs over the last two decades due to high specific capacity with a theoretical limit of 372 mAh g^{-1}, low costs, and low working potential between 50 to 250 mV versus Li^+/Li.[8] The degradation of graphite anodes primarily results from three major causes. 1) Irreversible volume expansion and crack formation during cycling. Studies show the graphite-based cells can expand by 2–5% over their lifetime.[61] 2) SEI formation induced by electrolyte decomposition and reduction of transition metal cations dissolved from the cathode. 3) Li plating and dendrite growth.[66–68]

Figure 16a shows that cracks in polycrystalline graphite originate from the stress along the grain boundaries during the Li-ion intercalation and deintercalation.[69] Consequently, the propagated cracks result in an irreversible volume expansion of the graphite anode. Another study concluded that the total volume change of graphite unit cells could increase by 13.2% at the complete lithiation state (Figure 16b).[70] The relationship between the unit cell volume change and lithium stoichiometric number shows two distinctive stages: the volume is increased by 6.1% at stage 1 ($0 \leq x$ (Li) ≤ 0.50) and by 13.2% at stage 2 ($0.50 \leq x$ (Li) ≤ 0.95). Notably, the volume change remains almost
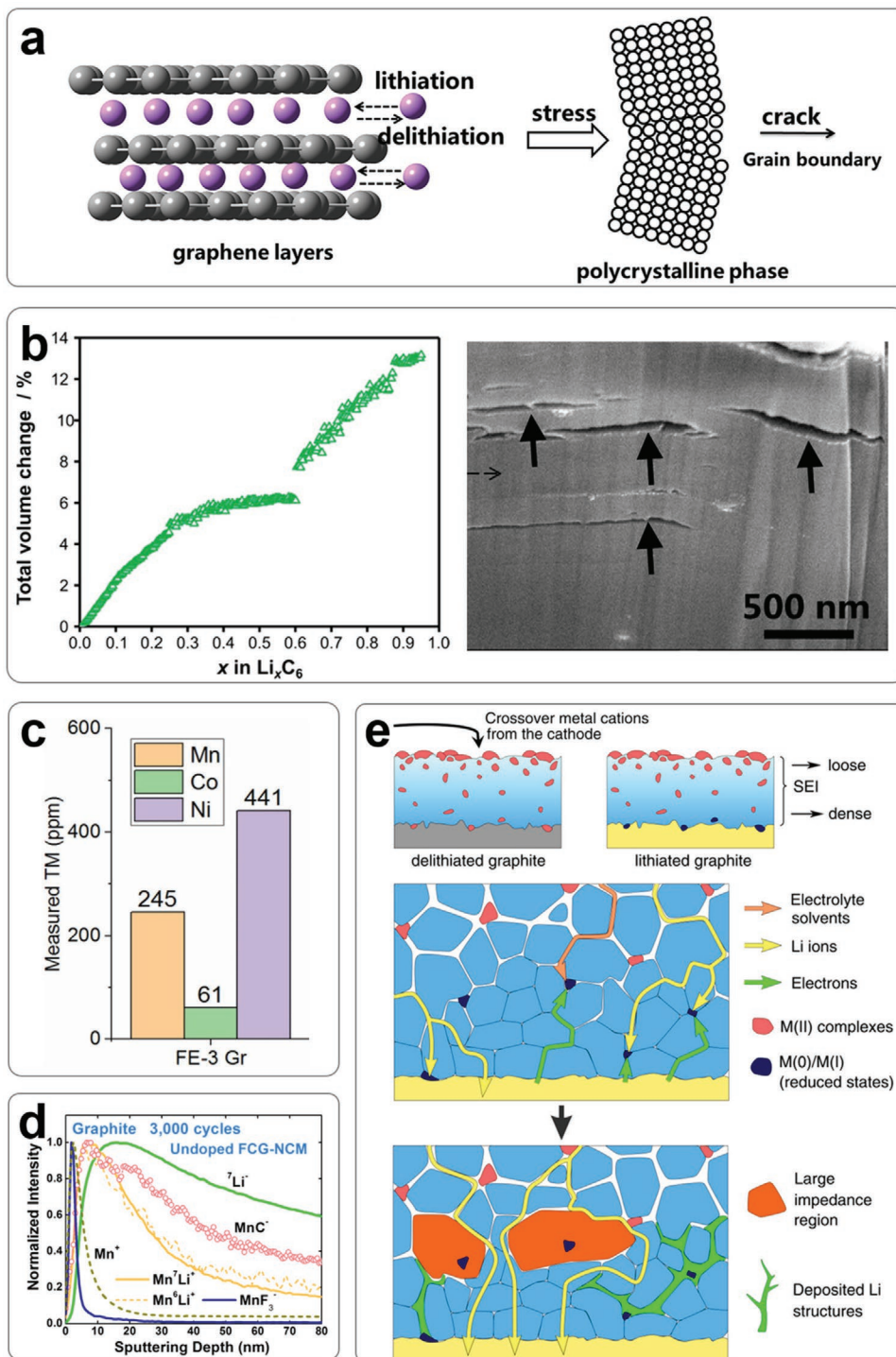
constant within the $0.25 \leq x$ (Li) ≤ 0.50 region. This behavior is attributed to the dominant intercalation mechanism, as Li accumulates in interlayers instead of occupying newly formed interlayers in the unit cell. These results demonstrate that occupation of only half of the intercalation sites can already lead to a significant crystallographic expansion of graphite. Figure 16b also shows an SEM image of cycled graphite, clearly revealing the formation of the parallel cracks inside the particles.[69]

Dissolution of Ni from the surface of Ni-rich cathode with subsequent precipitation on the anode side creates unfavorable chemical crossover, causing intensive SEI formation and nonuniform Li insertion, leading to a decline in battery performance. Inductively coupled plasma mass spectroscopy (ICP-MS) analysis for cycled graphite in Figure 16c reveals a considerable amount of transition metal deposited at the anode, especially Ni and Mn, attributed to the transition metal ions dissolved from the Ni-rich cathode during cycling.[71] Additionally, time-of-flight secondary ion mass spectrometry (TOF-SIMS) depth profiles of the cycled graphite confirm the migration of transition metal ions.[72] As shown in Figure 16d, a substantial amount of Mn ions (denoted by MnC^-, Mn^7Li^+, Mn^6Li^+, and MnF_3^-) penetrates inside the SEI film. The deposited transition metal components and the electrolyte decomposition products are believed to mask significant portions of graphite. That can increase the local current density and accelerate Li deposition and SEI growth. An overview of the parasitic reactions occurring and the formation of the SEI layer at the graphite surface can be seen in Figure 16e.[72] The crossover of metal cations from the cathode through the outer loose SEI layer at the graphite electrode is suppressed by the inner SEI layer at the graphite surface. The reduced transition metal ions subsequently serve as transport sites for electrons, facilitating electron transfer. When the SEI film grows, electrolyte decomposition and transition metal reduction lead to an accumulation of high-impedance regions, hindering Li^+ ions transportation. Simultaneously, the metallic Li will deposit at the graphite surface. Furthermore, the deposited Li structures will continuously develop into mosses and dendrite morphologies under extreme conditions, such as intensively cycling, rapid charging, high/low-temperature operation, etc.[73] Hence, immobilized Li due to SEI formation and Li deposition will consume active Li^+ ions from the battery system and accounts, in this way, for severe battery degradation.

Crossover effects in LIBs can also be induced by gas. Cui and co-workers reported that LiH induced exothermic reactions at the anode and that H_2 gas migration to the cathode are the primary triggers for thermal runaway of $LiNi_{0.5}Co_{0.2}Mn_{0.3}O_2$/graphite pouch cells.[74] Phase formations at the anode and O_2 release from the cathode have been considered the only accelerating factors.

3.2.2. Li-Metal Anode
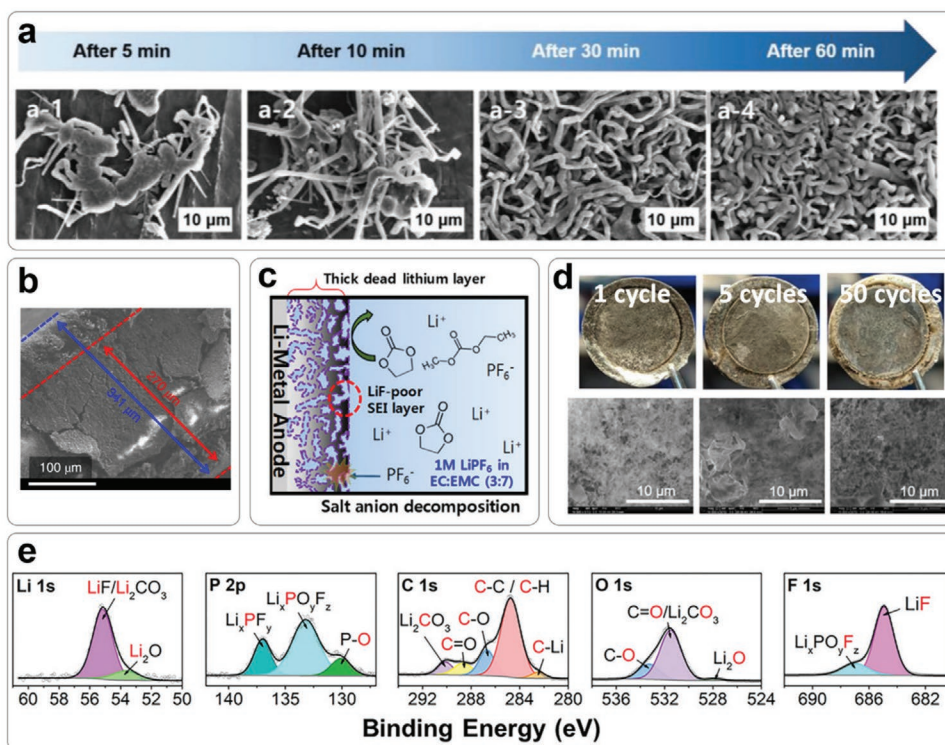
Studies focusing on Li-metal anodes have become more frequent in recent years. Li-metal has a remarkably high specific capacity (3860 mAh g^{-1}), the lowest redox potential (0 V vs Li^+/Li), and low density (0.59 g cm^{-3}).[75] With these promising parameters, Li-metal anode has become essential for the

ADVANCED
SCIENCE NEWS
www.advancedsciencenews.com

ADVANCED
ENERGY
MATERIALS
www.advenergymat.de

Figure 16. a) Crack formation of graphite particles induced by cycling. b) Volume change of a graphite electrode as a function of lithium content during lithiation, and SEM image of cracks. c) TM content obtained in a graphite anode after 120 cycles. d) TOF-SIMS depth profiles of graphite anode after 3000 cycles. e) Schematic representation of SEI film evolution at a graphite electrode during cycling under the influence of chemical crossover from the cathode. a) Reproduced with permission.[69] Copyright 2017, Elsevier. b) Reproduced with permission.[70] Copyright 2018, American Chemical Society. c) Reproduced with permission.[71] Copyright 2018, The Electrochemical Society. d,e) Reproduced with permission.[72] Copyright 2017, American Chemical Society.

next-generation LIBs in the market. Coupled with a Ni-rich cathode, pouch cells will be capable of meeting the goal with a high energy density of up to 890 Wh L^{-1}.[76] However, Li-metal

batteries face several critical challenges due to unstable dendrite growth and large volume expansion.[77–79] These shortcomings pose a significant risk of internal short-circuits in LIBs,

**ADVANCED
SCIENCE NEWS**

www.advancedsciencenews.com

**ADVANCED
ENERGY
MATERIALS**

www.advenergymat.de

Figure 17. a) SEM images of deposited Li on a Li-metal anode as a function of indicated deposit time. b) SEM image of cycled Li-metal anode in 1 M LiPF$_6$ in a DMC/FEC (8:2) electrolyte. c) Illustration of Li-metal anode degradation. d) Optical and SEM images of cycled Li-metal anodes. e) XPS spectra of a Li-metal anode after 50 cycles. a) Reproduced with permission.[81] Copyright 2020, Wiley-VCH. b) Reproduced with permission.[76] Copyright 2018, Nature. c) Reproduced with permission.[82] Copyright 2018, American Chemical Society. d,e) Reproduced with permission.[83] Copyright 2021, Wiley-VCH.

resulting in big safety concerns, restraining the commercialization of Li-metal anodes.[80]

The electrodeposition of lithium on a Li-metal anode is a hazardous and rapid process. It has been confirmed that Li deposition is not homogeneous. Li will be deposited at primary nucleation sites into a Li-moss structure or needle-like microstructures. **Figure 17**a demonstrates the structural evolution of Li plating as the function of time at the current density of 1.8 mA cm^{-2}.[81] It can be observed that Li is randomly deposited at the electrode surface already at the early stages (after 5 min) of charging and continuously aggregates into a porous morphology with a loose structure. The high surface area of deposited Li is attributed to the enhanced electrolyte consumption and the accumulation of Li dendrite growth. After long-term cycling in the electrolyte (1 M LiPF$_6$ in EC/DMC), the thickness of the Li-metal electrode expanded dramatically. It increased from 250 μm for the pristine electrode up to 341 μm for the cycled electrode, as shown in the cross-section SEM image of Figure 17b.[76] The red arrow reflects the highly porous and fragile Li layer, which shows poor resistance toward chemical degradation and suffers from side reactions between the electrolyte and Li-metal. Li dendrite growth and volume expansion of the Li-metal anode are illustrated in Figure 17c.[82] The thick death lithium layer is formed during combined electrolyte decomposition and Li plating/stripping cycling, which explains the low Coulombic efficiency generally found for Li-metal anodes.

The crossover effect in batteries with a Ni-rich cathode and Li-metal anode (LiNi$_{0.9}$Mn$_{0.05}$Co$_{0.05}$O$_2$/Li) has been thoroughly investigated by Langdon and Manthiram.[83] Figure 17d shows optical and SEM images of cycled Li-metal anodes from disassembled cells. Gradually dark and rough surfaces with spatial inhomogeneities can clearly be observed with increasing cycle number, suggesting the formation of a brittle SEI film at the Li-metal anode. Further characterization of a cycled Li anode was performed by XPS to analyze the composition of the SEI layer, as shown in Figure 17e. The peaks can be assigned to the electrolyte decomposition products, including LiF, Li$_x$PF$_y$, Li$_x$PO$_y$F$_z$, Li$_2$O, ROCO$_2$Li, etc. In addition, the authors compared the cathode-electrolyte-interphase (CEI) formation in an NCM/Li cell with that in an NCM/graphite cell. They found that the decomposition products from anodes can be transported to the cathode side and eventually accelerate CEI formation and impedance growth at the cathode side also. Appropriate modifications should be applied to metallic Li-anodes to avoid the adverse effect of such a process on battery performance.
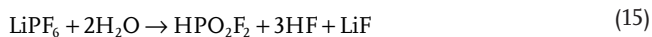
3.3. Electrolyte

3.3.1. Decomposition

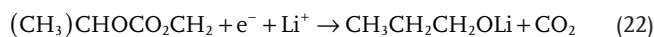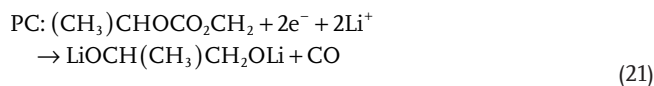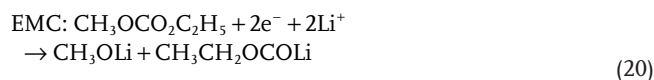The electrolyte serves as an ionic bridge between the cathode and anode of batteries. The role of electrolytes in the
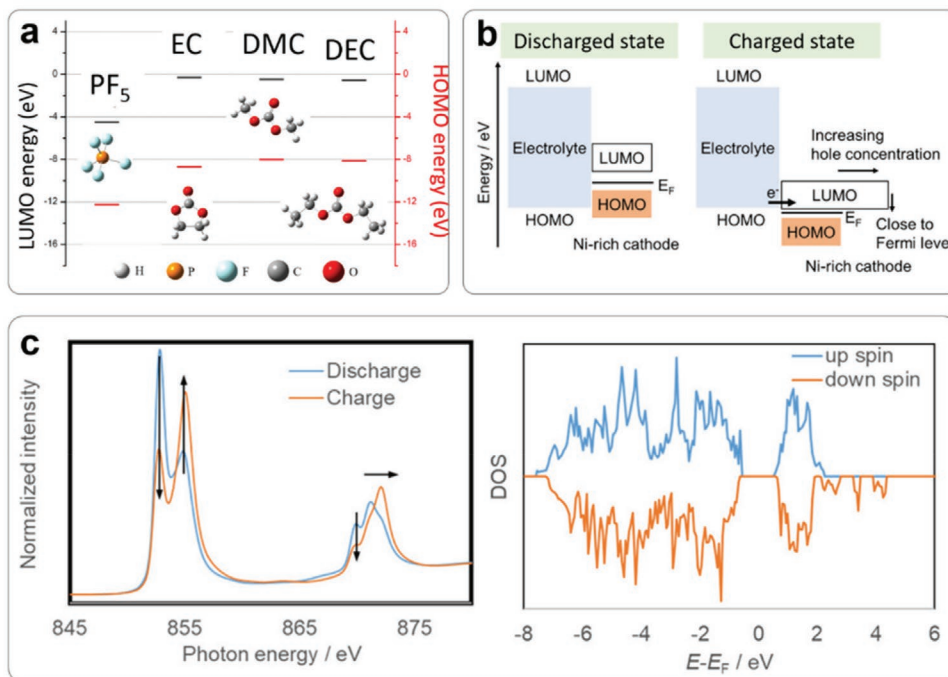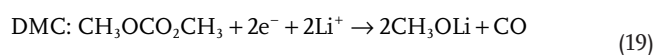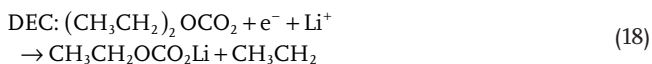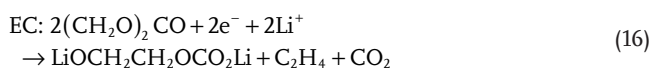
Figure 18. a) DFT calculations of electrolyte components. b) LUMO and HOMO energy levels of a Ni-rich cathode and electrolyte. c) S-XAS spectra of Ni L-edge of a Ni-rich cathode and corresponding DOS at the fully charged (delithiated) state. a) Reproduced with permission.[84] Copyright 2018, American Chemical Society. b,c) Reproduced with permission.[90] Copyright 2020, American Chemical Society.

performance and safety of LIBs is therefore immense. The electrolyte always consists of lithium salts and organic solvent(s). Both components are subject to side reactions. **Figure 18**a shows DFT molecular orbital calculations for PF_5 in solvents EC, DMC, and DEC, which are the most conventional electrolyte components and have been widely used in the battery industry.[84] PF_5 is the result of $LiPF_6$ decomposition. Owing to the relatively low LUMO energy, PF_5 is prone to gain electrons from other species in the electrolyte and initiate side reactions. The corresponding decomposition process of $LiPF_6$ has been described as follows[85]

$$LiPF_6 \rightarrow LiF + PF_5 \tag{13}$$

$$PF_5 + H_2O \rightarrow POF_3 + 2HF \tag{14}$$

$$LiPF_6 + 2H_2O \rightarrow HPO_2F_2 + 3HF + LiF \tag{15}$$

The decomposition process of solvents has been described by[86–89]

$$EC: 2(CH_2O)_2CO + 2e^- + 2Li^+ \\ \rightarrow LiOCH_2CH_2OCO_2Li + C_2H_4 + CO_2 \tag{16}$$

$$(CH_2O)_2CO + 2e^- + 2Li^+ \rightarrow Li_2CO_3 + C_2H_4 \tag{17}$$

$$DEC: (CH_3CH_2)_2OCO_2 + e^- + Li^+ \\ \rightarrow CH_3CH_2OCO_2Li + CH_3CH_2 \tag{18}$$

$$DMC: CH_3OCO_2CH_3 + 2e^- + 2Li^+ \rightarrow 2CH_3OLi + CO \tag{19}$$

$$EMC: CH_3OCO_2C_2H_5 + 2e^- + 2Li^+ \\ \rightarrow CH_3OLi + CH_3CH_2OCOLi \tag{20}$$

$$PC: (CH_3)CHOCO_2CH_2 + 2e^- + 2Li^+ \\ \rightarrow LiOCH(CH_3)CH_2OLi + CO \tag{21}$$

$$(CH_3)CHOCO_2CH_2 + e^- + Li^+ \rightarrow CH_3CH_2CH_2OLi + CO_2 \tag{22}$$

The degradation of other electrolytes has also been intensively investigated, and various reaction pathways were proposed.[89,91] The electrolyte decomposition has serious adverse effects on the battery performance, such as gas releasing and the consumption of Li^+ ions, leading to the loss of lithium inventory. Moreover, the decomposed products usually form passive layers at the electrode surface.

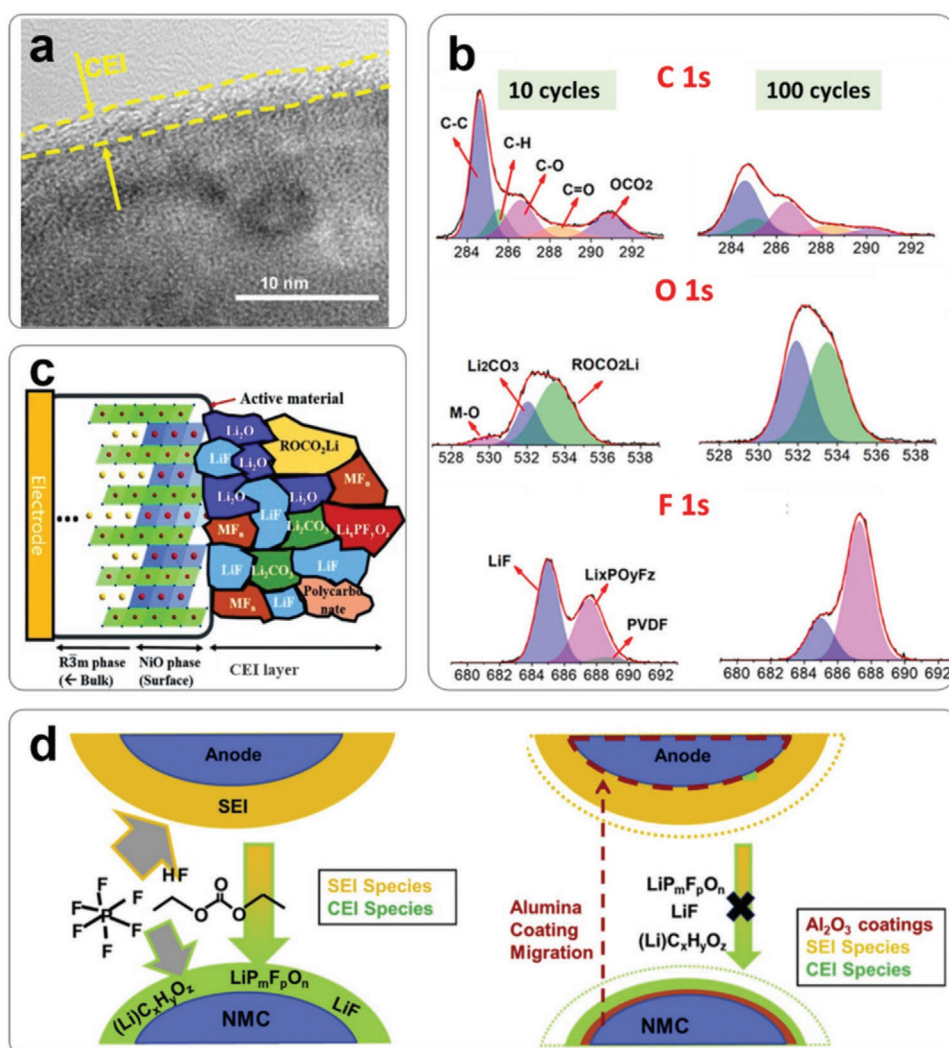### 3.3.2. CEI Formation

The electrolyte decomposition and CEI formation at the cathode are universal for all LIBs.[92–94] Compared to other active materials, TM ions in Ni-rich cathodes have a lower LUMO energy level, accelerating electrolyte oxidation. During cycling, the CEI film is continuously growing through the reactions between the cathode and electrolyte. This process predominantly occurs

**ADVANCED
SCIENCE NEWS**

www.advancedsciencenews.com

**ADVANCED
ENERGY
MATERIALS**

www.advenergymat.de

during charging, particularly for the reduction of Ni^{4+}, which attributes to the very low LUMO energy level of the antibonding orbital of e_g of Ni^{4+}–O 2p in Ni-rich materials.[90] According to previous DFT studies illustrated in Figure 18b, the Fermi level of NCM811 cathode materials approaches HOMO energy level of the electrolyte during charging. Thus, the hole concentration in the charged state increases dramatically, giving rise to electrolyte decomposition. In Figure 18c, the significant evolution of spectra can be detected in the Ni L-edge spectra measured in the charged and discharged states, suggesting a shift from Ni^{2+}–Ni^{3+} mixed-state to Ni^{4+}(peak located at 871.5 eV shifted to higher energy and intensity increased). The charged Ni^{4+} state has been confirmed to be highly nucleophilic to oxygen, which induces electrolyte oxidation. Additionally, DOS calculations of a discharged cathode show that an energy gap can be observed between the well-defined HOMO ($E - E_F < 0$ eV) and LUMO ($E - E_F > 0$ eV) energy levels. A high hole-concentration (at $E - E_F = 0$ eV) is obtained for a fully charged NCM811 ($Li_0Ni_{0.8}Co_{0.1}Mn_{0.1}O_2$)

electrode. That will induce electron transport from electrolyte molecules to the cathode, leading to electrolyte oxidation.

Unlike SEI films on the anode surface, CEI films are extremely thin, making it difficult to make direct observations. A TEM image of a Ni-rich cathode surface after 10 cycles shows a CEI film thickness of ≈3 nm (**Figure 19**a).[95] The CEI film continuously grows during cycling and stabilizes at around 5 nm. The components of the CEI films have been investigated XPS, as shown in Figure 19b.[84] It has been concluded that the CEI film is composed of inorganic components, including metal fluorides (LiF, NiF, etc.), metal oxides (Li_2O, Li_2CO_3, etc.), and organic components such as $ROCO_2Li$ and $Li_xPO_yF_z$. The inorganic components closely attach to the electrode surface and are considered as the "inner layer" of the CEI film, while the organic species are located at a larger distance from the electrode surface, defined as the outer CEI layer (Figure 19c).[1,97] Both layers have relatively poor lithium-ion conductivities, resulting in increased local resistances and performance decay.

Figure 19. a) SEM image of a CEI film on a cycled NCM811 electrode. b) XPS spectra of NCM622 after 10 cycles and 100 cycles. c) Illustration of CEI film formation on Ni-rich cathode surface. d) Illustration of CEI formation via migration of SEI components. a) Reproduced with permission.[95] Copyright 2020, Elsevier. b) Reproduced with permission.[84] Copyright 2018, American Chemical Society. c) Reproduced with permission.[1] Copyright 2015, Wiley-VCH. d) Reproduced with permission.[96] Copyright 2018, Elsevier.

Moreover, a chemical crossover between cathode and anode has also been reported in the literature. Hamers and co-workers investigated the ionic migration in $LiNi_{0.5}Co_{0.2}Mn_{0.3}O_2$/graphite, $LiNi_{0.5}Co_{0.2}Mn_{0.3}O_2$/Li, and $LiNi_{0.5}Co_{0.2}Mn_{0.3}O_2$/$Li_4Ti_5O_{12}$ cells by quantitative XPS analysis.[96] Their results show that the products of anodic decomposition can be detected in the CEI film at the cathode (Figure 19d). Subsequently, the migrated anodic species are reduced by the Al_2O_3 coating, protecting the cathode surface.

3.3.3. Challenges in ASSBs

With the growing concerns of safety aspects in LIBs, extensive research efforts have focused on exploiting all-solid-state batteries (ASSBs).[98] In this regard, ASSBs present a safer alternative to the conventional LIBs, especially for the electrodes and electrolytes with unstable properties, such as Ni-rich cathodes. Ni-rich cathode materials have recently been applied in several studies, and corresponding degradation mechanisms that exist specifically within all-solid-state battery systems have been investigated.[99–101] Apart from some intrinsic degradation mechanisms discussed in the previous sections, undermined mechanical integrity induced by cell pellet preparation and interfacial side reactions are other severe challenges in Ni-rich cathode-based ASSBs.[102] During the cell pellet preparation process, extensive pressure must be imposed on the particles, leading to contact failures at the solid-electrolyte interface even before cycling. As shown in **Figure 20**a, due to the cycling process, microcracks generated in secondary particles will be accelerated by the anisotropic volume expansion and contraction, resulting in mechanical failure. Figure 20b shows cross-section SEM images of particles after pellet pressing (upper image) and after cycling (lower image). Some internal microcracks can be observed in the particles after pressing. In contrast, after cycling, the particle completely lost its structural integrity due to pulverization.

The side reactions at the interface of Ni-rich cathodes and solid-electrolytes have also been responsible for capacity fading.[103] Figure 20c shows SEM images of pristine and long-term cycled $NCM622/\beta\text{-}Li_3PS_4$ composite electrodes. It can be seen that the cathode particles are distinct from the $\beta\text{-}Li_3PS_4$ solid-state electrolyte powder in the pristine state. After cycling, a significant solid-electrolyte decomposition layer can be observed, implying intense side reactions between the cathode and the solid-state electrolyte. Additionally, in a study of Ni-rich $LiNi_{0.80}Co_{0.16}Al_{0.04}O_2$ (NCA80) cathode and Li_6PS_5Cl solid electrolyte, XPS spectra reveal the existence of Li_6PS_5Cl-derived oxidized species at the cathode surface, as shown in Figure 20d.[104] As a result, interfacial side reactions reduce the lithium inventory in ASSBs and undermine the long-term cycling stability of ASSBs. Owing to the slack kinetics of ASSBs, the introduction
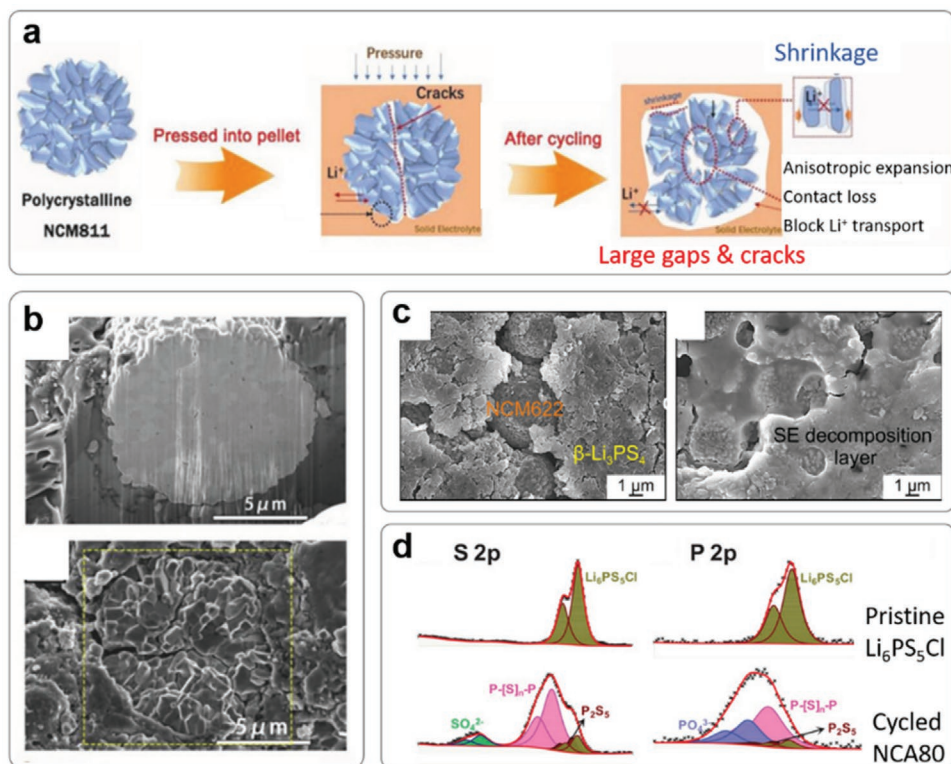
Figure 20. a) Schematic representation of crack formation induced by pellet preparation and cycling in an NCM811-based ASSB. b) SEM images of NCM811 particles before and after cycling in ASSB. c) SEM image of the interface between the NCM622 cathode and $\beta\text{-}Li_3PS_4$ solid-state electrolyte in the pristine and cycled state. d) XPS spectra of pristine Li_6PS_5Cl solid-state electrolyte and cycled NCA80 cathode. a,b) Reproduced with permission.[102] Copyright 2021, Wiley-VCH. c) Reproduced with permission.[103] Copyright 2019, American Chemical Society. d) Reproduced with permission.[104] Copyright 2019, Wiley-VCH.

ADVANCED
SCIENCE NEWS
www.advancedsciencenews.com

ADVANCED
ENERGY
MATERIALS
www.advenergymat.de

of electrode materials with enhanced capacity is highly needed. With the growing attention drawn to Ni-rich cathodes, the degradation mechanism of Ni-rich cathode-based ASSBs is thus essentially crucial for future broadening the range of the development for LIBs with improved safety.

4. Improvement Strategies

Numerous efforts have been devoted to the performance improvement for Ni-rich cathode-base LIBs.[105,106] The current strategies primarily focus on modifying the cathode, anode, and electrolyte. For cathode materials, the proposed strategies can be divided into the following categories: 1) Applying novel synthesis methods to avoid side-effects induced by conventional coprecipitation methods; 2) fabricating single-crystallized primary particles in favor of mitigating inner stress during the (de)lithiation process; 3) tailoring highly ordered morphologies to inhibit microcracks propagation within the electrode particles; 4) introducing foreign ions (cations or anions) into the crystal lattice for structural stabilization of the host material; 5) coating protective layers onto the cathode surface to prevent HF attack from the electrolyte; and 6) synthesizing particles with elemental concentration gradient structure.

Concerning the anode modifications, structural changes and protective layer coatings are commonly employed for the graphite anode and Li-metal anode.[107–109] Such strategies facilitate the stable mechanical properties of anode materials. Electrolyte decomposition and chemical crossover from the cathode can also be suppressed efficiently for the anodes. To optimize the electrolytes, many additives with various functional groups have been studied to restrain the decompositions of lithium salts and organic solvents in the electrolyte.[45,110,111] Some up-to-date and representative approaches for improving cathode, anode, and electrolyte in Ni-rich cathode-based LIBs will be discussed below.

4.1. Cathode

4.1.1. Novel Synthesis Methods

Coprecipitation combined with a solid-state reaction is the most mature and conventional method to prepare Ni-rich cathode materials. According to literature, the exact ratio between reactants and calcination parameters is essential for the quality of the final products.[112] However, limited by the reaction conditions, such a procedure always results in intrinsic drawbacks, such as a considerable amount of RLCs at the powder surface, a high degree of cation disorder, and crystal defects inside the crystallographic structure. Appropriate water-washing or acid-washing processes can dramatically eliminate the side effects of RLCs.[30] However, to fight cation disorder and crystallographic defects, more advanced synthesis methods have to be applied.

The high degree of cation disorder is attributed to the partial enrichment of Ni^{2+} at the cathode surface, inherited from Ni^{2+} in the transition metal precursor during the coprecipitation process. One of the optimization procedures is based on the cathode pretreatment via oxygen plasma and oxidants. Xie

and co-workers reported an improvement in the cyclability of $LiN_{i0.8}Co_{0.15}Al_{0.05}O_2$ cathodes by a nondestructive plasma treatment, as demonstrated in **Figure 21**a.[113] High-energy, active groups (O, •OH, O^3, O^3•) are obtained in the oxygen plasma, leading to $Ni^{2+}{\rightarrow}Ni^{3+}$ oxidation at the cathode surface. The formation of a NiOOH (nickeloxyhydroxide) layer at the cathode surface has also been confirmed. As presented in reactions (9) and (10) in Section 3.1.3, the surface reconstruction layer is induced by lattice oxygen loss. Thus, peroxidation of the cathode surface could reduce the following phase transformation in the synthesis. Hence, enhanced cycling stability and rate capability of Ni-rich cathode can be achieved.

Another widely used surface-oxidation method based on wet chemistry is mixing oxidants, such as $Na_2S_2O_8$ and $KMnO_4$, with hydroxide precursor during synthesis.[114] A representative study was carried out by Chen and co-workers with $Na_2S_2O_8$ peroxidization method (Figure 21b). Similarly, an ordered NiOOH layer is obtained after treatment, which guarantees the elimination of Li/Ni mixing and crystal defects at the cathode surface, eventually improving the cycling performance.

Apart from surface-oxidation, introducing oxygen vacancies at the cathode surface during the synthesis process is also a novel approach to avoid structural failure during cycling. Oxygen vacancies can serve as electron donors in the crystal host material. Massive oxygen vacancies are expected to form high-density dislocation layers at the grain surface. Wu and co-workers created oxygen vacancies by treating samples in an N_2 atmosphere.[115] The obtained high-density dislocation layers originate from oxygen vacancies, preventing continuous propagation of intergranular cracks inside the particles during cycling. Figure 21c shows TEM analyses and crystal structures of untreated and treated cathodes after cycles. Restrained growth of the inactive rock-salt phase at the surface of the treated cathode can be clearly seen. In addition, approaches based on hydrothermal synthesis are also advantageous in forming Ni-rich cathode materials with enhanced structural stability and thus contributing to electrode performance improvement.[116,117] Unfortunately, most of the proposed synthesis methods are quite complex for mass production, limiting their practical applications in large-scale battery production.

4.1.2. Single-Crystal Fabrication

The morphology of conventional Ni-rich cathodes has been described as a spherical secondary particle agglomerated with polycrystalline primary particles. The randomly aggregated primary particles result in strong grain boundary stress due to the anisotropy of Li-ion intercalation and deintercalation. In turn, the increase of boundary stress will lead to the loss of electrical contact between primary particles and accelerated electrolyte attack. A direct strategy to reduce grain boundary stress is to fabricate single-crystal cathode particles.[118,119] Advanced mechanical strength and more homogeneous electrochemical reactions can be achieved due to the high crystallinity and isotropy orientation of single-crystal cathode materials.

One of the critical factors to produce single-crystal particles is the sintering temperature controlling the solid-state lithiation reactions. Wang and co-workers investigated the agglomeration
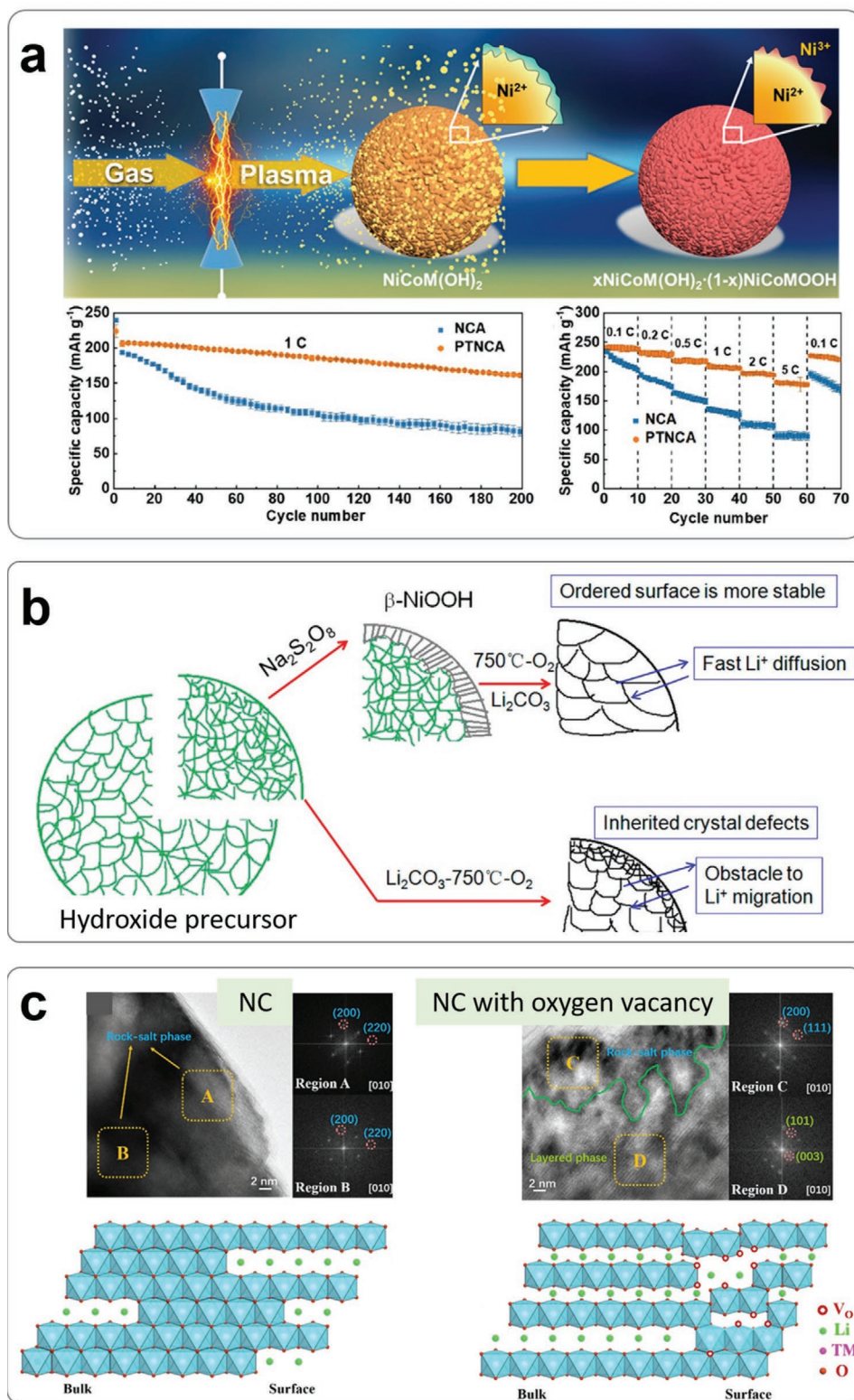
Figure 21. a) Schematic representation of the plasma treatment process of NCA precursor and comparison of the electrochemical performance of pristine and plasma-treated NCA cathode. b) Illustration of the reaction sequence of a $Na_2S_2O_8$-treated NCA precursor. c) HR-TEM images and structural model of $LiNi_{0.9}Co_{0.1}O_2$ (NC) and $LiNi_{0.9}Co_{0.1}O_2$ with oxygen vacancies (VO-NC-1) after cycling. a) Reproduced with permission.[113] Copyright 2020, Elsevier. b) Reproduced with permission.[114] Copyright 2016, American Chemical Society. c) Reproduced with permission.[115] Copyright 2020, American Chemical Society.

ADVANCED
SCIENCE NEWS
www.advancedsciencenews.com

ADVANCED
ENERGY
MATERIALS
www.advenergymat.de

degree of the final $LiNi_{0.8}Co_{0.15}Al_{0.05}O_2$ product with increasing sintering time, as shown in **Figure 22**a.[120] Combining in situ XRD and ex situ SEM measurements, the authors found that after 5 h sintering, single-crystal materials are formed with the most promising crystallinity. If the sintering time increases further, the grain size becomes much larger, suggesting a relatively high agglomeration. The diffraction spots in the selected area electron diffraction (SAED) image of a single-crystal particle are ideally aligned to the (104), (101), and (003) planes, confirming the well-defined hexagonal-layered crystal structure (Figure 22b). Compared with polycrystalline cathodes, single-crystal cathodes can adapt to volume changes, prevent intergranular microcracks, and shorten the Li-ion diffusion paths, ultimately improving the structural stability. However, the high dispersity of particles also facilitates the continuous growth of the surficial reconstruction layer (layered phase → rock-salt phase), bringing a major challenge for this method. A surficial reconstruction layer is detected on the long-term cycled single-crystal cathode (Figure 22c).

Sun and co-workers proposed a smart modification based on a single-crystal NCM811 cathode to cope with the above disadvantageous.[121] Single-crystal primary particles assemble into the secondary particles with radially aligned morphology, as illustrated in Figure 22d. Compatible lattice orientation exposing active crystal planes can provide open Li-ion diffusion channels from the surface to the center of these secondary particles. The compact aggregated primary particles with favorable crystal orientation can, on the one hand, mitigate intergranular stress by coordinated expansion/contraction. On the other hand, close contact between the primary particles prevents the growth of surface reconstruction layers. Only a minor surface reconstruction layer with 2–3 nm thickness can be observed at the cycled particles. Figure 22e shows that both the rate capability and cycle stability are remarkably promoted in the single-crystal NCM811 cathode materials with compatible crystal orientation and facilitated Li^+ diffusion.

It should be noted that although intergranular fractures can be avoided in single-crystal cathodes, the formation of intragranular fractures is still inevitable. That has also been considered as the primary degradation mechanism in single-crystal cathodes.[122] However, unlike the uncontrolled growth of intragranular fractures in polycrystalline particles, the fracture along the (003) direction in single-crystal particles remains stable once it appears during cycling.[123] The highly ordered orientation guarantees reversible planar gliding in the single-crystal lattice during cycling. Such self-limiting nature prevents continuous propagation of intragranular fracturing that eventually pulverizes the primary particles. The cycling performance is, therefore, significantly improved.

4.1.3. Microstructural Modification

Another strategy related to structural optimization of Ni-rich cathodes is microstructural modification. Cathodes with specially designed heterostructures or unique morphologies have remarkably improved structural stability with respect to long-term cycling. Heterostructure cathodes are typically composed of two structurally partitioned regions, including a compact inner-core region and a more open outer-shell region with completely different structures.[124]

As discussed in the previous section, conventional polycrystalline Ni-rich cathodes suffer from strong internal strain due to the anisotropic orientation. Thus, Ni-rich cathodes with a hierarchical structure could be a promising alternative. A pioneering work about heterostructured Ni-rich cathodes was reported by Sun and co-workers.[125] They presented a multicompositional NCM cathode material with polygonal shaped $LiNi_{0.94}Co_{0.038}Mn_{0.022}O_2$ in the particle core region, compactly surrounded by highly aligned $LiNi_{0.841}Co_{0.077}Mn_{0.082}O_2$ in the shell region. The outermost layer is smartly designed with a higher Ni-content to dissipate the internal strain induced by the H2-to-H3 phase transition during delithiation. The core- and shell-particles, therefore, undergo an unsynchronized lattice change due to the various Ni-contents.

As demonstrated in **Figure 23**a, the elongated primary particles in the outside layer are aligned along the *a*-direction and remain parallel to the radial direction, enabling the volume of the particles to change in the radial direction. As a result, the microscaled radial structure relieves the anisotropic strain. It constrains microcrack propagation, enabling highly improved electrochemical properties and structural stability. Subsequently, Sun's group explained why microstructurally engineered Ni-rich cathodes are so stable against the microcracks formation, as visualized in Figure 23b.[124] They investigated three different Ni-rich cathodes: bulk-structured $LiNi_{0.92}Co_{0.04}Mn_{0.03}Al_{0.01}O_2$ with higher Ni-content (BS-NCM92), bulk-structured $LiNi_{0.845}Co_{0.067}Mn_{0.078}Al_{0.01}O_2$ with lower Ni-content (BS-NCM85), and a hybrid-structured cathode (HS-NCMA90) with an interior BS-NCM92 core encapsulated by an exterior BS-NCM85 shell. In situ XRD measurements indicate the changes of the *c*-axis lattice parameters for the three cathodes during the H2-to-H3 phase transition during voltage variation. The degree of lattice contraction clearly depends on the Ni-content. Therefore, the core crystallites experienced compressive force while the shell-particles experienced tensile force during the delithiation process. This tensile stress in the outside layer clamps the wall of the microcracks and prevents it from propagation toward the particle surface.

Another way of producing heterostructured Ni-rich cathode materials has been reported by Wu and co-workers.[126] The obtained NCM811 particles are composed of compacted cores and nanosheet-stacked shells (Figure 23c). By properly controlling the synthesis process, the primary particles in the outer region dominantly expose active (010) crystallographic facets, creating favorable Li^+-ion transportation pathways. Furthermore, the highly ordered microstructure enables enhanced Li-ion diffusion, and exhibits excellent stability and rate capability.

Microstructural modification toward Ni-rich cathodes also includes studies on fabricating particles with other unique morphologies.[128] For example, Wang and co-workers presented a 3D flower-like hierarchical NCM622 cathode material by making use of a self-assembling synthesis process, as exemplified in Figure 23d.[127] TEM measurements confirm that the side-wall of the primary particle is the active (010) plane, contributing to the faster ionic transport kinetics.

The main target of this microstructural modification strategy is to form a cathode particle with a well-designed and controlled
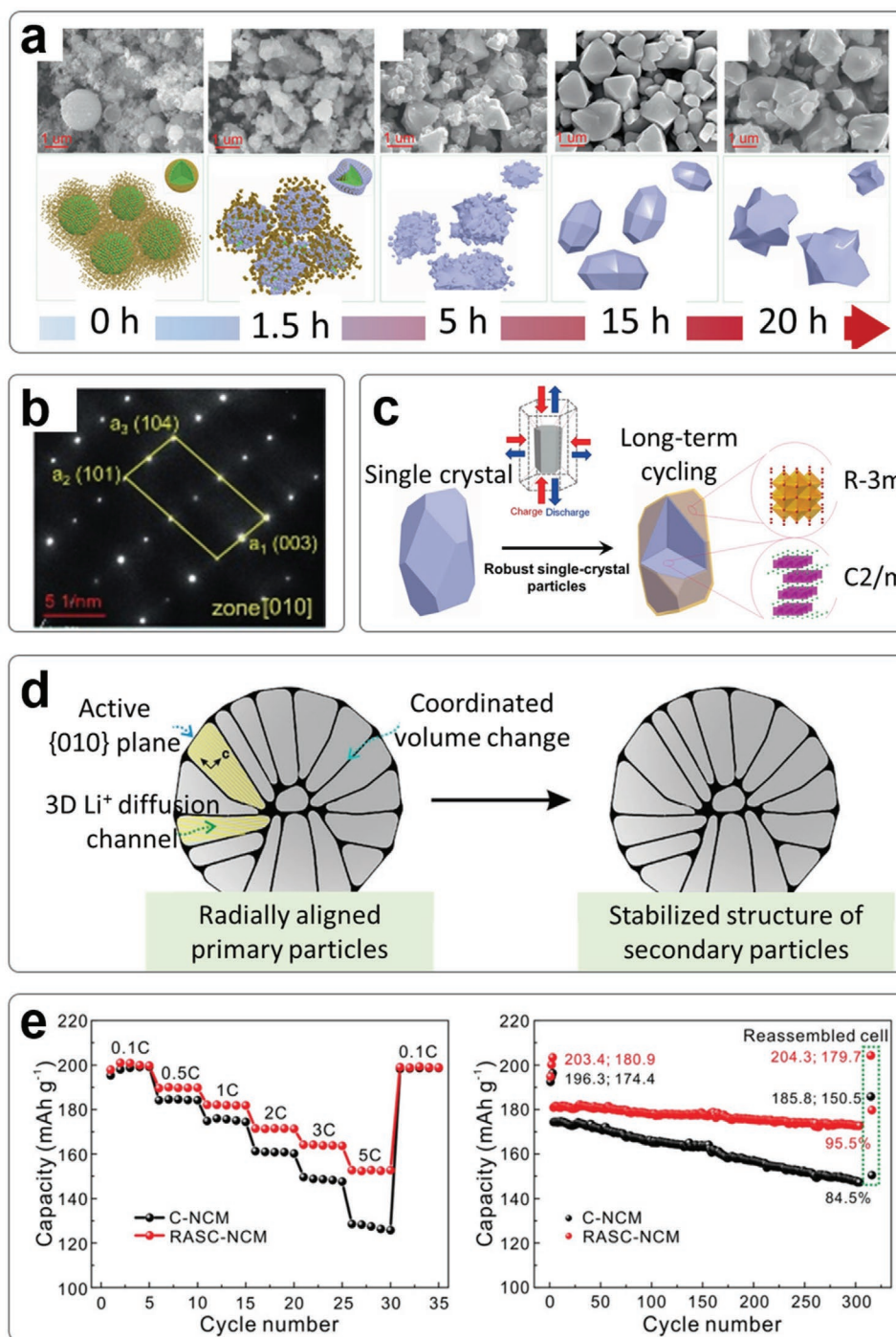
Figure 22. a) Phase and morphological evolution during the sintering process of the single-crystal synthesis process. b) SAED image of an as-prepared single-crystal NCA. c) Schematic illustration of phase transformation in a single-crystal NCA particle upon cycling. d) Schematic mechanism of the structural stability in a single-crystal NCM811 particle. e) Performance comparison between commercial poly-crystal NCM 811 (C-NCM) and radially aligned single-crystal NCM811 (RASC-NCM). a–c) Reproduced with permission.[120] Copyright 2021, Wiley-VCH. d,e) Reproduced with permission.[121] Copyright 2019, Wiley-VCH.

structure, which can be beneficial in suppressing the continuous growth of microcracks and, hence, achieving improved electrochemical electrode properties. However, similar to the strategy of single-crystalline materials, it is not possible to avoid intragranular fracturing caused by crystal lattice mismatches. Also, in some cases, the particles with novel morphology may lead to a higher degree of transition metal ion dissolution and lower tap density because of a higher specific surface area.[128]
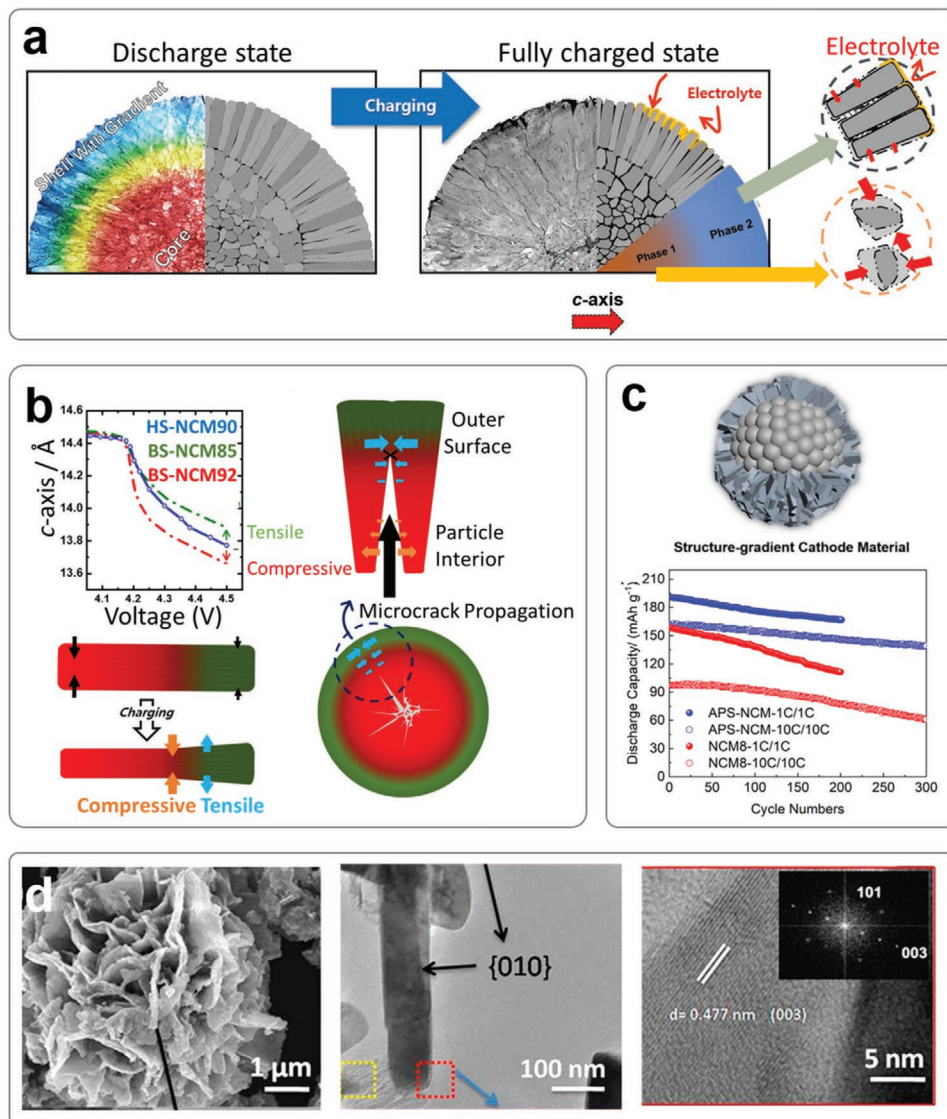
Figure 23. a) Schematic representation of the discharge and charge state of a structurally modified NCM core–shell particle. b) Evolution of lattice parameters during the H2-to-H3 phase transition in three different NCM cathode materials, illustrating the microcrack-resisting mechanism of HS-NCMA90. c) Layout and electrochemical performance of active-plane exposing shell NCM811 (APS-NCM). d) SEM and TEM images of NCM622 with hierarchical morphology. a) Reproduced with permission.[125] Copyright 2019, Wiley-VCH. b) Reproduced with permission.[124] Copyright 2020, American Chemical Society. c) Reproduced with permission.[126] Copyright 2019, American Chemical Society. d) Reproduced with permission.[127] Copyright 2018, American Chemical Society.

4.1.4. Doping

Incorporating various foreign ions into host materials is a well-known and frequently used method in material optimization. Elemental doping, including cation doping and anion doping, has been proven to significantly boost Ni-rich cathodes' structural and thermal stability.[106] Elemental doping can facilitate the performance of Ni-rich cathodes as it inhibits the irreversible phase transitions during delithiation, especially under high voltage operation conditions. The electrochemically inactive nature of dopants can explain this behavior in the cathode crystal lattice, which provides strong chemical bonds. Therefore, electrode degradation related to cation disorder, oxygen gas evolution, and intergranular cracking in Ni-rich cathode can be suppressed. Up to now, numerous substitutional elements have been proposed, such as Mg, Zr, Ce, Mo, Ta, etc., as cation dopant and F, Br, etc., as anion dopant.[129–135] **Table 2** summarizes the most important dopants for Ni-rich cathodes that have been published in the last three years.

Some cation dopants can act as "pillar ions" in the Ni-rich cathode crystal lattice to strengthen the bulk structure, as depicted in **Figure 24**a.[141] Preformed nanoscale cation disorder units are found in Ce^{4+}-doped NCM811 particles. Because of the stabilizing "pillar effect" and stronger Ce—O bonds, ion migration and NiO phase formation are effectively constrained in doped materials compared to undoped materials. Other

ADVANCED
SCIENCE NEWS

www.advancedsciencenews.com

ADVANCED
ENERGY
MATERIALS

www.advenergymat.de

Table 2. Summary of dopants in Ni-rich cathodes.

Dopant	Cathode	Function	Cut-off voltage (V vs Li+/Li)	Specific capacity[a] [mAh g−1]	Capacity retention	Refs.
Mo^{6+}	NCM811	Expand the interlayer spacing	2.75–4.3	215	92.4% after 100 cycles	[129]
Zr^{4+}	NCM811	Suppress layered-spinel phase transformation	2.8–4.3	180	84.3% after 60 cycles	[130]
Ti^{4+}	NC9[b]	Improve reversibility of the H2–H3 phase transitions	2.8–4.3	205	97.96% after 100 cycles	[131]
B^{3+}	NCM92[c]	Mitigate the particle cracks	2.5–4.4	221	78% after 100 cycles	[132]
P^{5+}	NCM92	Mitigate the particle cracks	2.5–4.4	221	72% after 100 cycles	[132]
Nb^{5+}	NCM811	Reduce the activity of Ni^{3+}; strong Nb—O bonds	3.0–4.3	210	97% after 100 cycles	[135]
Ga^{3+}	NCM811	Expand the interlayer spacing	2.8–4.3	203	91.2% after 100 cycles	[136]
Al^{3+}	NCM815[d]	Expand the interlayer spacing	2.8–4.35	208	98% after 100 cycles	[137]
Mg^{2+}	NCM83[e]	Mitigate the particle cracks	2.8–4.5	202	74% after 100 cycles	[138]
Ta^{5+}	NCM622	Strong Ta—O bonds; suppress cation disorder	3.0–4.5	197	83.6% after 100 cycles	[139]
F^-	NCM80[f]	Suppress cation disorder	2.7–4.3	217.7	96.5% after 100 cycles	[134]
Br^-	NCA815[g]	Expand the interlayer spacing	2.8–4.3	180	73.7% after 100 cycles	[140]

[a]Specific discharge capacity at 0.1C in the first cycle; [b]$LiNi_{0.9}Co_{0.1}O_2$; [c]$LiNi_{0.92}Co_{0.04}Mn_{0.04}O_2$; [d]$LiNi_{0.80}Co_{0.15}Mn_{0.05}O_2$; [e]$LiNi_{0.83}Co_{0.12}M_{n0.05}O_2$; [f]$LiNi_{0.80}Co_{0.05}Mn_{0.15}O_2$; [g]$LiNi_{0.815}Co_{0.15}Al_{0.035}O_2$.

cation dopants with higher valence states (Ti^{4+}, W^{6+}) also show similar functions by firmly clamping the active lattice oxygen and stabilizing the crystal structure.[131] It is noteworthy to remind that careful control of the doping ratio is critical for the cathode modification. Disproportionate dopant ratios cannot further improve the stability of the cathode. On the contrary, the capacity will be compromised because of blocking the active sites in the crystal lattice.

Conventional Ni-rich NCM and NCA materials originate from doping Co, Mn, and Al ions into the host lattice of $LiNiO_2$ to address structural instability. Another route for elemental doping is replacing the Mn and Al in Ni-rich NCMs and NCAs with other ions to form novel ternary cathodes. Sun and co-workers systematically studied five different substitutional cation dopants in $LiNi_{0.91}Co_{0.09}O_2$, including $LiNi_{0.90}Co_{0.05}Mn_{0.05}O_2$ (NCM90), $LiNi_{0.90}Co_{0.09}Al_{0.01}O_2$ (NCA90), $LiNi_{0.90}Co_{0.09}W_{0.01}O_2$ (NCW90), $LiNi_{0.895}Co_{0.09}B_{0.015}O_2$ (NCB90), and $LiNi_{0.90}Co_{0.09}Ta_{0.01}O_2$ (NCT90).[142] NCT90 exhibits the highest stability among the different doped materials with capacity retention higher than 95% and energy density larger than 850 Wh kg−1 after 100 cycles (Figure 24b). The substitution of Ta enables the cathode to form a highly ordered structure when lithiation takes place at 730 °C, demonstrating a decrease in inherent Li/Ni mixing compared with NCA90. Such cation ordering is also found in other cation doping cases. Furthermore, introducing foreign ions with larger ionic radii (Mo, Ta, Nb, etc.) increases the distance between the TM slabs, leading to the expansion of Li-ion diffusion channels and, consequently, improved electrochemical performance.

Anion doping is another kind of doping to stabilize the Ni-rich cathode structure by substituting O^{2-} with other anion dopants to form stronger chemical bonds with transition metal ions. Among various choices, F^- doping is frequently adopted in many studies. It has been considered that the binding energy of the TM–F bond is higher than that of TM–O, which is attributed to the more electronegative value of F^- than O^{2-}.[143] Most recently, Sun's group investigated the origin of the ultralong cycle life of F^--doped NCM cathode materials from an atomic point of view.[134] This study reveals F^--doped NCM materials will induce the formation of an ordered structure with $2a_{hex} \times 2a_{hex} \times c_{hex}$ superlattice. As shown in Figure 24c, Ni migration at the Li-sites occurs every two rows to form this superlattice structure. This ordered structure successfully survived 2000 cycles without revealing any lattice mismatches, which explains the long cycle life of the F^--doped $LiNi_{0.80}Co_{0.05}Mn_{0.15}O_2$. This is accompanied by a minor evolution of the impedance after 2000.

In general, the elemental doping strategy appeared to be the most efficient method to solve this issue by constraining the growth of intragranular cracks in Ni-rich cathode materials. The introduced foreign ions can strengthen the crystal structure by directly forming stronger bonds with host ions and preventing the continuous propagation of lattice mismatches. However, as mentioned above, the optimal doping ratio needs to be used to achieve enhanced stability without compromising any intrinsic capacity since most of the dopants that have been proposed are electrochemically inactive.

4.1.5. Protective Layer Coatings

Although structural modification methods can mitigate defect formation in Ni-rich cathode materials, the degradation induced by surface side reactions, such as HF corrosion and CEI formation, remains unsolved. In response to these challenges, protective layer coatings emerged as the most sensible strategy to impede electrolyte decomposition and suppress the dissolution of transition metal ions from the Ni-rich cathodes.[144] Various coating techniques have been proposed, involving wet chemical
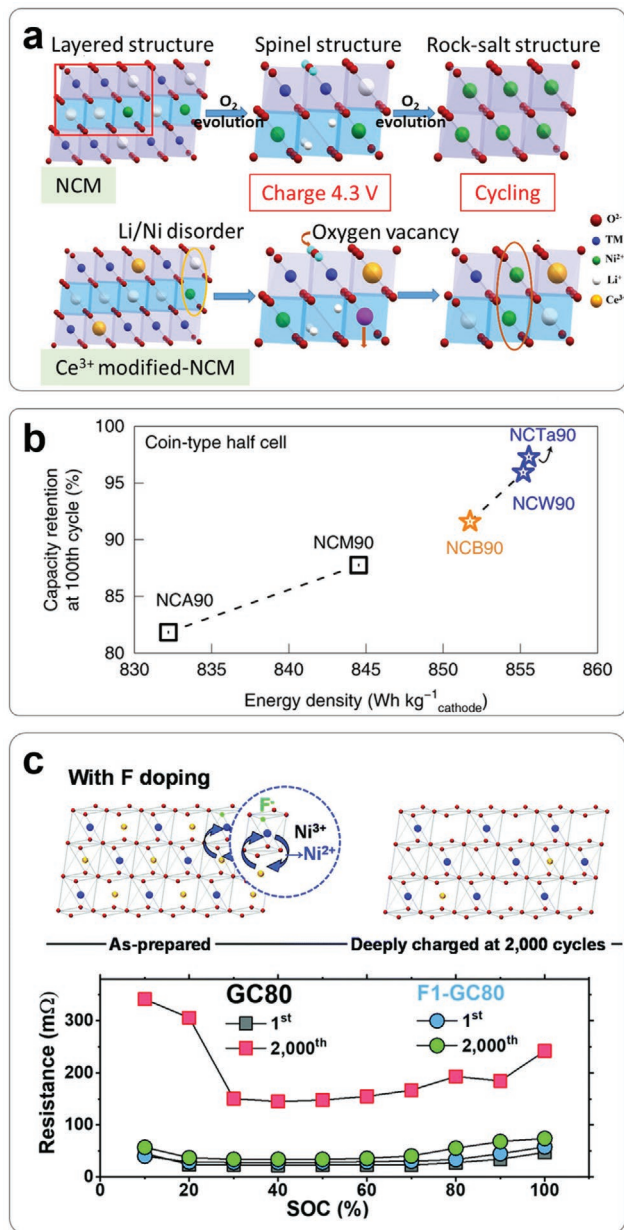
Figure 24. a) Schematic illustration of suppressing intergranular cracks on Ce^{4+}-doped NCM811 particles and the phase transition mechanism. b) Cathode-level energy density versus capacity retention for Ni-rich cathodes with different dopants. c) Illustration of structural stability of F^--doped NCM, and the evolution of resistance as a function of SOC after the 1st and 2000th cycles. a) Reproduced with permission.[141] Copyright 2021, American Chemical Society. b) Reproduced with permission.[142] Copyright 2018, Nature. c) Reproduced with permission.[134] Copyright 2021, Royal Society of Chemistry.

coating, dry ball-milling, sputtering coating, chemical vapor deposition (CVD) coating, and atomic layer deposition (ALD) coating.[145] Surface coating materials are also diverse and include metal oxides (Al_2O_3, TiO_2, MgO, etc.), metal fluorides (LiF, AlF_3, etc.), phosphates ($MnPO_4$, $AlPO_4$, $Si_3(PO_4)_4$, etc.), solid-state electrolytes (Li_3PO_4, $LiNbO_3$, Li_2ZrO_3, etc.), and conductive organic materials (polyimide, polyaniline, etc.).[146–153]

Coating layers can be divided into nonconductive materials (metal oxides, fluorides, and phosphates) with high stability and ionic conductive materials (solid-state electrolytes and conductive organic materials) with high Li-ion conductivity. As schematically shown in **Figure 25**a, Yim and co-workers fabricated a combined protective layer consisting of CaO and Li_3PO_4 at the NCM811 cathode surface via a dry coating technique.[154] CaO was employed as HF scavenging material, preventing corrosion between the acid and cathode. Thus, the dissolution of TM ions by HF can be suppressed. ICP analyses of cycled Li-metal in modified NCM811 cells show a significantly smaller amount of TM components than that in unmodified NCM811. On the other hand, Li_3PO_4 provides favorably Li-ion transport pathways due to its high ionic conductivity. The combination of CaO and Li_3PO_4 shows the ability to alleviate electrolyte decomposition at the cathode surface, assuring the long-term cycling performance of protective-layer-coated NCM811 cathodes.

Introducing negative thermal expansion (NTE) materials in electrodes is a novel design that emerged in recent studies. Such materials with extremely low expansion characteristics can be beneficial in stabilizing Ni-rich cathodes. Bai's group first applied a typical NTE material (ZrV_2O_7) to modify the surface of NCM622.[155] The cycling performance of the cathode was improved sharply. It can be cycled up to 500 cycles with a capacity retention of 71.0%. DOS calculations of surficial O 2p orbits explain why the ZrV_2O_7 layer stabilizes the surface. By the influence of Zr, the DOSs of oxygen decreases below −4 eV and become inert, which has been attributed to Zr ions tailoring the local electron distribution around surficial oxygen (Figure 25b). In contrast, for an unmodified surface, the energy at 1.5 eV suggests labile oxygen existing at the surface, which is prone to react with the electrolyte. In situ XRD measurements further reveal a change of the lattice volume expansion upon (de)lithiation for ZrV_2O_7-coated NCM622 is only half of that of pristine NCM622, as shown in Figure 25c. The mechanism of surface stabilization presented above can help to understand the functions of various electrochemically inert protective layers proposed in other studies.

Numerous organic materials have also been investigated to suppress electrolyte decomposition at the cathode electrode surface.[105] Park and co-workers developed an OTS-coated (octyltrichlorosilane) $LiNi_{0.82}Mn_{0.09}Co_{0.09}O_2$ (NCM82) cathode with higher storage cyclability.[156] The OTS molecules homogeneously self-assembled via van der Waals forces into a monolayer on the NCM82 surface, as depicted in Figure 25d. A uniform monolayer with a thickness of 1.2 nm has been observed by TEM. The modified surface reveals electrolyte-phobic characteristics, exhibiting a significantly larger contact angle of 31.7° with an electrolyte drop compared to a contact angle of 3.3° for a pristine cathode. The electrolyte-phobic surface increases the initial charge transfer resistance (R_{ct}). However, after 70 cycles, OTS-NCM82 displays a smaller R_{ct} than the pristine NCM82, and its cyclability is also improved.

One major drawback of the protective layer coating strategy is that introducing a new interface will inevitably increase surface resistance and disturb ionic transport. Therefore, the layer thickness must be appropriately controlled, not hindering ionic transport through the surface.
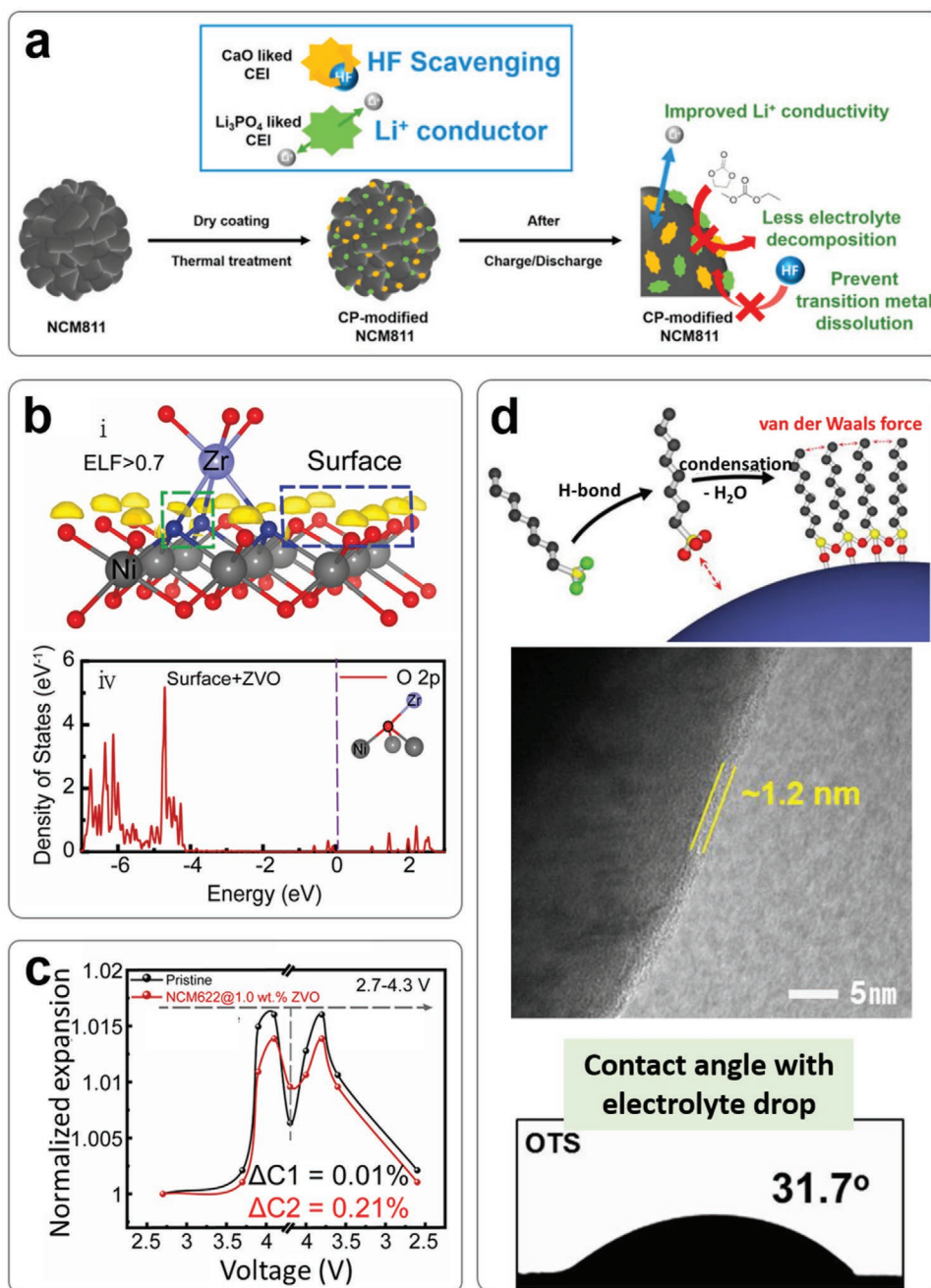
Figure 25. a) Stability mechanism of surface-modified NCM811 cathode material. b) Electron localization function (ELF) for the surface structure of LiNiO$_2$ with O–Ni–O termination reacted with ZrO$_6$ octahedron, and DOS of O 2p orbits of a Zr-modified NCM surface. c) Crystal lattice parameter evolution as a function of the voltage for two NCM622 cathodes. d) Illustration of the OTS coating process, SEM image, and contact angle result of OTS-coated NCM82. a) Reproduced with permission.[154] Copyright 2021, Elsevier. b,c) Reproduced with permission.[155] Copyright 2021, Elsevier. d) Reproduced with permission.[156] Copyright 2021, American Chemical Society.

4.1.6. Concentration Gradient

Concentration gradient control is also an interesting strategy to improve the stability of the Ni-rich cathodes by attempting to increase the storage capacity simultaneously. Similar to the case of microstructural manipulation, a core–shell structure has been employed for this strategy. The Ni-rich component located in the central part of the cathode particles is expected to increase

the capacity. In contrast, the Ni-deficient component located at the surface is expected to stabilize the particle structure during cycling.[157] Based on this concept, three different configurations have been proposed so far, including core–shell concentration gradients (CS), full concentration gradients (FCGs), and two-slopes full concentration gradients (TSFCGs).[158] **Figure 26**a illustrates an NCM811 particle with a typical core–shell concentration gradient structure.[159] Notably, the Ni concentration
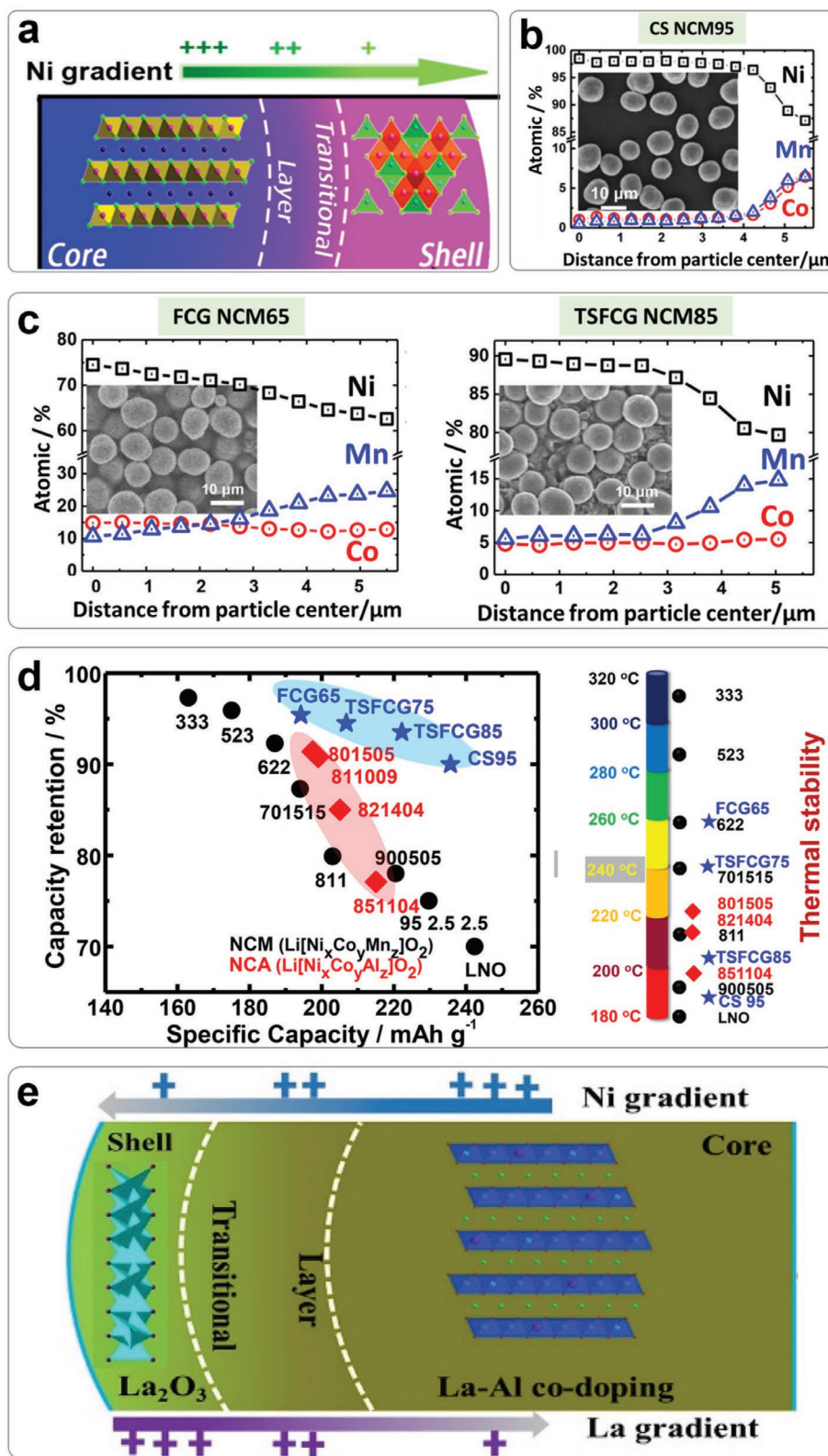
Figure 26. a) Illustration of a concentration gradient particle. b) The concentration gradient of various TM-contents in CS NCM95. c) The concentration gradient of various TM in FCG NCM65 and TSFCG NCM85. d) Specific capacity versus cycling stability of various layered cathodes, including gradient-type NCMs and conventional NCAs and NCMs. e) Illustration of a concentration gradient particle combined with surface coating. a) Reproduced with permission.[159] Copyright 2017, American Chemical Society. b) Reproduced with permission.[160] Copyright 2017, American Chemical Society. c,d) Reproduced with permission.[158] Copyright 2017, Wiley-VCH. e) Reproduced with permission.[161] Copyright 2019, Elsevier.

gradient is accompanied here by different phases. The Ni-deficient outer shell and Ni-rich inner core exist as spinel and layered phase, respectively. Between the two well-defined phases, a thin transitional layer can be observed. The tightly integrated structure with smooth phase transition enhances the binding between the bulk and surface in the particles.

Figure 26b presents an EDX line spectra of the cross-section of an NCM811@LiNiO$_2$ (CS NCM95) particle.[160] It can be seen that for such CS particles, a distinct drop of Ni atomic ratio is found in the transitional region. The composition profiles of the cross-section of FCG NCM65 and TSFCG NCM85 primary particles are shown in Figure 26c. For both FCG and TSFCG particles, the Ni concentration gradually changes and does not show a noticeable drop in Ni concentration. Well visible concentration gradients of TM can be seen within the particles. FCG NCM65 demonstrates two linear concentration profiles. The concentration of Ni gradually declines from the core to the surface. In contrast, the concentration of Mn increases, and the concentration of Co remains stable. In contrast, for TSFCG NCM85 particles, the Ni and Mn concentration profiles show two linear regions with different slopes. The Ni concentration declines slowly at the core, and then the declining slope becomes larger near the surface. This design can maximize the Ni concentration at the core for a higher capacity delivery and maximize the Mn concentration near the surface for a more robust outer structure. Such a remarkable concentration profile was recently obtained by Sun and co-workers to meet a balance between the high capacity retention of FCG NCM65 and the high specific capacity of CS NCM95.[158] Figure 26d presents a summary of the electrochemical and thermal stability of conventional and concentration gradient prepared cathodes. CS, FCG, and TSFCG-cathodes combine an overall superior capacity and electrode stability compared to their conventional counterparts with constant Ni-content. Especially among the three types of concentration gradient cathodes, TSFCG-cathodes achieve a relatively high specific capacity without compromising cyclability and thermal stability.

Finally, concentration gradient strategies combined with cation doping can also create modified epitaxial layers at the electrode particle surface. Incorporating electrochemically inert cations in concentration gradient during the cathode synthesis process will lead to ultrathin coatings, enabling the cathode to resist electrolyte erosion by HF and H$_2$O. To date, La-, Al-, and B-modified concentration gradient cathodes have been reported.[159,162] Cathode materials with a La and Ni gradient structure is depicted in Figure 26e. La-ion enrichment at the surface formed a layered olivine La$_2$O$_3$ structure, stabilizing the whole particle structure.[161] However, despite the achievements described above, concentration gradient strategies have limitations because electrode degradation induced by lattice mismatches and cation disorder cannot be avoided.

4.2. Anode

4.2.1. Graphite Anode

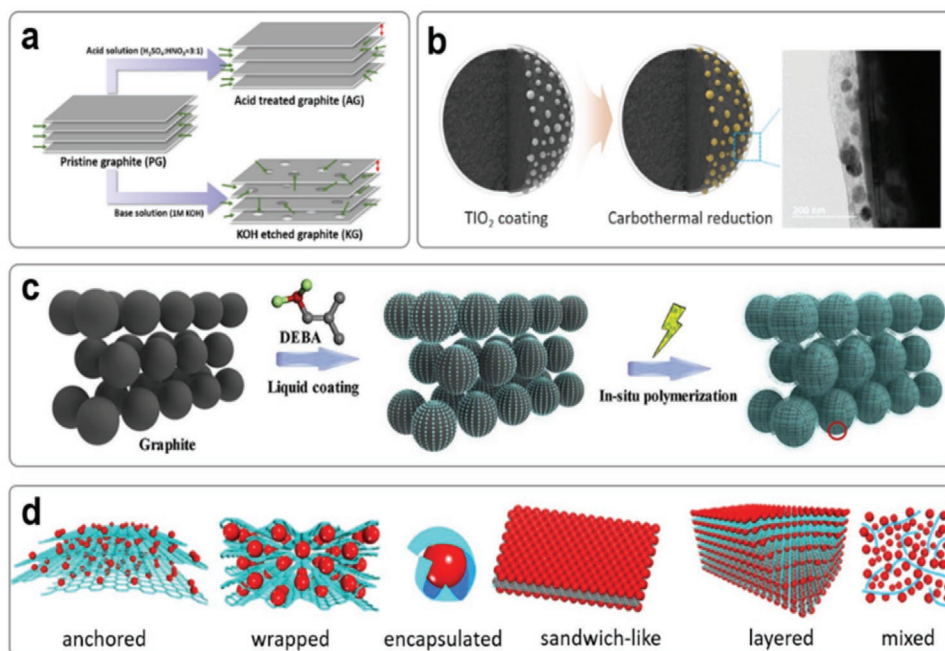The main strategies for achieving a favorable performance of graphite anodes are chemical treatment and coating. Chemical treatment aims to obtain an optimized graphite structure with expanded layer space. A major shortcoming of graphite is its narrow interlayer space of 0.335 nm, which restricts the number of Li$^+$ ions transported in the graphite interlayers and leads to exfoliation.[163] A commonly used method for expanding the graphite interlayer distance is treating conventional graphite with acid or base solutions.[164] As illustrated in **Figure 27**a, strong acid oxidation and base etching can convert pristine graphite into expanded graphite with porous voids. The higher specific surface area of the expanded graphite provides more active sites and facilitates the movement of Li$^+$ ions during the (de)intercalation process.

Apart from the strategy of surface treatment without introducing foreign materials, coating graphite with a functional layer is a promising approach to mitigate the degradation of graphite anodes. Especially, the formation of the SEI layer can be reduced through the synergy between graphite and coating material. Metal oxides and polymers are popular components that have been widely used as coating materials for graphite anodes.[96,168] For example, Park and co-workers plated TiO$_2$ nanoparticles at the surface of commercial graphite (Figure 27b).[165] Their results demonstrate that SEI formation is suppressed at TiO$_2$-coated graphite, while the electrochemical performance and thermal stability are improved.

Though metal oxide coatings have shown the ability to restrain the SEI layer growth, inorganic coating materials impose rigid structures. They are incompatible with SEI components that mainly consist of organic species. Applying organic artificial SEI layer as graphite coating is a smart strategy to form a continuous and more homogeneous artificial SEI layer before cycling. A robust and flexible artificial SEI layer composed of organic materials could subsequently guide a uniform SEI growth via chemical bonds and functional groups.

As indicated in Figure 27c, Zheng and co-workers synthesized a graphite anode with enhanced cycling stability by applying a functional 2,2-dimethylethenylboronic acid (DEBA) layer as an SEI precursor at the graphite surface.[166] In situ polymerization treatment produced a robust and flexible polymeric skeleton at the surface to control SEI formation. Strong chemical bonds are established between −COOH/−OH at graphite and the B–OH groups in DEBA, contributing to the enhanced mechanical strength of graphite anodes. Moreover, active intermediate species from electrolyte decomposition, such as PF$_6^-$, can be captured by electron-deficient B ions in DEBA.

A crucial improvement of graphite-based anodes emerged after graphene was discovered.[169] Graphene is a novel product and was acquired from the micro(nano)layer-exfoliation of graphite. Some bottleneck problems in conventional graphite anodes, such as capacity, mechanical failures, and poor stability, are overcome in graphene-based anodes. However, due to the high cost and difficult extraction mechanism of graphene sheets, graphene-based materials have always been applied together with metal oxide particles. Graphene sheets serve as a skeleton with a large specific surface area and high electronic conductivity.[169] The various types of graphene/metal oxides compositions have been comprehensively reviewed by Hassan et al., as summarized in Figure 27d, including anchored, wrapped, encapsulated, sandwiched, layered, and mixed models.[167]

**ADVANCED
SCIENCE NEWS**

www.advancedsciencenews.com

**ADVANCED
ENERGY
MATERIALS**

www.advenergymat.de

Figure 27. a) Schematic illustration of the preparation of acid-treated graphite and KOH-etched graphite. b) Illustration and TEM image of a TiO_2-coated graphite particle. c) Schematic illustration of the preparation of DEBA-treated graphite. d) Models of various graphene/metal oxide compositions. a) Reproduced with permission.[164] Copyright 2020, Elsevier. b) Reproduced with permission.[165] Copyright 2020, Elsevier. c) Reproduced with permission.[166] Copyright 2020, Elsevier. d) Reproduced with permission.[167] Copyright 2019, Elsevier.

4.2.2. Li-Metal Anode

To meet expectations in the commercialization of Li metal anodes, three major challenges have to be overcome: 1) Nonuniform Li deposition, which accelerates the detrimental Li dendrite growth; 2) considerable volume expansion that will result in a significant decrease of the Coulombic efficiency; 3) highly disordered SEI growth compared to other anode materials.[170] According to literature, these strategies can be divided into three categories: 1) Fabrication of artificial protective layers (metal oxides, metal fluorides, metal nitrides, solid electrolyte, polymers, composite materials, etc.); 2) construction of supporting scaffolds with electronic conductive materials (copper, nickel, carbon, etc.) to modulate Li plating; and 3) tailoring the uniform Li nucleation sites for uniform Li deposition.

Creating an artificial protective layer at the Li-metal surface has been a topic of intensive research for decades. Many studies of various materials and techniques for the preparation of these layers are reported in the literature.[175–179] Ideally, a protective layer should combine high mechanical strength with good flexibility and high ionic conductivity. It must be an electronically insulating material with a low dielectric constant and electrochemically and chemically stable. Mullins and co-workers recently comprehensively reviewed different kinds of protective layers for Li-metal electrodes.[180] Single components of inorganic or organic layers were commonly examined in the early stage of research. However, although inorganic layers have sufficient mechanical strength, they are brittle and crack during Li volume expansion/contraction. On the contrary, organic layers are flexible enough to endure these volume changes, but they cannot suppress dendrite growth. Hence, more attention has been paid to developing combined-component layers to use the best properties of each component. For example, Huang's group constructed an organic–inorganic artificial layer with a high mechanical modulus, superior shape compliance, and high ionic conductivity.[171] Rigid LiF particles are designed to anchor evenly on the soft poly(vinylidene-*co*-hexafluoropropylene) (PVDF-HFP) film, as shown in **Figure 28**a. This hybrid artificial layer is obtained by the strengths of LiF and PVDF-HFP, enabling uniform Li^+ permeation and deposition.

Another method to stabilize Li-metal anodes is applying scaffold materials with porous structures to achieve uniform Li deposition. Scaffold materials serve both as deposition substrates and current collectors. Copper foam, nickel foam, and carbon-based frameworks are the most frequently used current collectors in the studies because of their high electronic conductivity.[181,182] Shi and co-workers prepared graphene (nitrogen-doped)-coated porous copper substrates via CVD synthesis (Figure 28b).[172] The 3D modified current collector, on the one hand, provides a higher surface area for Li deposition. On the other hand, the strong binding between Li^+ in the electrolyte and graphene leads to a uniform Li^+ flux, thus contributing to a stable Li plating/stripping process without the formation of Li dendrites. Similarly, Cui and co-workers constructed hollow carbon nanospheres on copper foil to ensure a uniform Li deposition (Figure 28c).[173] Interestingly, the composite carbon nanosphere layer can freely move up and down the copper foil, slightly adjusting the space with Li volume variation during cycling. The corresponding theoretical calculations and experimental explorations have revealed that the uniform Li deposition, achieved by porous substrates, is attributed to the even distribution of the electric field at the substrate surface, thereby enabling a uniform Li^+ permeation.
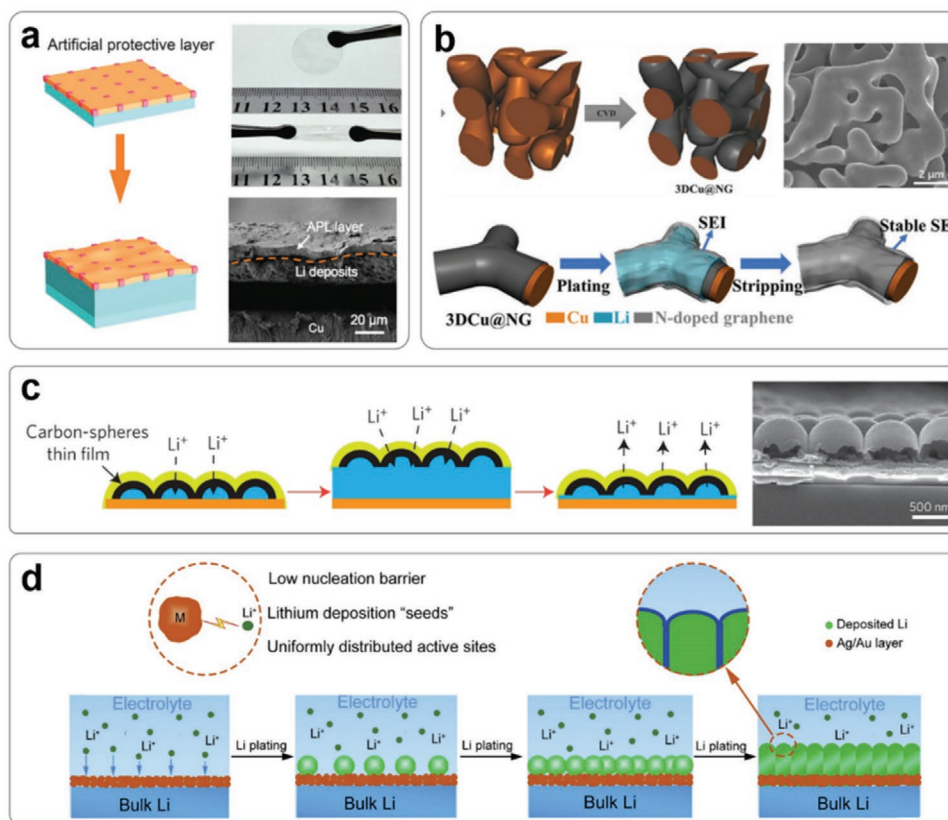
Figure 28. a) Schematic illustration and SEM image of Li deposition with a protective PVDF-HFP layer. b) Illustration and SEM image of Li deposition at a graphene-coated 3D copper substrate and c) at carbon-sphere modified copper substrate. d) Illustration of uniform Li deposition on a Ag/Au-coated copper substrate. a) Reproduced with permission.[171] Copyright 2018, Wiley-VCH. b) Reproduced with permission.[172] Copyright 2018, Wiley-VCH. c) Reproduced with permission.[173] Copyright 2014, Nature. d) Reproduced with permission.[174] Copyright 2020, Elsevier.

In principle, the growth of Li dendrites is a result of the self-amplifying behavior of Li deposition. Due to the inherent surface defects on Li foil, the nucleation initially started at defects because they are energetically more preferable for the Li reaction. Consequently, the nonuniformity of Li deposition will be gradually accelerated by the nonuniform nucleation during cycling, eventually leading to dendrite formation. Therefore, the uniformity of Li nucleation sites is also a vital factor for controllable Li deposition. Qian and co-workers proposed a heterogeneous metal layer at the Li-metal surface to form densely packed Li nucleation sites.[174] As illustrated in Figure 28d, an Ag/Au layer evenly homogeneously coats the Li foil surface and provides uniformly distributed nuclei seeds for Li deposition. In this case, Li grows into a columnar-structured morphology instead of a dendrite structure observed in the case of untreated Li-metal.

4.3. Electrolyte

4.3.1. Multifunctional Electrolyte Additives

A variety of organic species originating from electrolyte solvent decomposition reactions comprise the majority of CEI and SEI films. Thus, using multifunctional electrolyte additives is considered a versatile strategy to stabilize CEI and SEI films in Ni-rich cathode-based LIBs.[183–186] This stabilization mechanism is related to the higher HOMO energy level and lower LUMO energy level of the additives compared with conventional electrolyte solvents (e.g., EC, DMC, and DEC).[187–189] Hence, the electrolyte additives will oxidize at the cathode surface and reduce at the anode surface before the decomposition reactions of electrolyte solvents take place, resulting in the formation of homogeneous CEI and SEI films.[110,190,191] Apart from the film-forming ability, multifunctional additives also possess a high affinity toward HF and PF_5 species, which could mitigate the HF-driven degradation, such as TM ions dissolution and gas formation. Recently, several kinds of multifunctional additives have been proposed in studies, aiming at the effective formation of protective films at both cathode and anode surfaces.[192–197] **Table 3** summarizes the representative multifunctional electrolyte additives used in Ni-rich cathode-based LIBs, reported during the last five years.

One typical example of a novel multifunctional additive applied in $LiNi_{0.85}Co_{0.1}Mn_{0.05}O_2$ (NCM851005)/graphite full cells is methoxytri ethyleneoxypropy ltrimethoxysilane (MTE-TMS), which belongs to the group of silane derivatives (Si–O) (**Figure 29**a).[198] The reported cyclic voltammetry (CV) shows that a standard electrolyte with 1 wt% MTE-TMS reveals a couple of redox peaks at 3.75 and 1.5 V (vs Li/Li+) with a smaller potential interval (ΔV) compared with its additive-free

Table 3. Summary of multifunctional electrolyte additives used in Ni-rich cathode-based LIBs.

Additive	Functional group	Electrolyte	Electrode	Cut-off voltage (V vs Li+/Li)	Capacity retention	Refs.
Dimethoxydimethylsilane (DODSi, 0.25 wt%)	$-SO_2-$	1 M $LiPF_6$ in EC/EMC (1:2 wt%)	NCM811/graphite	3.0–4.5	60.8% after 100 cycles	[192]
Ethyl 4,4,4-trifluorobutyrate (ETFB, 1 wt%)	$-CF_3$, $-COO-$	1.15 M $LiPF_6$ in EC/EMC/DEC (2:5:3 wt%)	NCM71515[a]/graphite	3.0–4.35	84.8% after 300 cycles	[188]
Phenyl trans-styryl sulfone (PTSS, 1 wt%)	$-SO_2-$	1 M $LiPF_6$ in EC/DMC (3:7 wt%)	NCM811/graphite	3.0–4.35	63% after 100 cycles	[193]
p-toluenesulfonylmethyl isocyanide (TOSMIC, 3 wt%)	$-S-C(C\equiv N)-$	1 M $LiPF_6$ in EC/DEC (3:7 wt%)	NCA81505[b]/graphite	3.0–4.35	92% after 200 cycles	[189]
Methoxytriethyleneoxypropyltrimethoxysilane (MTE-TMS, 1 wt%)	$-SO_2-$	1 M $LiPF_6$ in EC/DEC (3:7 wt%)	NCM851005/graphite	3.0–4.3	84% after 100 cycles	[198]
Tripropargyl phosphate (TPP, 1 wt%)	$-C\equiv C-$	1 M $LiPF_6$ in EC/DMC/DEC (2:3:3 wt%)	NCM811/graphite	3.0–4.2	98.8% after 200 cycles	[190]
2-Thiophene sulfonamide (2-TS, 1 wt%)	C_4H_4S	1 M $LiPF_6$ in EC/EMC (1:2 wt%)	NCM811/graphite	2.8–4.2	91.6% after 500 cycles	[199]
2-Aminoethyldiphenyl borate (AEDB, 1 wt%)	$-B-O-$	1 M $LiPF_6$ in EC/DEC (3:7 wt%)	NCM851005/graphite	3.0–4.35	88% after 100 cycles	[200]
Adiponitrile ($C_6H_8N_2$, 1 wt%)	$-C\equiv N$	0.8 M LiTFSI + 0.2 M LiDFOB + 0.5 M $LiPF_6$ in EMC/FEC (3:1 wt%)	NCMA[c]/Li	2.7–4.3	75% after 830 cycles	[194]
(trifluoroethoxy)pentafluorocyclotriphosphazene (TFPN, 5 wt%)	$-P=N-$, $-P-F-$	1 M $LiPF_6$ EC/DMC (3:7, wt%)	NCM811/Li	2.8–4.2	87.5% after 100 cycles	[195]
Diphenyl sulfone (DPS, 0.5 wt%)	$-SO_2-$	1 M $LiPF_6$ in EC/DMC/DEC (1:1:1 wt%)	NCM811/Li	3.0–4.3	57% after 500 cycles	[183]
Bis(4florophenyl) sulfone (BFS, 0.5 wt%)	$-SO_2-$	1 M $LiPF_6$ in EC/DMC/DEC (1:1:1 wt%)	NCM811/Li	3.0–4.3	44.8% after 500 cycles	[183]

[a]$LiNi_{0.7}Co_{0.15}Mn_{0.15}O_2$; [b]$LiNi_{0.8}Co_{0.15}Al_{0.05}O_2$; [c]$LiNi_{0.73}Co_{0.10}Mn_{0.15}Al_{0.02}O_2$.

counterpart. Further characterizations demonstrate that the MTE-TMS also stabilizes the formation of the CEI and SEI films at the electrodes and that the crack generation and TM dissolution is significantly reduced.
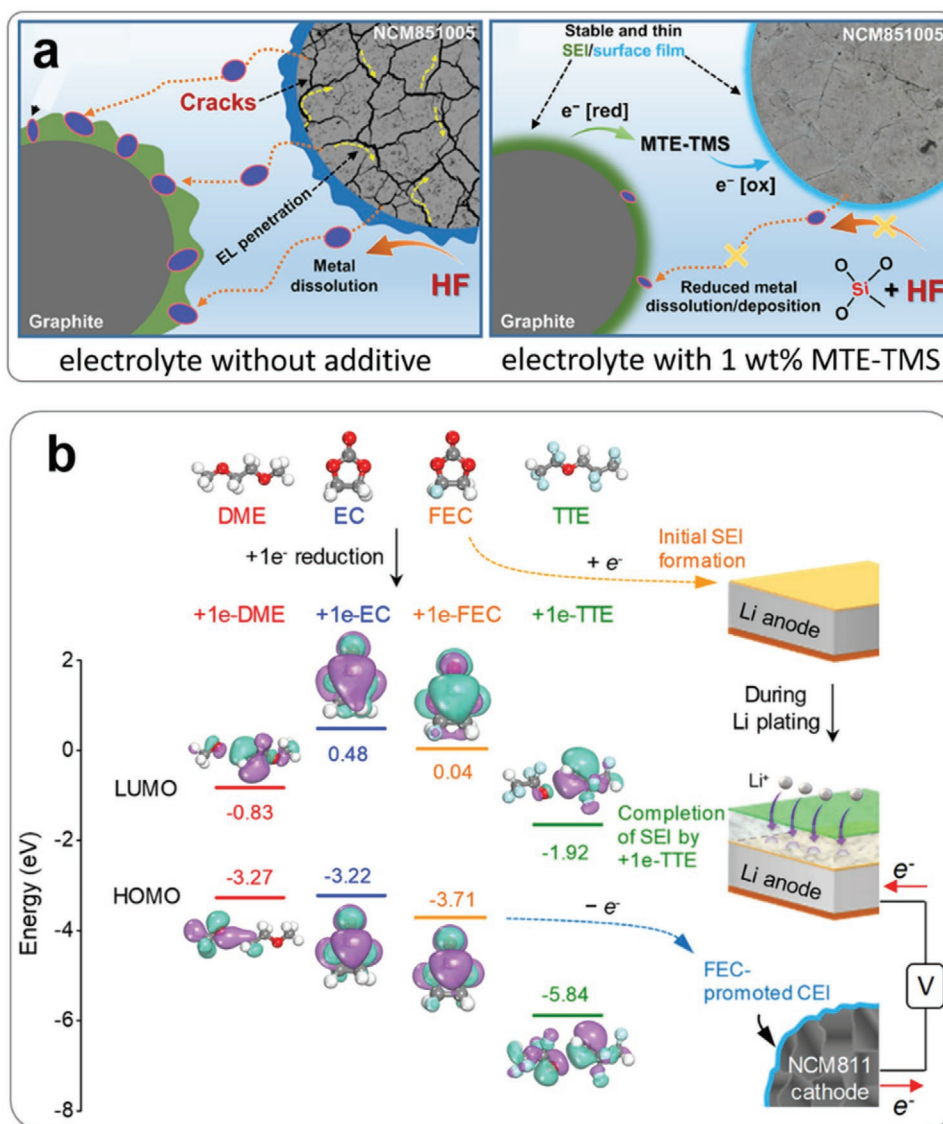
The interfacial engineering for both cathodes and anodes can also be achieved by the interaction between additive and electrolyte solvents. Choi and co-workers prepared ether-based electrolyte by 1,1,2,2-tetrafluoroethyl-2,2,3,3-tetrafluoropropyl ether (TTE) with 1 wt% fluoroethylene carbonate (FEC) as additive, and investigated its effect in NCM811/Li full cells.[201] Figure 29b displays the HOMO–LUMO energy levels of various solvents (DME, EC, TTE) and additive (FEC) under their reduced states (+1e− reduction). It is known that neutral FEC has the lowest LUMO energy level among all components. Therefore, it will favorably initiate and control the SEI formation. The TTE solvent dominantly contributes to the subsequent SEI formation through further reduction on anode because the LUMO energy level of the as-denoted reduced state +1e-TTE after the first cycle of charging is much lower than +1e-FEC. FEC also promotes the CEI formation at the cathode surface because the reduced state +1e-FEC has a higher HOMO energy level than neutral DME. The NCM811/Li cells demonstrate superior cycling stability beyond 150 cycles with a capacity retention of 84.2%. An intact morphology without cracks is observed in NCM811 particles. More uniform SEI films with a more compact morphology are formed at Li-metal anode.

5. Summary and Outlook

The expanding production scale of electric vehicles during the last few years has been strongly dependent on the continuous improvement of LIBs. Among all sorts of cathode materials, Ni-rich cathodes have drawn massive attention as near-term candidates for commercialization due to their high capacity, favorable rate capability, and reasonable cost.[4] One can see significant successes in the EV market with Ni-rich cathode-based LIBs embedded in EVs, such as NCM811/graphite LIBs applied in the Nio ES6 with an energy density of 737 Wh L−1, and NCA-graphite/silicon oxide LIBs applied in Tesla Model 3 with an energy density of 866 Wh L−1. Nevertheless, driven by the ambition for achieving even higher energy densities, more advanced battery materials are definitely needed to meet such goals. In addition, an in-depth understanding of electrochemical fatigue mechanisms is important for further optimization of the LIB chemistry.

This review thoroughly discussed the degradation upon cycling originating from the cathodes, electrolytes, and anodes in Ni-rich cathode-based LIBs. As an essential component in LIB, Ni-rich cathodes undergo the most destructive and complex degradation processes. These processes can be categorized into the negative reactions induced by RLCs, cation disorder (especially for Li/Ni mixing), surface reconstruction (from layered-to-spinel and rock-salt phase), gas generation, transition metal dissolution, microcracks propagation (intragranular and intergranular), and the fragile thermal stability. The findings emphasize the importance of crystal structure stability with respect to the decreased strength of metal–oxygen bonding at high SOC and high temperatures. In response to these negative effects, various strategies have been proposed, including optimizing synthesis methods, fabricating single-crystal particles, optimizing microstructures, doping foreign ions, coating protective layers, and designing concentration gradients. All these strategies are designed to experimentally enhance the

**ADVANCED
SCIENCE NEWS**

www.advancedsciencenews.com

**ADVANCED
ENERGY
MATERIALS**

www.advenergymat.de

Figure 29. a) Schematic representation of interfacial phenomena occurring in the NCM851005/graphite full-cells with and without electrolyte additive. b) HOMO–LUMO energy levels of negatively charged electrolyte molecules, and schematic representation of the interface occurring in an NCM811/Li-metal full-cell. a) Reproduced with permission.[198] Copyright 2020, Elsevier. b) Reproduced with permission.[201] Copyright 2020, Elsevier.

performance of Ni-rich cathodes. However, as discussed, one universal solution cannot be expected to solve all problems because each strategy has its clear limits.

Moving to the anode side, two typical anodes (graphite and Li-metal) that are commonly coupled with Ni-rich cathodes in the presented studies have been discussed. Graphite, as the most successful intercalation material, has been widely applied in the battery industry. At the same time, the challenges of volume expansion, exfoliation, inferior SEI film formation, and nonuniform Li deposition still need to be handled carefully. Surface coating and chemical treatments help to stabilize graphite anode. Additionally, the introduction of hybrid graphite-based anodes (graphite/silicon, graphite/silicon oxide, graphene/metal oxide, etc.) offers alternative directions for further developments in the anode design.

Regarding Li-metal anode, it is undoubtedly the most promising anode that will enable the considerable growth of specific energy needed for the next generation of LIBs. However, the high (electro)chemical activity of Li-metal impedes the practical application of the Li-metal anode. Many approaches devoted to controlling the Li deposition are proposed, including applying artificial layers, introducing stable deposition skeletons and uniform nucleation sites at the electrode surface for Li deposition. These methods bring significant improvements in lab-scale demonstrations. Still, the challenge remains in large-scale manufacturing. Remarkably, the phenomenon of chemical crosstalk between cathodes and anodes has recently drawn rising attention. Some CEI/SEI film species have been found to dissolve in the electrolyte, penetrate through the separator, and react at the surface of the anode or

cathode, leading to accelerated SEI and CEI formation. Thus, the chemical crossover of components in full cells should be considered when modifications are adopted for both cathode and anode materials.

One more major problem of Ni-rich cathode is the degradation related to the electrolyte. The decomposition of conventional electrolytes poses a risk to battery safety in terms of HF and gas generation. Also, the decomposition species are the major components of the CEI and SEI films, causing large lithium inventory losses. The use of multifunctional electrolyte additives with HF-scavenging ability is promising to stabilize the interfaces at both cathodes and anodes simultaneously. A brief discussion on the remaining challenges in solid-state Ni-rich cathodes is also given. In particular, cracking induced by pellet preparation and interfacial side reactions hold primary responsibilities for the degradation of all-solid-state Li-ion batteries.

The search for higher efficiencies and upscaling battery designs is under severe pressure of the exponential growth of the global EV market. More advanced materials and battery manufacturing methods are needed. Overseeing the recent progress in Ni-rich cathode-based LIBs, the following research directions are envisioned for the near future:

1) The development of Ni-rich/Co-less layered cathode materials will play a strategic role because of the critical shortage of cobalt sources in the world.
2) In-depth investigations on the degradation mechanisms of newly proposed materials are of utmost importance since the various implemented modifications might alter the lattice structure or surface environment of the cathode materials, leading to a different deterioration processes.
3) Atomic mismatches and electronic structure distortion could diminish the electrode stability significantly. Advanced characterization techniques, such as XANES, HRPD, HR-STEM, HAADF-STEM, etc., are considered essential in assisting scientists to fundamentally understand the degradation mechanism of battery materials, especially when these techniques are combined with in operando method and theoretical calculations.
4) The combined synergistic effect of several strategies could offer additional performance benefits to new Ni-rich cathode materials, such as applying protective layers and using elemental concentration gradients inside the active electrode particles.
5) Further progress of anode-free LIBs will lead to new methods for the modification of uniform Li deposition, promising an excellent possibility for adaptation in the commercial LIBs in the near future.
6) Empowering multifunction electrolytes with nonflam0mable or oxygen-scavenging capability would be further reassuring the safety concerns. Additionally, replacing liquid electrolytes with solid-state electrolytes has undoubtedly been a clear roadmap in battery science.

With the growing efforts committed to improving Ni-rich cathode-based LIBs, it is to be expected that numerous exciting new opportunities will continuously arise shortly in the search for high-performance Li-ion batteries.

[1] W. Liu, P. Oh, X. Liu, M. J. Lee, W. Cho, S. Chae, Y. Kim, J. Cho, *Angew. Chem., Int. Ed. Engl.* **2015**, *54*, 4440.
[2] J. Kim, H. Lee, H. Cha, M. Yoon, M. Park, J. Cho, *Adv. Energy Mater.* **2018**, *8*, 1870023.
[3] S.-T. Myung, F. Maglia, K.-J. Park, C. S. Yoon, P. Lamp, S.-J. Kim, Y.-K. Sun, *ACS Energy Lett.* **2016**, *2*, 196.
[4] W. Li, E. M. Erickson, A. Manthiram, *Nat. Energy* **2020**, *5*, 26.
[5] A. Manthiram, B. Song, W. Li, *Energy Storage Mater.* **2017**, *6*, 125.
[6] L. de Biasi, B. Schwarz, T. Brezesinski, P. Hartmann, J. Janek, H. Ehrenberg, *Adv. Mater.* **2019**, *31*, 1900985.
[7] J. P. Pender, G. Jha, D. H. Youn, J. M. Ziegler, I. Andoni, E. J. Choi, A. Heller, B. S. Dunn, P. S. Weiss, R. M. Penner, C. B. Mullins, *ACS Nano* **2020**, *14*, 1243.
[8] V. Gopalakrishnan, A. Sundararajan, P. Omprakash, D. Bhat Panemangalore, *J. Electrochem. Soc.* **2021**, *168*, 040541.
[9] D. Lin, Y. Liu, Y. Cui, *Nat. Nanotechnol.* **2017**, *12*, 194.
[10] T. Li, X.-Z. Yuan, L. Zhang, D. Song, K. Shi, C. Bock, *Electrochem. Energy Rev.* **2019**, *3*, 43.
[11] L. D. Dyer, B. S. Borie Jr., G. P. Smith, *J. Am. Chem. Soc.* **1954**, *76*, 1499.
[12] J. U. Choi, N. Voronina, Y. K. Sun, S. T. Myung, *Adv. Energy Mater.* **2020**, *10*, 2002027.
[13] P. Teichert, G. G. Eshetu, H. Jahnke, E. Figgemeier, *Batteries* **2020**, *6*, 8.
[14] S. Cui, Y. Wei, T. Liu, W. Deng, Z. Hu, Y. Su, H. Li, M. Li, H. Guo, Y. Duan, W. Wang, M. Rao, J. Zheng, X. Wang, F. Pan, *Adv. Energy Mater.* **2016**, *6*, 1501309.
[15] C. Xu, K. Marker, J. Lee, A. Mahadevegowda, P. J. Reeves, S. J. Day, M. F. Groh, S. P. Emge, C. Ducati, B. L. Mehdi, C. C. Tang, C. P. Grey, *Nat. Mater.* **2021**, *20*, 84.
[16] W. Li, J. N. Reimers, J. R. Dahn, *Solid State Ionics* **1993**, *67*, 123.
[17] C. Liang, F. Kong, R. C. Longo, S. Kc, J.-S. Kim, S. Jeon, S. Choi, K. Cho, *J. Phys. Chem. C* **2016**, *120*, 6383.
[18] H.-H. Ryu, K.-J. Park, C. S. Yoon, Y.-K. Sun, *Chem. Mater.* **2018**, *30*, 1155.
[19] X. Wang, Y. L. Ding, Y. P. Deng, Z. Chen, *Adv. Energy Mater.* **2020**, *10*, 1903864.
[20] M. Dixit, B. Markovsky, F. Schipper, D. Aurbach, D. T. Major, *J. Phys. Chem. C* **2017**, *121*, 22628.
[21] W. Li, H. Y. Asl, Q. Xie, A. Manthiram, *J. Am. Chem. Soc.* **2019**, *141*, 5097.
[22] H.-H. Sun, A. Manthiram, *Chem. Mater.* **2017**, *29*, 8486.

**ADVANCED
SCIENCE NEWS**

www.advancedsciencenews.com

**ADVANCED
ENERGY
MATERIALS**

www.advenergymat.de

[23] C. Xu, P. J. Reeves, Q. Jacquet, C. P. Grey, *Adv. Energy Mater.* **2021**, *11*, 2003404.

[24] S. S. Zhang, *J. Energy Chem.* **2020**, *41*, 135.

[25] H. Li, A. Liu, N. Zhang, Y. Wang, S. Yin, H. Wu, J. R. Dahn, *Chem. Mater.* **2019**, *31*, 7574.

[26] W. Lee, S. Muhammad, T. Kim, H. Kim, E. Lee, M. Jeong, S. Son, J.-H. Ryou, W.-S. Yoon, *Adv. Energy Mater.* **2018**, *8*, 228592.

[27] Q. Tao, C. Shi, J. Li, G. Chen, Z. Xue, J. Wang, S. Wang, H. Jin, *Mater. Chem. Front.* **2021**, *5*, 2607.

[28] Y. Su, L. Li, G. Chen, L. Chen, N. Li, Y. Lu, L. Bao, S. Chen, F. Wu, *Chin. J. Chem.* **2020**, *39*, 189.

[29] D.-H. Cho, C.-H. Jo, W. Cho, Y.-J. Kim, H. Yashiro, Y.-K. Sun, S.-T. Myung, *J. Electrochem. Soc.* **2014**, *161*, A920.

[30] Y. Su, G. Chen, L. Chen, L. Li, C. Li, R. Ding, J. Liu, Z. Lv, Y. Lu, L. Bao, G. Tan, S. Chen, F. Wu, *Front. Chem.* **2020**, *8*, 573.

[31] H. S. Liu, Z. R. Zhang, Z. L. Gong, Y. Yang, *Electrochem. Solid-State Lett.* **2004**, *7*, A109.

[32] J. H. Jo, C.-H. Jo, H. Yashiro, S.-J. Kim, S.-T. Myung, *J. Power Sources* **2016**, *313*, https://doi.org/10.1016/j.jpowsour.2016.02.015.

[33] S. Xu, C. Du, X. Xu, G. Han, P. Zuo, X. Cheng, Y. Ma, G. Yin, *Electrochim. Acta* **2017**, *248*, 534.

[34] J.-H. Park, B. Choi, Y.-S. Kang, S. Y. Park, D. J. Yun, I. Park, J. H. Shim, J.-H. Park, H. N. Han, K. Park, *Energy Technol.* **2018**, *6*, 1361.

[35] Z. Yu, X. Qu, T. Wan, A. Dou, Y. Zhou, X. Peng, M. Su, Y. Liu, D. Chu, *ACS Appl. Mater. Interfaces* **2020**, *12*, 40393.

[36] J. Zhao, W. Zhang, A. Huq, S. T. Misture, B. Zhang, S. Guo, L. Wu, Y. Zhu, Z. Chen, K. Amine, F. Pan, J. Bai, F. Wang, *Adv. Energy Mater.* **2017**, *7*, 1601266.

[37] S. Wang, W. Hua, A. Missyul, M. S. D. Darma, A. Tayal, S. Indris, H. Ehrenberg, L. Liu, M. Knapp, *Adv. Funct. Mater.* **2021**, *31*, 2009949.

[38] X. Li, A. Gao, Z. Tang, F. Meng, T. Shang, S. Guo, J. Ding, Y. Luo, D. Xiao, X. Wang, D. Su, Q. Zhang, L. Gu, *Adv. Funct. Mater.* **2021**, *31*, 2010291.

[39] A. Gao, X. Li, F. Meng, S. Guo, X. Lu, D. Su, X. Wang, Q. Zhang, L. Gu, *Small Methods* **2021**, *5*, 2000730.

[40] Y.-S. Kang, S. Y. Park, K. Ito, Y. Kubo, Y. Shin, D. Y. Kim, D.-H. Seo, S. Kim, J.-H. Park, S.-G. Doo, M. Koh, J. A. Seo, K. Park, *J. Power Sources* **2021**, *490*, 229542.

[41] S. S. Zhang, *Energy Storage Mater.* **2020**, *24*, 247.

[42] S. Li, Z. Yao, J. Zheng, M. Fu, J. Cen, S. Hwang, H. Jin, A. Orlov, L. Gu, S. Wang, Z. Chen, D. Su, *Angew. Chem., Int. Ed. Engl.* **2020**, *132*, 22276.

[43] L. Zou, W. Zhao, H. Jia, J. Zheng, L. Li, D. P. Abraham, G. Chen, J. R. Croy, J.-G. Zhang, C. Wang, *Chem. Mater.* **2020**, *32*, 2884.

[44] J. Zhu, S. Sharifi-Asl, J. C. Garcia, H. H. Iddir, J. R. Croy, R. Shahbazian-Yassar, G. Chen, *ACS Appl. Energy Mater.* **2020**, *3*, 4799.

[45] X. Tian, Y. Yi, B. Fang, P. Yang, T. Wang, P. Liu, L. Qu, M. Li, S. Zhang, *Chem. Mater.* **2020**, *32*, 9821.

[46] S. E. Renfrew, L. A. Kaufman, B. D. McCloskey, *ACS Appl. Mater. Interfaces* **2019**, *11*, 34913.

[47] S. E. Renfrew, B. D. McCloskey, *ACS Appl. Energy Mater.* **2019**, *2*, 3762.

[48] D. Streich, C. Erk, A. Guéguen, P. Müller, F.-F. Chesneau, E. J. Berg, *J. Phys. Chem. C* **2017**, *121*, 13481.

[49] W. Li, *J. Electrochem. Soc.* **2020**, *167*, 100510.

[50] J. Kim, H. Ma, H. Cha, H. Lee, J. Sung, M. Seo, P. Oh, M. Park, J. Cho, *Energy Environ. Sci.* **2018**, *11*, 1449.

[51] D.-S. Ko, J.-H. Park, S. Park, Y. N. Ham, S. J. Ahn, J.-H. Park, H. N. Han, E. Lee, W. S. Jeon, C. Jung, *Nano Energy* **2019**, *56*, 434.

[52] R. Jung, F. Linsenmann, R. Thomas, J. Wandt, S. Solchenbach, F. Maglia, C. Stinner, M. Tromp, H. A. Gasteiger, *J. Electrochem. Soc.* **2019**, *166*, A378.

[53] S. Yin, W. Deng, J. Chen, X. Gao, G. Zou, H. Hou, X. Ji, *Nano Energy* **2021**, *83*, 105854.

[54] Q. Lin, W. Guan, J. Zhou, J. Meng, W. Huang, T. Chen, Q. Gao, X. Wei, Y. Zeng, J. Li, Z. Zhang, *Nano Energy* **2020**, *76*, 105021.

[55] K. Min, E. Cho, *Phys. Chem. Chem. Phys.* **2018**, *20*, 9045.

[56] G. W. Nam, N.-Y. Park, K.-J. Park, J. Yang, J. Liu, C. S. Yoon, Y.-K. Sun, *ACS Energy Lett.* **2019**, *4*, 2995.

[57] T. M. M. Heenan, A. Wade, C. Tan, J. E. Parker, D. Matras, A. S. Leach, J. B. Robinson, A. Llewellyn, A. Dimitrijevic, R. Jervis, P. D. Quinn, D. J. L. Brett, P. R. Shearing, *Adv. Energy Mater.* **2020**, *10*, 1321.

[58] J. Park, H. Zhao, S. D. Kang, K. Lim, C. C. Chen, Y. S. Yu, R. D. Braatz, D. A. Shapiro, J. Hong, M. F. Toney, M. Z. Bazant, W. C. Chueh, *Nat. Mater.* **2021**, *20*, 991.

[59] H.-H. Ryu, B. Namkoong, J.-H. Kim, I. Belharouak, C. S. Yoon, Y.-K. Sun, *ACS Energy Lett.* **2021**, *6*, 2726.

[60] H. Wu, C. Qin, K. Wang, X. Han, M. Sui, P. Yan, *J. Power Sources* **2021**, *503*, 230066.

[61] J. Duan, X. Tang, H. Dai, Y. Yang, W. Wu, X. Wei, Y. Huang, *Electrochem. Energy Rev.* **2019**, *3*, https://doi.org/10.1007/s41918-019-00060-4.

[62] D. Hu, Q. Zhang, J. Tian, L. Chen, N. Li, Y. Su, L. Bao, Y. Lu, D. Cao, K. Yan, S. Chen, F. Wu, *ACS Appl. Mater. Interfaces* **2021**, *13*, 6286.

[63] L. Geng, J. Liu, D. L. Wood, Y. Qin, W. Lu, C. J. Jafta, Y. Bai, I. Belharouak, *ACS Appl. Energy Mater.* **2020**, *3*, 7058.

[64] X. Liu, G. L. Xu, L. Yin, I. Hwang, Y. Li, L. Lu, W. Xu, X. Zhang, Y. Chen, Y. Ren, C. J. Sun, Z. Chen, M. Ouyang, K. Amine, *J. Am. Chem. Soc.* **2020**, *142*, 19745.

[65] E. Lee, S. Muhammad, T. Kim, H. Kim, W. Lee, W. S. Yoon, *Adv. Sci.* **2020**, *7*, 1902413.

[66] J. Asenbauer, T. Eisenmann, M. Kuenzel, A. Kazzazi, Z. Chen, D. Bresser, *Sustainable Energy Fuels* **2020**, *4*, 5387.

[67] S. Komaba, N. Kumagai, Y. Kataoka, *Electrochim. Acta* **2002**, *47*, 1229.

[68] V. A. Sethuraman, L. J. Hardwick, V. Srinivasan, R. Kostecki, *J. Power Sources* **2010**, *195*, 3655.

[69] N. Lin, Z. Jia, Z. Wang, H. Zhao, G. Ai, X. Song, Y. Bai, V. Battaglia, C. Sun, J. Qiao, K. Wu, G. Liu, *J. Power Sources* **2017**, *365*, 235.

[70] S. Schweidler, L. de Biasi, A. Schiele, P. Hartmann, T. Brezesinski, J. Janek, *J. Phys. Chem. C* **2018**, *122*, 8829.

[71] A. Tornheim, R. Sahore, M. He, J. R. Croy, Z. Zhang, *J. Electrochem. Soc.* **2018**, *165*, A3360.

[72] W. Li, U. H. Kim, A. Dolocan, Y. K. Sun, A. Manthiram, *ACS Nano* **2017**, *11*, 5853.

[73] S. Klein, P. Barmann, T. Beuse, K. Borzutzki, J. E. Frerichs, J. Kasnatscheew, M. Winter, T. Placke, *ChemSusChem* **2021**, *14*, 595.

[74] L. Huang, G. Xu, X. Du, J. Li, B. Xie, H. Liu, P. Han, S. Dong, G. Cui, L. Chen, *Adv. Sci.* **2021**, *8*, 2100676.

[75] M. K. Aslam, Y. Niu, T. Hussain, H. Tabassum, W. Tang, M. Xu, R. Ahuja, *Nano Energy* **2021**, *86*, 106142.

[76] X. Fan, L. Chen, O. Borodin, X. Ji, J. Chen, S. Hou, T. Deng, J. Zheng, C. Yang, S. C. Liou, K. Amine, K. Xu, C. Wang, *Nat. Nanotechnol.* **2018**, *13*, 715.

[77] D. Wang, W. Zhang, W. Zheng, X. Cui, T. Rojo, Q. Zhang, *Adv. Sci.* **2017**, *4*, 1600168.

[78] W. Xu, J. Wang, F. Ding, X. Chen, E. Nasybulin, Y. Zhang, J.-G. Zhang, *Energy Environ. Sci.* **2014**, *7*, 513.

[79] M. Jiang, Q. Zhang, D. L. Danilov, R.-A. Eichel, P. H. L. Notten, *ACS Appl. Energy Mater.* **2021**, *4*, 10333.

[80] B. Song, I. Dhiman, J. C. Carothers, G. M. Veith, J. Liu, H. Z. Bilheux, A. Huq, *ACS Energy Lett.* **2019**, *4*, 2402.

[81] S. H. Lee, J. Y. Hwang, J. Ming, Z. Cao, H. A. Nguyen, H. G. Jung, J. Kim, Y. K. Sun, *Adv. Energy Mater.* **2020**, *10*, 2153.

[82] S. J. Park, J. Y. Hwang, C. S. Yoon, H. G. Jung, Y. K. Sun, *ACS Appl. Mater. Interfaces* **2018**, *10*, 17985.

[83] J. Langdon, A. Manthiram, *Adv. Funct. Mater.* **2021**, *31*, 2010267.

[84] J. Fu, D. Mu, B. Wu, J. Bi, H. Cui, H. Yang, H. Wu, F. Wu, *ACS Appl. Mater. Interfaces* **2018**, *10*, 19704.

[85] D. Y. Kim, I. Park, Y. Shin, D.-H. Seo, Y.-S. Kang, S.-G. Doo, M. Koh, *J. Power Sources* **2019**, *418*, 74.

[86] J. Henschel, C. Peschel, S. Klein, F. Horsthemke, M. Winter, S. Nowak, *Angew. Chem., Int. Ed. Engl.* **2020**, *59*, 6128.

[87] Q. Wang, L. Jiang, Y. Yu, J. Sun, *Nano Energy* **2019**, *55*, 93.

[88] C. W. L. Xing, W. Li, M. Xu, X. Meng, S. Zhao, *J. Phys. Chem. B* **2009**, *113*, 5181.

[89] K. Kumai, H. Miyashiro, Y. Kobayashi, K. Takei, R. Ishikawa, *J. Power Sources* **1999**, *81*, 715.

[90] I. Takahashi, H. Kiuchi, A. Ohma, T. Fukunaga, E. Matsubara, *J. Phys. Chem. C* **2020**, *124*, 9243.

[91] C. L. Campion, W. Li, B. L. Lucht, *J. Electrochem. Soc.* **2005**, *152*, A2327.

[92] Q. Li, Y. Wang, X. Wang, X. Sun, J. N. Zhang, X. Yu, H. Li, *ACS Appl. Mater. Interfaces* **2020**, *12*, 2319.

[93] Y. Wu, X. Liu, L. Wang, X. Feng, D. Ren, Y. Li, X. Rui, Y. Wang, X. Han, G.-L. Xu, H. Wang, L. Lu, X. He, K. Amine, M. Ouyang, *Energy Storage Mater.* **2021**, *37*, 77.

[94] M. Jiang, X. Wu, Q. Zhang, D. L. Danilov, R.-A. Eichel, P. H. L. Notten, *Electrochim. Acta* **2021**, *398*, 139316.

[95] M. Mao, B. Huang, Q. Li, C. Wang, Y.-B. He, F. Kang, *Nano Energy* **2020**, *78*, 105282.

[96] S. Fang, D. Jackson, M. L. Dreibelbis, T. F. Kuech, R. J. Hamers, *J. Power Sources* **2018**, *373*, 184.

[97] H. M. K. Sari, X. Li, *Adv. Energy Mater.* **2019**, *9*, 1970151.

[98] T. Yoshinari, R. Koerver, P. Hofmann, Y. Uchimoto, W. G. Zeier, J. Janek, *ACS Appl. Mater. Interfaces* **2019**, *11*, 23244.

[99] Y. A. Heidy Visbal, S. Ito, T. Watanabe, *J. Power Sources* **2016**, *314*, 85.

[100] N. Gauthier, C. Courrèges, J. Demeaux, C. Tessier, H. Martinez, *Appl. Surf. Sci.* **2020**, *501*, 144266.

[101] X. Li, Q. Sun, Z. Wang, D. Song, H. Zhang, X. Shi, C. Li, L. Zhang, L. Zhu, *J. Power Sources* **2020**, *456*, 227997.

[102] X. Liu, B. Zheng, J. Zhao, W. Zhao, Z. Liang, Y. Su, C. Xie, K. Zhou, Y. Xiang, J. Zhu, H. Wang, G. Zhong, Z. Gong, J. Huang, Y. Yang, *Adv. Energy Mater.* **2021**, *11*, 2003583.

[103] A. Y. Kim, F. Strauss, T. Bartsch, J. H. Teo, T. Hatsukade, A. Mazilkin, J. Janek, P. Hartmann, T. Brezesinski, *Chem. Mater.* **2019**, *31*, 9664.

[104] S. H. Jung, U. H. Kim, J. H. Kim, S. Jun, C. S. Yoon, Y. S. Jung, Y. K. Sun, *Adv. Energy Mater.* **2019**, *10*, 1903360.

[105] J.-M. Kim, X. Zhang, J.-G. Zhang, A. Manthiram, Y. S. Meng, W. Xu, *Mater. Today* **2021**, *46*, 155.

[106] H. Lv, C. Li, Z. Zhao, B. Wu, D. Mu, *J. Energy Chem.* **2021**, *60*, 435.

[107] S. He, S. Huang, S. Wang, I. Mizota, X. Liu, X. Hou, *Energy Fuels* **2020**, *35*, 944.

[108] X. B. Cheng, R. Zhang, C. Z. Zhao, Q. Zhang, *Chem. Rev.* **2017**, *117*, 10403.

[109] X. Rao, Y. Lou, S. Zhong, L. Wang, B. Li, Y. Xiao, W. Peng, X. Zhong, J. Huang, *J. Electroanal. Chem.* **2021**, *897*, 115499.

[110] K. Kim, H. Ma, S. Park, N.-S. Choi, *ACS Energy Lett.* **2020**, *5*, 1537.

[111] T. van Ree, *Curr. Opin. Electrochem.* **2020**, *21*, 22.

[112] M. Wood, J. Li, R. E. Ruther, Z. Du, E. C. Self, H. M. Meyer, C. Daniel, I. Belharouak, D. L. Wood, *Energy Storage Mater.* **2020**, *24*, 188.

[113] K. Yuan, N. Li, R. Ning, C. Shen, N. Hu, M. Bai, K. Zhang, Z. Tian, L. Shao, Z. Hu, X. Xu, T. Yu, K. Xie, *Nano Energy* **2020**, *78*, 105239.

[114] Z. Tang, J. Bao, Q. Du, Y. Shao, M. Gao, B. Zou, C. Chen, *ACS Appl. Mater. Interfaces* **2016**, *8*, 34879.

[115] Y. Su, Q. Zhang, L. Chen, L. Bao, Y. Lu, Q. Shi, J. Wang, S. Chen, F. Wu, *ACS Appl. Mater. Interfaces* **2020**, *12*, 37208.

[116] Y. Shi, M. Zhang, C. Fang, Y. S. Meng, *J. Power Sources* **2018**, *394*, 114.

[117] Y. Chen, P. Li, Y. Li, Q. Su, L. Xue, Q. Han, G. Cao, J. Li, *J. Mater. Sci.* **2017**, *53*, 2115.

[118] Y. Wang, E. Wang, X. Zhang, H. Yu, *Energy Fuels* **2021**, *35*, 1918.

[119] G. Qian, Y. Zhang, L. Li, R. Zhang, J. Xu, Z. Cheng, S. Xie, H. Wang, Q. Rao, Y. He, Y. Shen, L. Chen, M. Tang, Z.-F. Ma, *Energy Storage Mater.* **2020**, *27*, 140.

[120] J. Leng, J. Wang, W. Peng, Z. Tang, S. Xu, Y. Liu, J. Wang, *Small* **2021**, *17*, 2006869.

[121] X. Xu, H. Huo, J. Jian, L. Wang, H. Zhu, S. Xu, X. He, G. Yin, C. Du, X. Sun, *Adv. Energy Mater.* **2019**, *9*, 1803963.

[122] F. Zhang, S. Lou, S. Li, Z. Yu, Q. Liu, A. Dai, C. Cao, M. F. Toney, M. Ge, X. Xiao, W. K. Lee, Y. Yao, J. Deng, T. Liu, Y. Tang, G. Yin, J. Lu, D. Su, J. Wang, *Nat. Commun.* **2020**, *11*, 3050.

[123] Y. Bi, J. Tao, Y. Wu, L. Li, Y. Xu, E. Hu, B. Wu, J. Hu, C. Wang, J.-G. Zhang, *Science* **2020**, *370*, 1313.

[124] H.-H. Ryu, N.-Y. Park, T.-C. Noh, G.-C. Kang, F. Maglia, S.-J. Kim, C. S. Yoon, Y.-K. Sun, *ACS Energy Lett.* **2020**, *6*, 216.

[125] U. H. Kim, H. H. Ryu, J. H. Kim, R. Mücke, P. Kaghazchi, C. S. Yoon, Y. K. Sun, *Adv. Energy Mater.* **2019**, *9*, 1970046.

[126] Y. Su, G. Chen, L. Chen, Y. Lu, Q. Zhang, Z. Lv, C. Li, L. Li, N. Liu, G. Tan, L. Bao, S. Chen, F. Wu, *ACS Appl. Mater. Interfaces* **2019**, *11*, 36697.

[127] X. Ju, H. Huang, W. He, H. Zheng, P. Deng, S. Li, B. Qu, T. Wang, *ACS Sustainable Chem. Eng.* **2018**, *6*, 6312.

[128] M. Jiang, Q. Zhang, X. Wu, Z. Chen, D. L. Danilov, R.-A. Eichel, P. H. L. Notten, *ACS Appl. Energy Mater.* **2020**, *3*, 6583.

[129] Y. Su, Y. Yang, L. Chen, Y. Lu, L. Bao, G. Chen, Z. Yang, Q. Zhang, J. Wang, R. Chen, S. Chen, F. Wu, *Electrochim. Acta* **2018**, *292*, 217.

[130] S. Gao, X. Zhan, Y.-T. Cheng, *J. Power Sources* **2019**, *45*, 410.

[131] F. Wu, N. Liu, L. Chen, Y. Su, G. Tan, L. Bao, Q. Zhang, Y. Lu, J. Wang, S. Chen, J. Tan, *Nano Energy* **2019**, *59*, 50.

[132] C. H. Jung, D. H. Kim, D. Eum, K. H. Kim, J. Choi, J. Lee, H. H. Kim, K. Kang, S. H. Hong, *Adv. Funct. Mater.* **2021**, *31*, 2010095.

[133] U. H. Kim, J. H. Park, A. Aishova, R. M. Ribas, R. S. Monteiro, K. J. Griffith, C. S. Yoon, Y. K. Sun, *Adv. Energy Mater.* **2021**, *11*, 2100884.

[134] U.-H. Kim, G.-T. Park, P. Conlin, N. Ashburn, K. Cho, Y.-S. Yu, D. A. Shapiro, F. Maglia, S.-J. Kim, P. Lamp, C. S. Yoon, Y.-K. Sun, *Energy Environ. Sci.* **2021**, *14*, 1573.

[135] Y. Levartovsky, A. Chakraborty, S. Kunnikuruvan, S. Maiti, J. Grinblat, M. Talianker, D. T. Major, D. Aurbach, *ACS Appl. Mater. Interfaces* **2021**, *13*, 34145.

[136] L. Wu, X. Tang, X. Chen, Z. Rong, W. Dang, Y. Wang, X. Li, L. Huang, Y. Zhang, *J. Power Sources* **2020**, *445*, 227337.

[137] M. Jeong, H. Kim, W. Lee, S.-J. Ahn, E. Lee, W.-S. Yoon, *J. Power Sources* **2020**, *474*, 228592.

[138] Y. Lv, X. Cheng, W. Qiang, B. Huang, *J. Power Sources* **2020**, *450*, 227718.

[139] B. Chu, S. Liu, L. You, D. Liu, T. Huang, Y. Li, A. Yu, *ACS Sustainable Chem. Eng.* **2020**, *8*, 3082.

[140] S. He, A. Wei, W. Li, X. Bai, L. Zhang, X. Li, R. He, L. Yang, Z. Liu, *Electrochim. Acta* **2019**, *318*, 362.

[141] L. Wang, R. Wang, J. Wang, R. Xu, X. Wang, C. Zhan, *ACS Appl. Mater. Interfaces* **2021**, *13*, 8324.

[142] U.-H. Kim, G.-T. Park, B.-K. Son, G. W. Nam, J. Liu, L.-Y. Kuo, P. Kaghazchi, C. S. Yoon, Y.-K. Sun, *Nat. Energy* **2020**, *5*, 860.

[143] K. Li, D. Xue, *J. Phys. Chem. A* **2006**, *110*, 11332.

[144] S. H. Song, M. Cho, I. Park, J. G. Yoo, K. T. Ko, J. Hong, J. Kim, S. K. Jung, M. Avdeev, S. Ji, S. Lee, J. Bang, H. Kim, *Adv. Energy Mater.* **2020**, *10*, 2000521.

[145] S. Yang, Q. Fan, Z. Shi, L. Liu, J. Liu, X. Ke, J. Liu, C. Hong, Y. Yang, Z. Guo, *ACS Appl. Mater. Interfaces* **2019**, *11*, 36742.

[146] A. M. Wise, C. Ban, J. N. Weker, S. Misra, A. S. Cavanagh, Z. Wu, Z. Li, M. S. Whittingham, K. Xu, S. M. George, M. F. Toney, *Chem. Mater.* **2015**, *27*, 6146.

**ADVANCED
SCIENCE NEWS**

www.advancedsciencenews.com

**ADVANCED
ENERGY
MATERIALS**

www.advenergymat.de

[147] Y. Li, X. Liu, D. Ren, H. Hsu, G.-L. Xu, J. Hou, L. Wang, X. Feng, L. Lu, W. Xu, Y. Ren, R. Li, X. He, K. Amine, M. Ouyang, *Nano Energy* **2020**, *71*, 104643.

[148] D. Hu, Y. Su, L. Chen, N. Li, L. Bao, Y. Lu, Q. Zhang, J. Wang, S. Chen, F. Wu, *J. Energy Chem.* **2020**, *58*, https://doi.org/10.1016/j.jechem.2020.09.031.

[149] K. Liu, Q. Zhang, S. Dai, W. Li, X. Liu, F. Ding, J. Zhang, *ACS Appl. Mater. Interfaces* **2018**, *10*, 34153.

[150] H. H. Sun, J. Y. Hwang, C. S. Yoon, A. Heller, C. B. Mullins, *ACS Nano* **2018**, *12*, 12912.

[151] J. Zhang, J. Zhang, X. Ou, C. Wang, C. Peng, B. Zhang, *ACS Appl. Mater. Interfaces* **2019**, *11*, 15507.

[152] Y.-G. Zou, F. Meng, D. Xiao, H. Sheng, W.-P. Chen, X.-H. Meng, Y.-H. Du, L. Gu, J.-L. Shi, Y.-G. Guo, *Nano Energy* **2021**, *87*, 106172.

[153] N. H. Yeh, F. M. Wang, C. Khotimah, X. C. Wang, Y. W. Lin, S. C. Chang, C. C. Hsu, Y. J. Chang, L. Tiong, C. H. Liu, Y. R. Lu, Y. F. Liao, C. K. Chang, S. C. Haw, C. W. Pao, J. L. Chen, C. L. Chen, J. F. Lee, T. S. Chan, H. S. Sheu, J. M. Chen, A. Ramar, C. H. Su, *ACS Appl. Mater. Interfaces* **2021**, *13*, 7355.

[154] H. J. Song, S. H. Oh, Y. Lee, J. Kim, T. Yim, *J. Power Sources* **2021**, *483*, 229218.

[155] K. Du, A. Gao, L. Gao, S. Sun, X. Lu, C. Yu, S. Li, H. Zhao, Y. Bai, *Nano Energy* **2021**, *83*, 105775.

[156] S. Jeong, J. H. Park, S. Y. Park, J. Kim, K. T. Lee, Y. D. Park, J. Mun, *ACS Appl. Mater. Interfaces* **2021**, *13*, 22475.

[157] K. Wu, J. Wang, Q. Li, Y. Yang, X. Deng, R. Dang, M. Wu, Z. Wu, X. Xiao, X. Yu, *Nanoscale* **2020**, *12*, 11182.

[158] C. S. Yoon, K.-J. Park, U.-H. Kim, K. H. Kang, H.-H. Ryu, Y.-K. Sun, *Chem. Mater.* **2017**, *29*, 10436.

[159] J. Zhang, Z. Yang, R. Gao, L. Gu, Z. Hu, X. Liu, *ACS Appl. Mater. Interfaces* **2017**, *9*, 29794.

[160] D.-W. Jun, C. S. Yoon, U.-H. Kim, Y.-K. Sun, *Chem. Mater.* **2017**, *29*, 5048.

[161] Y.-C. Li, W. Xiang, Y. Xiao, Z.-G. Wu, C.-L. Xu, W. Xu, Y.-D. Xu, C. Wu, Z.-G. Yang, X.-D. Guo, *J. Power Sources* **2019**, *423*, 144.

[162] W. Yang, W. Xiang, Y. X. Chen, Z. G. Wu, W. B. Hua, L. Qiu, F. R. He, J. Zhang, B. H. Zhong, X. D. Guo, *ACS Appl. Mater. Interfaces* **2020**, *12*, 10240.

[163] K.-H. Chen, M. J. Namkoong, V. Goel, C. Yang, S. Kazemiabnavi, S. M. Mortuza, E. Kazyak, J. Mazumder, K. Thornton, J. Sakamoto, N. P. Dasgupta, *J. Power Sources* **2020**, *471*, 228475.

[164] J. Kim, S. M. Nithya Jeghan, G. Lee, *Microporous Mesoporous Mater.* **2020**, *305*, 110325.

[165] D. Y. Rhee, J. Kim, J. Moon, M.-S. Park, *J. Alloys Compd.* **2020**, *843*, 156042.

[166] S. Heng, X. Shan, W. Wang, Y. Wang, G. Zhu, Q. Qu, H. Zheng, *Carbon* **2020**, *159*, 390.

[167] M. R. Al Hassan, A. Sen, T. Zaman, M. S. Mostari, *Mater. Today Chem.* **2019**, *11*, 225.

[168] Y. Liu, X. Li, L. Fan, S. Li, H. Maleki Kheimeh Sari, J. Qin, *Front. Chem.* **2019**, *7*, 721.

[169] W. Jiang, H. Wang, H. Xu, N. Li, C. Chen, C. Li, J. Li, H. Lv, L. Kuang, X. Tian, *Chem. Eng. J.* **2018**, *335*, 954.

[170] X. B. Cheng, R. Zhang, C. Z. Zhao, F. Wei, J. G. Zhang, Q. Zhang, *Adv. Sci.* **2016**, *3*, 1500213.

[171] R. Xu, X.-Q. Zhang, X.-B. Cheng, H.-J. Peng, C.-Z. Zhao, C. Yan, J.-Q. Huang, *Adv. Funct. Mater.* **2018**, *28*, 1705838.

[172] R. Zhang, S. Wen, N. Wang, K. Qin, E. Liu, C. Shi, N. Zhao, *Adv. Energy Mater.* **2018**, *8*, 1800914.

[173] G. Zheng, S. W. Lee, Z. Liang, H. W. Lee, K. Yan, H. Yao, H. Wang, W. Li, S. Chu, Y. Cui, *Nat. Nanotechnol.* **2014**, *9*, 618.

[174] F. Guo, C. Wu, H. Chen, F. Zhong, X. Ai, H. Yang, J. Qian, *Energy Storage Mater.* **2020**, *24*, 635.

[175] K. Yan, H. W. Lee, T. Gao, G. Zheng, H. Yao, H. Wang, Z. Lu, Y. Zhou, Z. Liang, Z. Liu, S. Chu, Y. Cui, *Nano Lett.* **2014**, *14*, 6016.

[176] L. Wang, Q. Wang, W. Jia, S. Chen, P. Gao, J. Li, *J. Power Sources* **2017**, *342*, 175.

[177] Y. Liu, D. Lin, P. Y. Yuen, K. Liu, J. Xie, R. H. Dauskardt, Y. Cui, *Adv. Mater.* **2017**, *29*, 1605531.

[178] E. Cha, M. D. Patel, J. Park, J. Hwang, V. Prasad, K. Cho, W. Choi, *Nat. Nanotechnol.* **2018**, *13*, 337.

[179] P. Zhao, Y. Feng, T. Li, B. Li, L. Hu, K. Sun, C. Bao, S. Xiong, A. Matic, J. Song, *Energy Storage Mater.* **2020**, *33*, 158.

[180] M. L. Meyerson, P. E. Papa, A. Heller, C. B. Mullins, *ACS Nano* **2021**, *15*, 29.

[181] R. Zhang, N. W. Li, X. B. Cheng, Y. X. Yin, Q. Zhang, Y. G. Guo, *Adv. Sci.* **2017**, *4*, 1600445.

[182] F. Guo, C. Wu, S. Chen, X. Ai, F. Zhong, H. Yang, J. Qian, *ACS Mater. Lett.* **2020**, *2*, 358.

[183] X. Zhang, Q. Wu, X. Guan, F. Cao, C. Li, J. Xu, *J. Power Sources* **2020**, *452*, 227833.

[184] C. Z. Zhao, Q. Zhao, X. Liu, J. Zheng, S. Stalin, Q. Zhang, L. A. Archer, *Adv. Mater.* **2020**, *32*, 1905629.

[185] W. Zhao, J. Zheng, L. Zou, H. Jia, B. Liu, H. Wang, M. H. Engelhard, C. Wang, W. Xu, Y. Yang, J.-G. Zhang, *Adv. Energy Mater.* **2018**, *8*, 2211.

[186] J. Li, Y. Liao, W. Fan, Z. Li, G. Li, Q. Zhang, L. Xing, M. Xu, W. Li, *ACS Appl. Energy Mater.* **2020**, *3*, 3049.

[187] A. Kazzazi, D. Bresser, M. Kuenzel, M. Hekmatfar, J. Schnaidt, Z. Jusys, T. Diemant, R. J. Behm, M. Copley, K. Maranski, J. Cookson, I. de Meatza, P. Axmann, M. Wohlfahrt-Mehrens, S. Passerini, *J. Power Sources* **2021**, *482*, 228975.

[188] K. Kim, Y. Kim, S. Park, H. J. Yang, S. J. Park, K. Shin, J.-J. Woo, S. Kim, S. Y. Hong, N.-S. Choi, *J. Power Sources* **2018**, *396*, 276.

[189] Z. Li, X. Lin, H. Zhou, L. Xing, G. Lan, W. Zhang, J. Chen, M. Liu, Q. Huang, W. Li, *J. Power Sources* **2020**, *467*, 228343.

[190] C. Wang, Q. Hu, J. Hao, X. Xu, L. Ouyang, W. Fan, J. Ye, J. Liu, J. Li, A. Mei, M. Zhu, *ACS Appl. Energy Mater.* **2021**, *4*, 2292.

[191] J. Alvarado, M. A. Schroeder, T. P. Pollard, X. Wang, J. Z. Lee, M. Zhang, T. Wynn, M. Ding, O. Borodin, Y. S. Meng, K. Xu, *Energy Environ. Sci.* **2019**, *12*, 780.

[192] S. H. Jang, K. Jung, T. Yim, *Curr. Appl. Phys.* **2018**, *18*, 1345.

[193] G. Lan, L. Xing, D. Bedrov, J. Chen, R. Guo, Y. Che, Z. Li, H. Zhou, W. Li, *J. Alloys Compd.* **2020**, *821*, 153236.

[194] S. H. Lee, J. Y. Hwang, S. J. Park, G. T. Park, Y. K. Sun, *Adv. Funct. Mater.* **2019**, *29*, 1902496.

[195] Y. Li, Y. An, Y. Tian, H. Fei, S. Xiong, Y. Qian, J. Feng, *J. Electrochem. Soc.* **2019**, *166*, A2736.

[196] K. Qian, Y. Liu, X. Zhou, D. J. Gosztola, H. Nguyen, T. Li, *Energy Storage Mater.* **2021**, *41*, 222.

[197] T. Yang, S. Li, W. Wang, J. Lu, W. Fan, X. Zuo, J. Nan, *J. Power Sources* **2021**, *505*, 230055.

[198] H. Q. Pham, M. Mirolo, M. Tarik, M. El Kazzi, S. Trabesinger, *Energy Storage Mater.* **2020**, *33*, 216.

[199] S. Li, T. Yang, W. Wang, J. Lu, X. Zhao, W. Fan, X. Zuo, J. Nan, *Electrochim. Acta* **2020**, *352*, 104309.

[200] H. Q. Pham, M. T. Nguyen, M. Tarik, M. El Kazzi, S. Trabesinger, *ChemSusChem* **2021**, *14*, 2461.

[201] Y. Lee, T. K. Lee, S. Kim, J. Lee, Y. Ahn, K. Kim, H. Ma, G. Park, S.-M. Lee, S. K. Kwak, N.-S. Choi, *Nano Energy* **2020**, *67*, 104309.
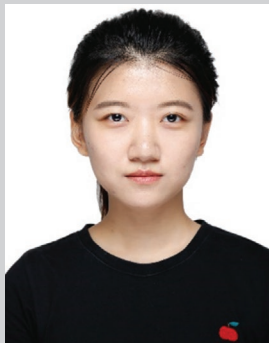
Ming Jiang is a Ph.D. candidate at the Eindhoven University of Technology (TU/e, The Netherlands) under the supervision of Prof. Peter H. L. Notten, and is a researcher at Forschungszentrum Jülich (Germany). Her topic focuses on the material design and degradation mechanism studies of Ni-rich cathode-based Li-ion batteries.

Dmitri L. Danilov, Ph.D., has a background in physics and mathematics and obtained his M.Sc. at the Saint-Petersburg University in 1993. In 2003, he got his Ph.D. degree from the University of Tilburg. In 2002, he joined the Eurandom Institute in Eindhoven University of Technology, being involved in various national and international research projects. His current research interests include mathematical modeling of complex electrochemical systems, including Li-ion and NiMH batteries, ageing and degradation processes, thin-film batteries, and advanced characterization methods. Starting 2017, he joined IEK-9 in the Forschungszentrum Jülich. He has published, as author and coauthor, more than 70 papers and book contributions.

Peter H. L. Notten worked in the Philips Research Laboratories (Eindhoven, The Netherlands) from 1975 to 2010. He received his Ph.D. degree from Eindhoven University in 1989. Since then, he has been focusing on energy storage research, including hydrogen and lithium storage materials, new battery technologies, modeling electrochemical systems, and design of battery-management algorithms. In 2000, he was appointed as a professor at TU/e, where he heads the group Energy Materials and Devices. In 2014, he was appointed as the International adjunct faculty at Amrita University, Coimbatore (India), and as a group leader at Forschungszentrum Jülich (Germany), and in 2018, as an honorary professor at the University of Technology Sydney.